CRANFIELD UNIVERSITY

Jafar S L Alzaili

SEMI-EMPIRICAL APPROACH TO CHARACTERIZE THIN WATER FILM BEHAVIOUR IN RELATION TO DROPLET SPLASHING IN MODELLING AIRCRAFT ICING

SCHOOL OF ENGINEERING
Department of Power and Propulsion
Turbomachinery and Icing Group

PhD Thesis
Academic Year: 2011 - 2012

Supervisor: Dr David W. Hammond
July 2012

CRANFIELD UNIVERSITY

SCHOOL OF ENGINEERING
Department of Power and Propulsion
Turbomachinery and Icing Group

PhD Thesis

Academic Year 2011 - 2012

JAFAR S. L. ALZAILI

SEMI-EMPIRICAL APPROACH TO CHARACTERIZE THIN WATER FILM BEHAVIOUR IN RELATION TO DROPLET SPLASHING IN MODELLING AIRCRAFT ICING

Supervisor: Dr. David W. Hammond
July 2012

This thesis is submitted in partial fulfilment of the requirements for the degree of Doctor of Philosophy

Abstract

Modelling the ice accretion in glaze regime for the supercooled large droplets is one of the most challenging problems in the aircraft icing field. The difficulties are related to the presence of the liquid water film on the surface in the glaze regime and also the phenomena associated with SLD conditions, specifically the splashing and re-impingement. The steady improvement of simulation methods and the increasing demand for highly optimised aircraft performance, make it worthwhile to try to get beyond the current level of modelling accuracy.

A semi-empirical method has been presented to characterize the thin water film in the icing problem based on both analytical and experimental approaches. The experiments have been performed at the Cranfield icing facilities. Imaging techniques have been used to observe and measure the features of the thin water film in the different conditions.

A series of numerical simulations based on an inviscid VOF model have been performed to characterize the splashing process for different water film to droplet size ratios and impact angles. Based on these numerical simulations and the proposed methods to estimate the thin water film thickness, a framework has been presented to model the effects of the splashing in the icing simulation. These effects are the lost mass from the water film due to the splashing and the re-impingement of the ejected droplets.

Finally, a new framework to study the solidification process of the thin water film has been explored. This framework is based on the lattice Boltzmann method and the preliminary results showed the capabilities of the method to model the dynamics, thermodynamics and the solidification of the thin water film.

Keywords:

Thin Water Film Velocity, Water Film Thickness, Corona Breakup, Volume of Fluid Method, Splashing and Re-impingement, Lattice Boltzmann Method, Solidification

Acknowledgments and Dedication

This research project would not have been possible without the support of many people. I would like to express my gratitude to my supervisor Dr. David Hammond, who was abundantly helpful and offered invaluable assistance, support and guidance during my PhD course. I would also like to thank the members of my thesis committee, Mr Roger Gent and Professor Chris Thompson for their time and comments.

I would also like to take this opportunity to thank the committee members of my first and second year review Dr Joao Amaral Teixeria and Dr James Whidborne.

I would like to express special thanks Dr. Richard Purvis from University of East Anglia for his involvement in the numerical simulations for providing the VOF numerical tool and his involvement in this work.

The advice and comments from all the members of the EXTICE project or their comments during the meetings and the teleconferences have been invaluable, and for which I am deeply grateful. My special thanks to Dr. Giuseppe Mingione and Dr. Emiliano Iuliano from CIRA and Dr Pierre Berthoumieu from ONERA.

I also would like to thank Prof. Frank Smith from University College of London and Prof Mark Savill from Cranfield University for their advices during the icing group meetings, and Mr Brian Stapleton, Dr. Omid Gohardani and Dr. Adair Williams for their help in performing the experiments. I want to acknowledge and thank Dr. Shidvash Vakilipour from University of Manitoba for his advice in the lattice Boltzmann modelling.

During my daily work at Cranfield I have been blessed with a cheerful and friendly group of fellow student, Thank you to all my colleagues whom have made my time during the research course joyful and full of fun.

Finally I would like to thank the department of Power and Propulsion for providing the support and equipment I have needed to produce and complete my thesis.

I would like to dedicate this dissertation to my beloved wife Asma for her unrelenting support and understanding during my research and to my parents for their endless love, support and encouragement and to those who contributed by imparting their knowledge and wisdom.

May Almighty God bless them all.

Table of Contents

List of Figures

List of Tables

List of Equations

List of Abbreviations

SLD	Supercooled Large Droplet
LED	Light Emitting Diode
CCD	Charged Coupled Detector
LWC	Liquid Water Content (g/m^3)
VOF	Volume Of Fluid
LBM	Lattice Boltzmann Method
PDF	Particle Distribution Function
MVD	Median Volumetric Diameter (μm)
MED	Mean Effective Diameter (μm)
Q_c	convective heat (J)
Q_e	evaporation heat (J)
Q_d	sensible heat (J)
Q_k	kinetic energy (J)
Q_l	latent heat (J)
Q_a	aerodynamic heating (J)
θ, θ_c	contact angle (degree)
θ_a, θ_r	advancing and receding contact angles (degree)
p, q	distance of object and image from the lens (m)
f_L, m	focal length of the lens (m) and the magnification of lens
d	droplet size (μm)
V_f	water film velocity (cm/s)
τ_w	air shear stress on the surface (Pa)
δ	air boundary layer thickness (μm)
V	airflow velocity (m/s)
$V_{in}, \dot{n}$	velocity (m/s) and rate of the droplets generation (1/s) in the inlet of icing tunnel
ξ	distance from stagnation point (mm)
y^+	non dimensional turbulent wall distance
Re_f	Reynolds number based on water film characteristics
Re_d	Reynolds number based on droplet characteristics
We	Weber number based on droplet characteristics
ρ_w, μ_w	water density (kg/m^3) and water molecular viscosity (Pa.s)
α	impact angle (degree)
ω	relative Liquid Water Content = LWC/ρ_w

h	water film thickness (μm)
σ	surface tension (N/m)
u, v, w	x-component, y-component and z-component of velocity (m/s)
s, n	tangential and normal direction
β, β_0	catch efficiency
Q	water volumetric flow flux per depth unit (m^2/s)
J_w	incoming water mass flux per unit area ($kg/s.m^2$)
a_s	tangential acceleration per unit volume (N/m^3)
ϵ	small parameter
g_0	gravitational acceleration (m/s^2)
t	time (s)
t^*	dimensionless time = t/(d/V)
t_{cd}	breakup time of the corona
M	Mach number
f_{imp}	frequency of the droplets impact
p	pressure
δ^*	dimensionless air boundary layer thickness
$\hat{h}$	dimensionless water film thickness =h/d
Υ	curvature of the water film
m_{sp}	splashed mass from droplet
$m_{sp,total}$	total splashed mass from the droplet and the water film
m_d	droplet mass
$\alpha_{j,L}$	left jet angle (degree)
$\alpha_{j,R}$	right jet angle (degree)
$V_{j,L}$	left jet velocity (m/s)
$V_{j,R}$	right jet velocity (m/s)
$(V_{j,L})_n$	normal component of left jet velocity (m/s)
$(V_{jR})_n$	normal component of right jet velocity (m/s)
n_s	number of the secondary droplets after the splash
d_{sec}	size of the secondary droplets (μm)
c_d	drag coefficient of the droplets
$\dot{x}, \dot{y}$	particle velocity in x and y directions
$\ddot{x}, \ddot{y}$	particle acceleration in x and y directions
f, g	particle distribution functions

$\vec{c}, \vec{e}$	particle velocity and direction vectors
$\vec{F}$	external force vector
$\vec{S}$	source term in the momentum equation
$\vec{x} = (x, y, z)$	position vector
$\vec{u}, T$	macroscopic velocity vector and macroscopic temperature
τ_f, τ_T	relaxation time for momentum and energy
c_s	speed of sound
ν	kinematic viscosity
I, J, k, k^-	Indices
w	weight function
δ_x, δ_t	spatial and temporal spacing
N, N_{iter}	number of the computational cells and number of iterations
$L_0 (and\ H), t_0$	physical length and time scales
$U, \widetilde{U}$	velocity scales in the physical and lattice units
f^{eq}, g^{eq}	equilibrium particle distribution functions for momentum and energy
α_T, β_T	thermal diffusivity and thermal expansion
Ec	Eckert number
Ψ	collision term
Pr	Prandtl Number
Ra	Rayleigh number
Nu	Nusselt number
β_T	thermal expansion (1/ºK)
K_0	constant in the permeability term in the momentum equation (kg/s.m^3)
φ	phase fraction function
T_f	freezing temperature
L	latent heat of freezing (kJ/kg)
c_p	heat capacity (J/kgºK)
ΔT	temperature variation in the system (ºK)
T_H, T_c, T_m	temperature boundary value and the average temperature in the domain
T_w, q_w	temperature and heat flux on the wall
St	Stefan number
$\vec{u}_{in}, \vec{u}_{out}$	known velocity vector on the inlet and outlet boundaries
ρ_{in}, ρ_{out}	known density on the inlet and outlet boundaries
u_{lid}	known velocity on the moving boundary

1 Introduction and Motivation of this Research

1.1 EXTICE Project and Motivation of this Work

The biggest weakness of existing icing codes is in the prediction of ice accreted over the surfaces in glaze SLD icing conditions. There are many works undertaken to improve the understanding of glaze and SLD icing physics. One of these works is EXTICE project (EXTreme ICing Environment) which is funded by European Community as a part of Seventh Framework Programme (FP7). The aim of EXTICE project is to improve the ice prediction tools in the SLD icing conditions. The consortium has undertaken a series of fundamental experiments to understand the physics beyond the SLD icing. The focus of the studies was on the first order effect of the SLD conditions which is believed to be the splashing of the large droplets. As the outcome of these experiments, the consortium is expected to generate some correlations and models to be implemented in the current icing codes in order to improve the accuracy of ice prediction in the SLD conditions. The proposed models are compared with full scale icing tunnel test and in-flight icing tests. Figure 1-1 shows the interaction of the different measures taken in EXTICE project to improve icing simulation in the SLD conditions. Figure 1-2 shows the details of the different work packages and the tasks of the project.

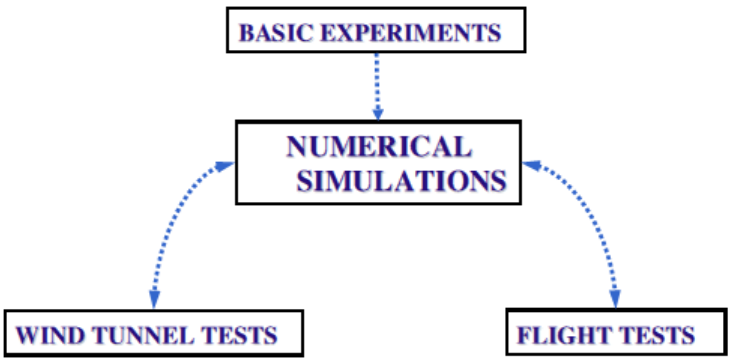

Figure 1-1 Interaction of the different measures taken in EXTICE project to improve icing simulation

Cranfield University is one of the partners in the EXTICE project and this PhD research is funded by EXTICE project. The main participation of Cranfield University was to perform a series of basic experiments to characterize the liquid water film in the SLD icing conditions. We believed that liquid water film has significant impact on the splashing process of the SLD and subsequently affects the ice accretion. We emphasise that for better prediction of ice shapes especially in the SLD condition and glaze regime, it is essential to understand the liquid water film dynamics and its solidification which is responsible for forming the roughness and final ice shapes. This PhD work has been undertaken as a part of activities of the EXTICE projects and consists of three major parts:

- Experimental study of liquid water film in Cranfield icing tunnel facilities
- Developing a semi-empirical model of SLD splashing
- Introducing and exploring a new numerical tool to model the dynamics of thin liquid water film and its solidification

The first and second parts have been undertaken as our participation in EXTICE project in the activities of work package 2 (WP2 in Figure 1-2). The outcome of these two parts of the research is a methodology to estimate the thin water film thickness in icing problem and a deterministic method to predict the features of splashing of SLD. The novelty of this methodology is to consider the effects of water film characteristics on the splashing process. This assumption was based on both experimental data and simulation of the splashing using sophisticated numerical modelling tools (Quero, 2006 and Purvis, 2004). The different features of the water film such as its thickness, velocity, waviness and wave celerity have been measured in different conditions and a set of correlations have been developed to characterize the water film in the SLD condition. The experiments have been undertaken in Cranfield icing tunnel facilities and the vertical icing tunnel, which is capable for study of SLD condition, has been used to investigate the dynamics of water film formed by SLD impact on a small aluminium target in the different conditions.

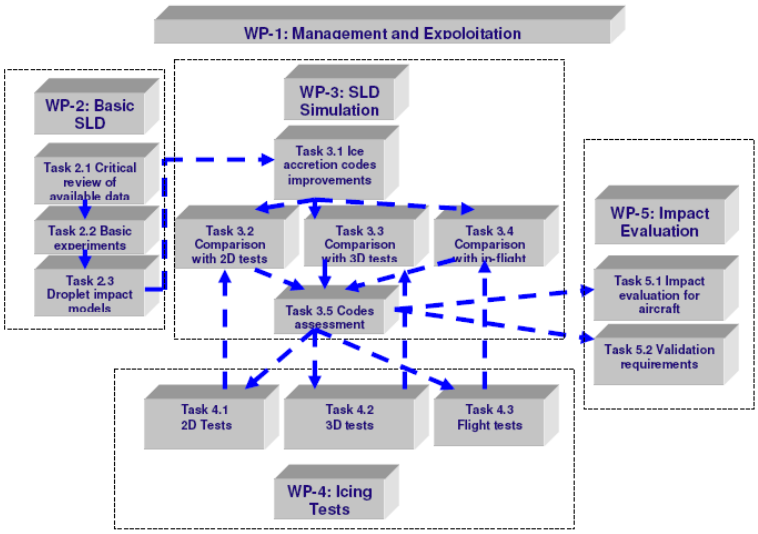

Figure 1-2 Details of different work packages and tasks of EXTICE project

Numerical modelling based on the lattice Boltzmann method has been introduced and developed to help with analysing the water film characteristics. This method has potential capabilities to model both water film hydrodynamics and the solidification problems. The lattice Boltzmann method could be used to model flow over complex geometries such ice roughness and it shows better efficiency than traditional CFD methods in modelling this kind of problem. The other advantage of using the lattice Boltzmann method instead of CFD methods is the parallelization potential capability of this method.

1.2 In-flight Icing and SLD Conditions

In-flight icing can happen when aircraft fly through clouds and in this condition the ambient temperature could be below the freezing point of water. Additionally supercooled water droplets, which are liquid but their temperature is below the freezing point, can exist in the clouds. These supercooled droplets freeze after impact with the body of aircraft causing the formation of ice over the exposed surfaces of the aircraft. The ice formed over the leading edge of the wings, control surfaces, and engine inlet can have significant impact on aircraft

performance and stability. To avoid aerodynamic degradation and instability problems during the flight, both anti-icing and de-icing systems are widely used in the current aircraft. According to aircraft safety regulations, designers should prove the ability of aircraft to fly in icing conditions without any serious problem in safety and stability. During the design procedure, icing tunnel tests and in-flight test are usually used to analyse the aircraft performance and stability in icing conditions. The advantage of these methods is their realism but in the same time they are very expensive. By developing both computational methods and computer hardware, icing simulation has started to be used regularly as a powerful tool to analysis the aircraft icing.

1.2.1 Metrological Background

As it has been said two main conditions are required for aircraft icing to occur:

- Existence of supercooled water droplets
- The temperature on the surface below the freezing point of pure water

Water droplets can be found in clouds and in general cloud can consist of water droplets, ice crystals or both phases (mixed clouds). Our focus in this work is on the aircraft icing associated with liquid supercooled water and we do not discuss the icing occur because of ice crystal. However this kind of icing recently has been in interest of icing community and considerable number of incidents and accidents are thought to be related to ice crystals icing. The ice crystals do not easily stick on aircraft surfaces but they can seriously affect the engine and measurement devices on the aircraft.

Figure 1-3 Examples of different clouds causing in-flight icing: Cumulus congestus (left), Cumulonimbus calvus precipitation (middle), Cumulonimbus capillatus incus (right)

The clouds with water droplets are usually characterized by their sharp-cut edges. The Cumulus congestus clouds usually have liquid water on them and pilots are advised to avoid flying through this kind of clouds. The Cumulonimbus capillatus incus clouds usually carry huge amount of ice crystals and a Cumulonimbus calvus precipitation cloud are containing both ice crystals and water droplets. If air temperature is lower than (-40 °C), clouds are essentially ice crystal clouds and as the ambient temperature increases, the clouds are more likely to contain water droplets. When temperature reach (-40 °C) the droplets are tending to freeze spontaneously while in warmer temperature an initial disturbance or small ice particle (ice nucleus) are needed for freezing or water droplets. When these supercooled liquid water droplets hit the surface of the aircraft, it initiates the freezing process of liquid droplets and forms the ice over the aircraft surfaces.

The basis of formation of the supercooled droplets could be explained by up-draft air phenomena. Air rises from warmer to colder zone and it tends to become saturated when there is enough humidity in air. The vapour in the colder area transforms into water droplets through condensation process in the colder altitudes. When liquid water droplets are formed, they are no longer arising with the air the gravity forces them to fall. If the surrounding temperature is warm and above the freezing point, they will fall immediately to form the warm rain, while in the lower temperature the droplets will freeze and fall as ice crystals or graupel. They could melt in a lower altitude and fall as a cold rain. These mechanisms can explain why in the zones where the temperature is around the freezing point, is more likely to encounter supercooled water droplets. The droplets condensation phenomena, which characterize the warm rain process, could also lead to the formation of the supercooled large droplets (SLD) with sizes larger than usual. Supercooled large droplets are associated with a hazardous type of aircraft icing and this will be discussed in more details later in this chapter. The temperature inversion could cause the formation of the supercooled large droplets through the cold rain process. When ice crystals melt in the lower altitudes they can form large water droplets. These droplets when fall through a temperature inversion zone will become supercooled. This

mechanism is the main reason of the formation of SLD and it explains why SLD is more likely to occur in the relatively lower altitudes mainly below 12,000 ft (Mingione, 2002).

1.2.2 Ice Accretion

The major environmental factors affecting aircraft icing are liquid water content, ambient temperature and water droplet size in the clouds. Cloud liquid water content (LWC) is the density of liquid water in a cloud and has direct effect on the amount of the accreted ice on the exposed surfaces of aircraft. It is usually expressed in term of grams of liquid water per cubic meter of air (g/m^3) and typical values of LWC in the clouds vary from 0.3 g/m^3 to 0.6 g/m^3 although it is usual to find cumuliform clouds with LWC value of 1.7 g/m^3 and higher. Ambient temperature affects both the severity and the type of ice formed on the aircraft when it is exposed to liquid water while flying in the clouds. As it was discussed, most of icing events, which are associated with supercooled liquid droplets in the atmosphere, tend to occur at temperatures between 0 °C to -20 °C and in the lower temperature is more likely to find ice crystals rather than supercooled water droplets. In the limit of (-40 °C) only ice crystals are found in the clouds because at this temperature droplets freeze even without icing nuclei.

The ice formed in the different temperatures, has different appearance and transparency. When temperature is lower than (-15 °C), the water droplets tend to freeze rapidly when they hit the cold aircraft surfaces. This category of ice has fragile and dense structure and milky colour. Although rime ice usually is characterized by the ambient temperature, its formation depends on the LWC as well. If liquid water is high enough, all the droplets could not freeze rapidly upon impact on the surfaces, and a liquid water film will form on the surface (or on the accumulated ice). Also in the case of large droplets, a liquid water film will form on the surface and not all of liquid water freeze immediately even in the low temperatures. When a liquid water film form on the surface, the ice accreted has a transparent structure and it is called glaze ice. This type of ice is characterized by the higher temperature, higher liquid water content and also

larger droplet size which all of these conditions will lead to formation of a liquid water film instead of rapid freezing of the incoming droplets. The glaze ice has irregular shape which can be related to the liquid water film random movement over the surface.

Figure 1-4 Glaze and Rime Ice, Cranfield icing wind tunnel, left: glaze ice, right: rime ice

The other important environmental parameter of icing is the droplet diameter (or an alternative size scale if the droplets are not sphere) which is usually expressed in micron (μm). In the reality there is a spectrum of droplet size in the clouds, therefore the actual droplet size distribution is represented by an average value called median volumetric diameter (MVD) which is expressed in micron as well. In the most of cases, the MVD of the clouds is smaller than 50 microns and the classical icing is associated with this type of water droplets. However, as is discussed, in some cases the clouds contain larger droplets with MVD higher than 50 microns and SLD icing is associated with this type of water droplets. In the case of classical icing, the droplets tend to impact the wing of the aircraft near the leading edge which is protected with an appropriate anti icing or de icing system. However, in the case of SLD, the large droplets will not follow the air path to impact the wing on the leading edge and may impact further back on the area which is not protected against the icing. Also in the case of SLD, the droplets have higher inertial energy and when they hit the

surface, some secondary droplets could be ejected to the airflow around the surface. These smaller secondary droplets could re-impinge somewhere on the unprotected area of the aircraft and causing ice accretion.

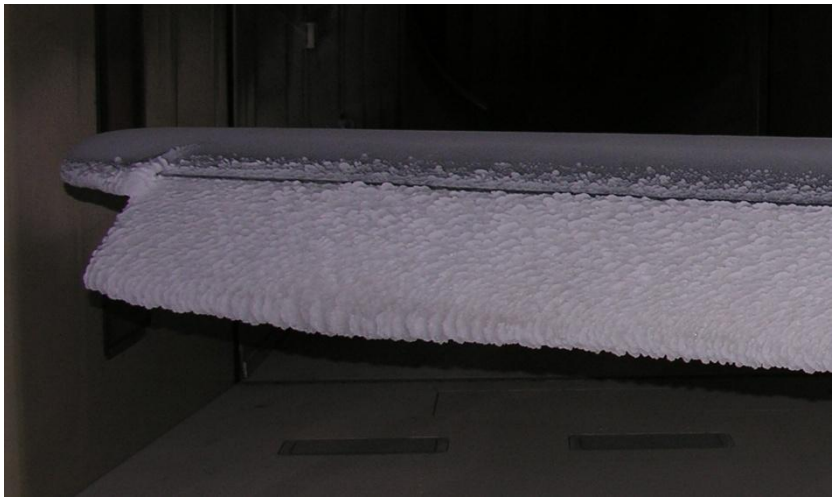

Figure 1-5 Example of SLD ice accretion on a 3D wing (CIRA ice accretion test campaign, EXTICE project)

There are other forms of icing such step ice, runback ice, SLD ice ridge and frost. Step ice is a ridge of ice along the wing span which may accumulate on wing with low power thermal ice protection systems. If there is enough power to avoid water freezing on the leading edge, but not enough for water evaporation, water can run back on the aircraft surface and freeze later on beyond the protected area and form so-called runback ice. Since SLD are droplets with a relatively large size, they can accumulate on a wide wing area, even beyond the ice protected zone. In particular, in case of pneumatic boot ice protection system, the boot activation can create a ridge of residual ice beyond the protected area and this ridge can act as a trigger for additional ice accumulation Frost may form on the aircraft in flight when descent is made from below freezing conditions into a layer of warm moist air. In this condition aerodynamic performances may be affected and vision may be restricted as frost forms on windshield and canopy (Mingione, 2002).

Figure 1-4 shows an example of glaze ice for classical water droplet size. The MVD in this case is 20 μm, air velocity is 50 m/s and the temperature is (-5 °C) for the glaze ice and (-15 °C) for the rime ice. Figure 1-5 shows an example of glaze SLD ice accretion on Dassault business jet wing section where the temperature is (-10 °C), LWC is 0.33 g/m^3, MVD is 143 μm and the air velocity is 60 m/s.

1.2.3 Effects of the Icing

The ice accreted over the vulnerable surfaces such as the leading edge of the wings, control surfaces, and engines inlet has significant impact on aircraft performance and stability which could affect the flight safety. Both anti-icing and de-icing systems are used in the aircraft in order to prevent aerodynamic degradation and instability problem during the flight.

The accreted ice could affect the aircraft performance in different ways depending on the design of the aircraft and also the characteristics of the accreted ice itself. The ice accreted on aircraft generally could decrease lift, increase drag, reduce stall angle, decrease thrust of the engines and could affect longitudinal and lateral stability of the aircraft. Even small ice roughness on the leading edge of the wing could change the stall characteristics of the aircraft and also could cause loss in of effectiveness of control surfaces because of the flow separation. Most of flight accidents caused by icing are related to stall in wing and tail, roll upset, ground icing, engine icing, instrument icing and icing on windshield.

The aviation authorities, as part of airworthiness standards, have different icing certification for the aircrafts depending on the size and flight conditions which the vehicle is designed for. Federal Aviation Authority in the United States of America published the first icing certification requirement for the commercial jet on the early 1960's. These requirements have been concluded in what is known by aviation community as "Appendix C" (FAA, 2002). The icing conditions envelopes in this document are specified based on real metrological monitoring and measurements which are believed to have most significant effects on flight

safety. The aircraft are required to be shown fly safely in theses icing conditions which are related to supercooled liquid droplets up to 50 μm and liquid water content up to 3.0 g/m^3. The details of these conditions are given in the end of this thesis in App. A. It should be noticed that in real conditions there is no single droplet size in the clouds and the aforementioned droplet sizes are the representative of a spectrum of droplet size. The droplet size in any cloud is characterized using a parameter called Median Volumetric Diameter: (MVD), the droplet diameter which divides the total water volume present in the droplet distribution in half. The values are obtained by actual drop size measurement (Mingione, 2002). Sometimes Mean Effective Droplet Diameter (MED) is used to characterize the droplet size which has quite similar definition of MVD.

On October 31, 1994 an American Eagle ATR-72 turboprop aircraft carrying 68 people experienced an out of commanded roll and crashed in a field at Roselawn, Indiana while it was in a holding pattern to land in Chicago O'Hare Airport. The National Transport Safety Board (NTSB) concluded that ice had accreted aft of the aircraft's wing de-icing boots on the upper surface of the wing causing aileron deflections which were not commanded by the auto pilot system. It was also concluded that this icing condition that led to the formation of the ice on the unprotected area of the wing was caused by freezing drizzle (SLD icing condition). Figure 1-6 shows the protected area of ATR-72 against icing which couldn't help it to survive the SLD icing condition in the accident of Roselawn.

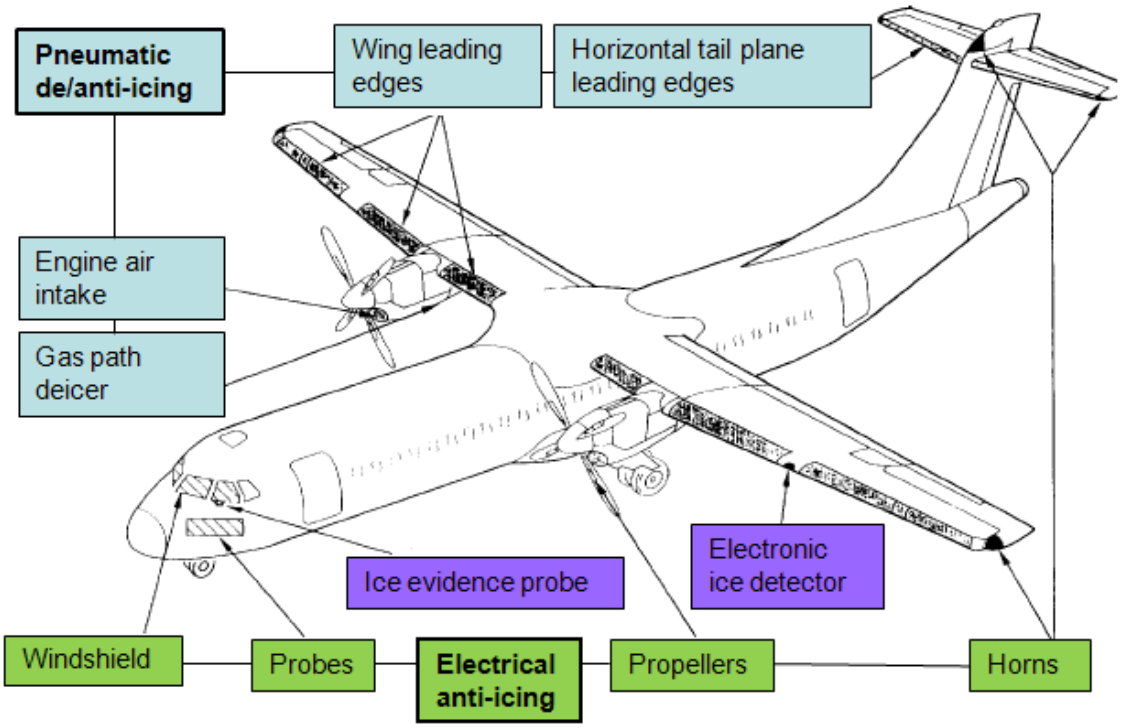

Figure 1-6 the ice protection systems on ATR-72 aircraft which was involved in an accident caused by SLD icing (NTSB report)

This type of icing was not considered in any airworthiness standards and it was believed that it does not have any significant effect on the flight safety. Based on this accident and some other incidents, which were related to SLD icing conditions, FAA has introduced new regulations for aircraft safety when it flies in SLD icing conditions. These regulations alongside with flight safety requirements for flight in ice crystal conditions have been concluded in "Appendix O" of the airworthiness standards (FAA, 2010). The envelopes of icing conditions in the proposed new regulations are specified for the freezing drizzle (droplet size from 50 μm to 500 μm) and freezing rain (supercooled droplet with diameter up to 2mm). The main difference of the SLD icing and common icing conditions could be concluded as follows:

- Due to bigger size of the droplets, they could hit the surfaces in areas which are not protected against icing. The impingement zone for the larger droplets is bigger and it may include some unprotected areas.

- Due to bigger size of the droplets and the momentum they carrying out, some of the droplet will be ejected to the airflow after the impact to the surface. The secondary ejected droplets may hit other surfaces of the aircraft which are not protected against icing.

Several aspects of SLD icing will be discussed later in this chapter.

1.3 Aircraft Icing Simulation

The aim of the icing codes is to simulate the ice accretion over different parts of the aircraft caused by supercooled water droplet impingement during the flight. The main concept used in the icing codes is the energy balance over the target substrate. The usual way is to consider the water accreted over the substrate as a system and to calculate the local energy balance. This water film is formed by impingement of incoming droplets over the substrate. The amount of this water which freezes and forms the ice over the substrate, depends on the conditions such as droplet temperature and velocity, substrate shape, thermal properties of the substrate, rate of impingement and airflow conditions around the target.

1.3.1 The Basis of Icing Codes

One can consider the icing simulation as an iterative procedure marching in time to estimate the ice shape over the target in different time steps. For any time step, the following processes must be undertaken and the results of this time step will then become the initial conditions for the next time step;

- First step is to calculate the flow field considering the ice free condition; this calculation forms the initial condition for next calculations.
- The second step is to calculate the droplet trajectories in order to estimate the incoming water rate to the surface and the impingement limits. They depend on droplet velocity and water liquid content (LWC). In addition, collection efficiency, which determines the ability of the target to collect the coming droplets, must be calculated.
- The main step is to perform ice growth calculations. This step is based on the heat balance (balancing the heat loss and heat gain for the

system of ice and water over a small element), mass balance (total mass is constant for this system) and the considerations of phase change for both mass and heat balance. This step is performed for every element over the impact surface. By choosing an appropriate set of equations, we can calculate the ice and water film conditions over the target.

- Finally the geometry should be modified by the addition of ice growth. Now the flow field may be recalculated using this new geometry and repeat the above calculation stages.

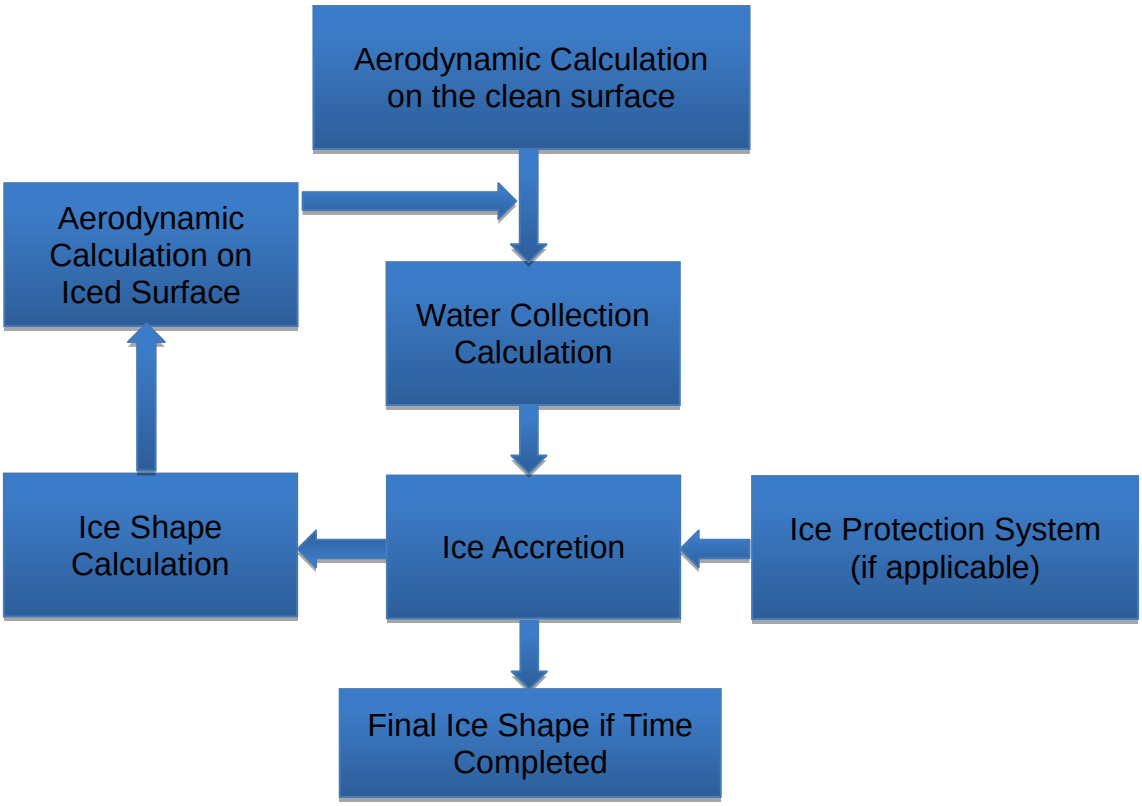

Figure 1-7 Ice simulation procedure in icing codes

Figure 1-7 shows the procedure used in icing codes to simulate aircraft icing. If a thermal ice protection system simulation is applicable, it is generally modelled as an energy source in ice accretion modelling stage.

This process will be repeated for a number of time steps. The existing icing codes (such as LEWICE, TRAJICE, CAPTA (developed by ONERA), ICECREMO, MULTI-ICE, and CANICE) use the methodology based on Messinger (Messinger, 1953) model to do these calculations. There are many modifications made on this basic model, which will be discussed later.

The four main stages of this procedure are discussed in the following sections. LEWICE icing code is used as the default reference to discuss the icing codes. The data and manuals related to this icing code are accessible while other icing codes have less provided information.

Airflow Calculations

The first step is to calculate the flow field considering the ice free condition; this calculation forms the initial condition for next calculations. Even for basic form of the Messinger model, it is necessary to know the airflow conditions in order to be able to determine the droplets trajectory and subsequently the way and amount of droplet impingement over the target. In the other hand, we need to determine the boundary layer of air over the surface for heat transfer calculation. The icing codes use different approaches for these calculations depending on the level of accuracy and computation cost acceptable for a specific application. For example, LEWICE (Wright, 2001) uses a panel method with boundary layer modifications to predict the airflow around the body. ICECREMO (Hammond, 2000) has the ability to use any three-dimensional CFD results as input for the icing calculations. Both these approaches have advantages and disadvantages. When we use a panel method, it is possible to modify the geometry after each time step (Ruff, 1990). It would cost much more to modify the geometry each time step when more accurate CFD methods are used. In this case, it is necessary to re-mesh the geometry after each time step. Some icing codes perform the aerodynamic calculations only in the beginning of the simulation procedure. However, this is a balancing problem, between the accuracy needed and computational cost.

Droplet Trajectory

The second part of an icing code is the droplet trajectory calculation. In this step of the calculation, the droplet impingement characteristics such as droplet velocity, impact angle, final droplet size and rate of impingement must be determined in this part. There are two main approaches for determining droplet trajectory, the Eulerian approach and the Lagrangian approach. A Lagrangian approach is used to track the droplets trajectories and to determine which of them impinge the body and which fly over the body and escape from the domain. In this approach, it is possible to define different conditions for the incoming droplets such as size and initial conditions. The equations of motion are integrated for the droplets using the local airflow conditions, which have been calculated in the previous step of ice simulation. The details of this approach are given in LEWICE user manual (Wright, 2001). In the Eulerian approach, the droplets are treated as continues flow and different set of mass and momentum conservation equations are solved to estimate their characteristics (Bourgault, 1999). There is a limitation in this method when considering different sizes of droplets, leading to many more calculations when compared to the Lagrangian approach. In the icing codes, it is more conventional to use the Lagrangian approach to determine droplet trajectories.

Icing Calculations

Messinger (1953) developed what is now accepted as the basic method of ice accretion modelling. This model is based on equating the energies sources for heating and cooling for the system and the mass balance in the system. He considered the following components cause cooling of the system of the water film and the ice layer over the surface:

- Convective heat transfer on the interface of water film and air (Q_c)
- Heat loss due to evaporation of water (Q_e)
- Cooling causes by temperature difference between incoming droplets and water film (Q_d).

The components causing warming were considered as:

- Kinetic energy of the incoming droplets (Q_k)
- Latent heat released during the freezing of water (Q_l)
- Heat gained by aerodynamic heating (Q_a).

To estimate the equilibrium temperature and freezing fraction, Messinger used energy balance and assumed that:

$$Q_c + Q_e + Q_d = Q_k + Q_l + Q_a \quad \textbf{(1-1)}$$

The schematic of this system is showed in Figure 1-8. This model is discussed in more details in (Myers, 2001 and Fortin, 2006).

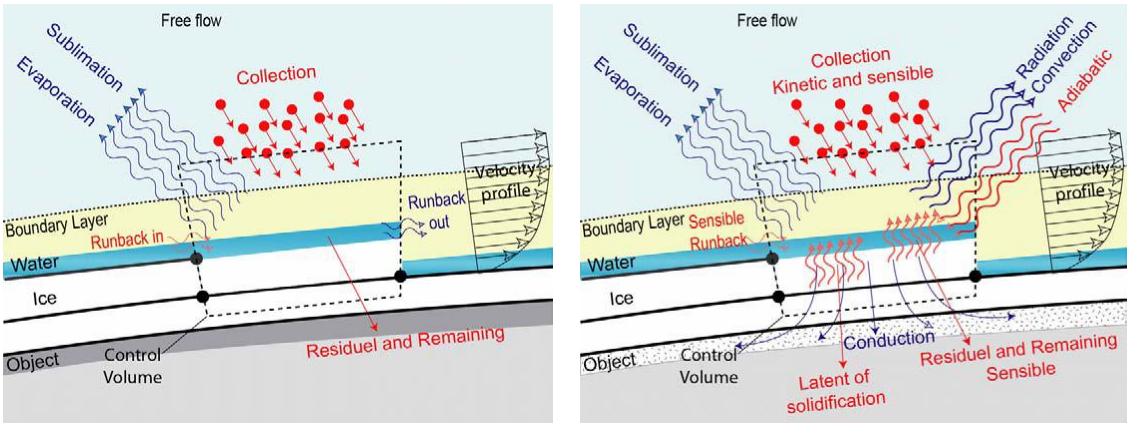

Figure 1-8 Mass balance (left) and energy balance (right) for liquid water in Messinger model (Fortin, 2006)

There are some modifications to this model based on both experimental data and observations and also analytical approach. Myers (2001) and Davis (2001) and other researchers have introduced more sophisticated modelling for ice growth by considering the variation of temperatures of ice and water film with time and by extending zero-dimensional Messinger model in its basic form to the multi-dimensional models.

Geometry Modification

The last stage of any time step is to modify the geometry by adding the calculated ice growth. This stage is computationally expensive because it is necessary first to re-mesh the field around the geometry which takes time and also needs very smart meshing process to generate a good mesh over an iced surface. The iced surface, unlike the clean one, does not have a smooth geometry and this makes the mesh generation more difficult. If an icing code uses structured data to save the mesh information, because of rough shape of iced surface there is further difficulty to map the data back on to the structured mesh. ICECREMO is one of the icing codes, which uses unstructured data to deal with this problem. There are some icing codes like LEWICE and the CAPTA icing codes that use panel method to prevent this difficulty. With panel methods, as described, it is not necessary to mesh the field around the geometry and the air flow calculation needs only the geometry of surface. The disadvantage of this method is the poor accuracy in comparison with solving Navier-Stokes equations. However several modifications have been made to improve the accuracy of panel methods to predict the air flow field (Wright, 2002).

After this stage the flow field should be recalculated using this new geometry and repeat above calculation stages.

1.3.2 Assessment of Icing Codes

There are some surveys which have been done to assess the accuracy of the icing codes. In 1997, an AGARD report titled “Ice Accretion Simulation” addressed the overall accuracy of the icing codes at that time. One of the recommendations in this report was that more study of ice growth physics was desirable to achieve more accuracy in icing modelling. This included the basic physics of ice accretion and especially crystal growth behaviour and the evolution of roughness elements. They believed that this research is essential for the accurate prediction of ice shape in glaze regime and three-dimensional ice growth problems.

In December 2000, RTO of NATO organized a workshop to evaluate the icing codes (NATO, 2001). The following icing codes were discussed in this workshop: CAPTA, LEWICE, TRAJICE, MULTI-ICE, CANICE and ICECREMO. The test cases were mainly from the glaze ice regime, which is the most difficult to predict. The results of this workshop showed the shortcomings of all icing codes to produce accurate ice shapes in the glaze ice regime. The authors recommended that improved modelling of the physical phenomena underlying the icing process should be uses and experimental studies of icing must be used to support these efforts.

Gent (2000) believed that to have more accurate ice prediction codes, more research is needed to study the freezing process of the individual droplets, the formation and characteristics of the water film and the development of roughness. The authors assumed that this should lead to better predictions of the localized three-dimensional features of ice. In addition, phenomena related to SLD conditions need to be modelled more accurately.

1.4 Wetting Physics

One of the most important factors in the study of glaze icing conditions is the liquid water behaviour over the surfaces. In fact, this factor distinguishes the glaze icing condition from rime icing condition. In rime ice there is very little liquid water over the surface and the low temperature in this type of icing insures that all impinging water is freezing very quickly after the impact. In this research, our focus is on the behaviour of liquid water over the surfaces in the icing process. It is mandatory before undertaking experiments in this field, to have a brief study of behaviour of liquid water over surfaces. It will help the understanding of the way water behaves over solid surfaces and also will help in the design of useful experiments for this research.

Wetting is a general concept in physics and chemistry which means the ability of a liquid to maintain contact with a solid surface. It results from intermolecular interactions when a liquid and solid surface, are in contact (Schrader, 1992). As we are studying the icing process made by liquid water, only water as liquid will

be studied here. The degree of wetting or wettability is determined by a force balance between adhesive and cohesive forces. The adhesive force here is between the liquid water and the solid surface and cohesive force is referred to liquid water. Cohesion is a physical property of substance, caused by the intermolecular attraction between like-molecules within the substance acting to unite them. Liquid water is strongly cohesive as each molecule may make four hydrogen bonds to other water molecules in a tetrahedral configuration. On other hand, adhesion is the tendency of certain dissimilar molecules to cling together due to attractive forces (Comyn, 1997). There are several physical and chemical mechanisms which cause the adhesion between water and solid surfaces. Mechanical adhesion, chemical adhesion, dispersive adhesion, electrostatic adhesion and diffusive adhesion are the most important mechanisms for causing adhesion. The strength of the adhesion between water and the solid surfaces depends on which of these mechanisms occurs between them and also depends on the surface area over which they contact.

To be able to characterize the wetting phenomenon, first surface energy and contact angle will be defined. Then different wetting behaviour of surfaces will be discussed.

Surface Energy and Contact Angel

In wetting phenomena, the adhesive forces between water and solid cause a water drop to spread across the surface. The cohesive forces within water cause the drop to ball up and avoid contact with the surface. The contact angle (θ), is the angle at which the liquid-vapour interface meets the solid-liquid interface at equilibrium. The contact angle is determined by the resultant between adhesive and cohesive forces. The tendency of a drop to spread out over a flat solid surface increases as the contact angle decreases. Thus, the contact angle provides an inverse measure of wettability (Schrader, 1992; Johnson, 1993).

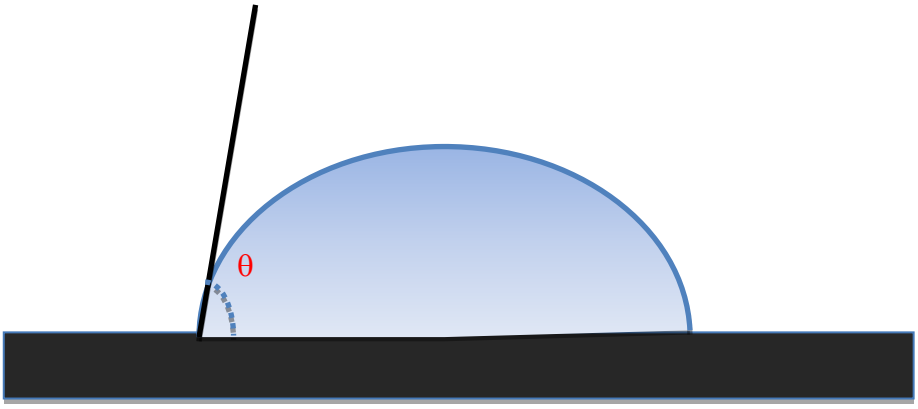

Figure 1-9 Schematic of definition of the contact angle

Figure 1-9 shows a schematic of how contact angle is defined for a single drop on a solid surface. The surface in this schematic figure is assumed to be ideal. This means that advancing and receding contact angles are equal. In reality the surfaces do not have perfect smoothness, rigidity or chemical homogeneity and such deviations from the ideal conditions result in phenomenon called contact-angle hysteresis (Robert, 1992) .Contact angle hysteresis is defined as the difference between the advancing contact angle (θ_a) and the receding contact angle (θ_r).

The advancing contact angle is the maximum stable angle, whereas the receding contact angle is the minimum stable angle (Johnson, 1993). In icing problems, even if it is assumed that the surface is ideal, there is a difference between the advancing and receding contact angles (Fortin, 2004). Here because of the aerodynamic forces acting on the surface of the drop, we cannot assume the drop is in the equilibrium state. Figure 1-10 shows the forces acting on the drop in the static condition, while Figure 1-11 shows the deformed drop (or bead as is called in the icing literature) due to aerodynamic forces (Fortin, 2004).

In icing problems the shape of bead has significant impact on final ice shape. The roughness developed over the surface is made from the water beads and other form of liquid water over the surface. It is understandable that small

changes in the liquid water shapes and characteristics can make different final ice shape over the geometry. In Fortin's work (Fortin, 2004) it is assumed that hysteresis is low and negligible. Sometimes it is useful to define average contact angle (θ_c) and use this angle as the contact angle for both advancing and receding contact angles especially when the hysteresis is low.

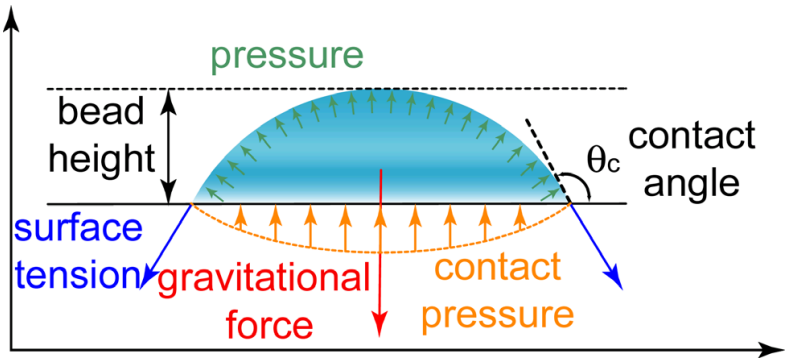

Figure 1-10 Forces on a drop in the static condition (Fortin, 2004)

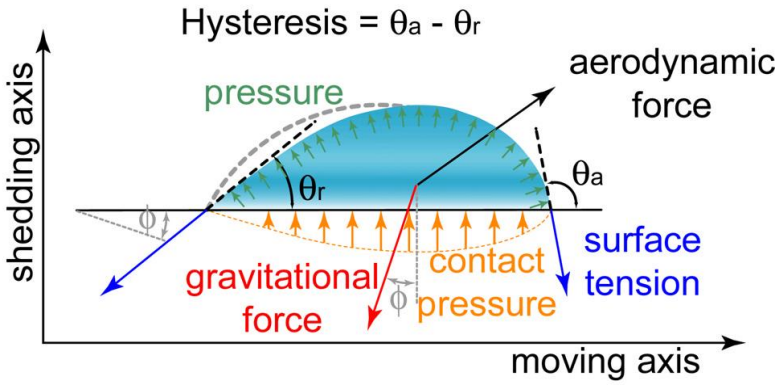

Figure 1-11 Deformed bead due to aerodynamic forces in icing problem (Fortin, 2004)

As said, the wettability or degree of wetting determines the balance of adhesive and cohesive forces. Adhesive force relates to the strength of water-solid interaction while cohesive force relates to water molecules interaction. Depending on the relative strength of adhesive to cohesive forces, four cases can be distinguished;

- If adhesive force is much stronger that cohesive force, the contact angle is close to zero ($\theta_c \approx 0°$) and the wetting is perfect.
- If adhesive and cohesive forces are in the same order, the degree of wetting is high and ($0° < \theta_c < 90°$).
- If adhesive force is weaker than cohesive force, the degree of wetting is low and ($90° < \theta_c < 180°$).
- If adhesive force is much weaker than cohesive force, the degree of wetting is perfectly non- wetting and ($\theta_c \approx 180°$).

In Figure 1-12 two of the different wetting conditions are shown. The left side of figure shows the low wettability condition, while the other one shows the high wettability.

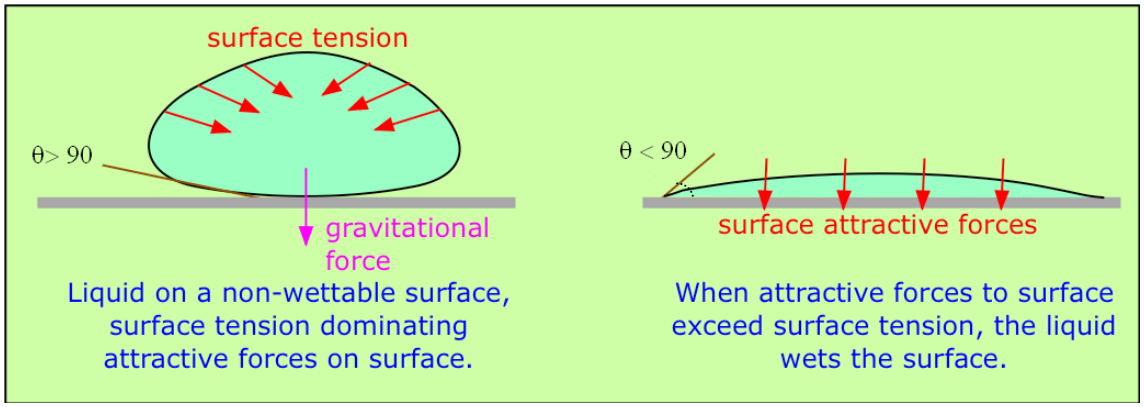

Figure 1-12 Different conditions of wetting (from www.chem1.com)

For water specifically other terms are used to describe the wettable and non-wettable surfaces. The term hydrophilic is used for wettable surfaces with low contact angles. The non-wettable surfaces are termed as hydrophobic. Water has high contact angles on this type of solid surfaces.

As discussed above, wetting, contact angle, hydrophilicity, and hydrophobicity are determined by the balance of the cohesive and adhesive forces. Thomas Young in 1805 was the first one who described the concept of surface energy in connection to the study of wetting behaviour. Surface energy quantifies the disruption of intermolecular bonds that occurs when a surface is created. In

other words, the surface energy is the excess energy at the surface of a material compared to the bulk. For liquids, the surface tension which is the force per unit length and the surface energy density are identical. Water has a surface energy density of 0.072 J/m^2 and a surface tension of 0.072 N/m.

Different Forms of Wetting

In this section a conclusion of modelling liquid water over the surface in an icing problem is given. Based on observations of Shin (1994) and Hansman (1987), three different zones can be used to describe the iced zone. They are a smooth zone, a rough zone and a feather region which are shown in Figure 1-13.

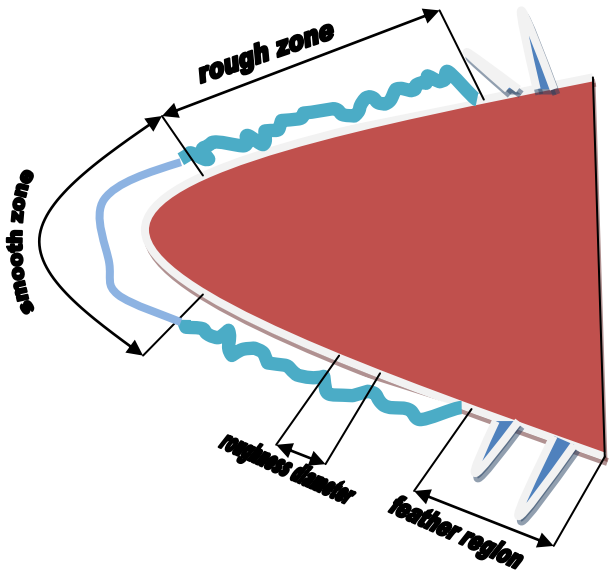

Figure 1-13 Different zones of iced surface due to water droplets impingement (Shin, 1994)

Fortin (2004) used an analytical model to represent the different observed zones in the icing problem. To represent all these zones, it is assumed that the liquid water on a surface can exist in three states which are as a continuous film, a rivulet, and as isolated beads. The continuous water film represents the

smooth zone, while beads represent a rough zone when droplets are impinging on the surface, and rivulets represent a rough zone where there are no droplets impinging on the surface. Figure 1-14 shows a schematic of this model. These assumptions have been modelled mathematically and added to the CIRA icing code (MULTI-ICE) by Fortin and his colleagues. The result of ice simulation using this modelling have slightly more accuracy when comparing to results from icing tunnel experiments (Fortin, 2004, 2006).

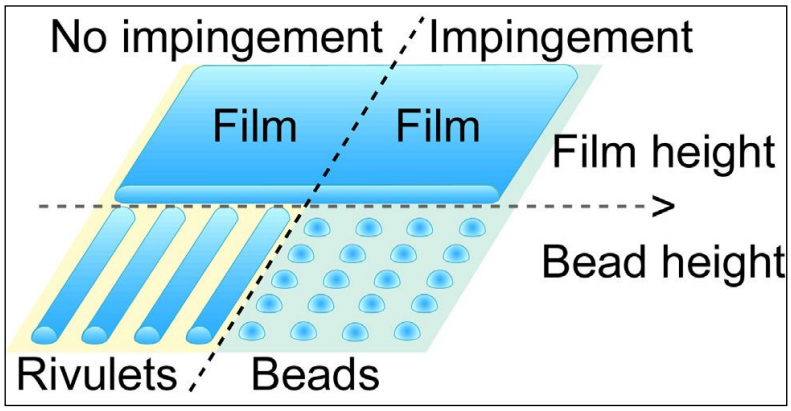

Figure 1-14 Different forms of water over the surface in icing problem (Fortin, 2004)

1.5 Previous Study on SLD Icing

Since the accident of ATR-72 turboprop and after the conclusion that SLD icing was the main reason of that accident, study of SLD icing has become an area of much interest of the icing community. Many experimental activities have been undertaken since 1996 when FAA organised an international conference on aircraft icing with special focus on SLD icing conditions. The consortium of EXTICE project (in the project summary and its motivation) concluded the major activities of the icing community worldwide on the SLD icing as follows:

- FAA organised an International Conference on Aircraft Icing in May 1996. The conference reviewed certification requirements, operating regulations, and forecast methodologies associated with aircraft icing

under varying environmental conditions, seeking to determine whether changes or modifications should have been made to provide an increased level of safety. As a consequence of this conference and to start the third phase, an in-flight Icing Plan was prepared with the aim of describing activities, rule-making, development and revision of advisory material, research programs and other activities which have already started or will be undertaken by the FAA in order to ensure safe operation in icing conditions. In addition to a revision of the certification regulations, FAA stresses the equal need for better icing forecasting, in-flight ice detection, training and guidance, and flight operations under icing conditions.

- Worldwide, a significant number of initiatives devoted to aircraft icing have been initiated, often in coordination with the FAA in-flight icing plan.
- Transport Canada organised a 'Standing Committee on Operations under Icing Conditions' which meets twice a year to co-ordinate the winter season, to share results obtained by various institutions and to generally co-ordinate and unify efforts.
- ALPA, the 'Air Line Pilot Association' formed an in-flight Icing Certification Project Team tasked with monitoring certification review and developing recommendations for change in both certification and operating rules with regard to in-flight structural icing.
- The 'Society of Automotive Engineers' (SAE) established the SAE AC-9C aircraft icing technology sub-committee.
- The Joint Aviation Authorities (JAA) established a Flight Study Group (FSG) for the development of the Notice of Proposed Amendment (NPA) 25F219 and in 1994 the NPA was raised as a FAA/JAA harmonisation item and the Flight Test Harmonisation Working Group has been tasked of reviewing the NPA 25F219. Even if these JAA activities were more addressed to flight requirements, the needs for efforts in the icing atmospheric area, SLD and aircraft icing certification were accepted by the European Community and by JAA. In 1996 the European research proposal, 'EURICE: EUropean Research on aircraft Ice CErtification'

received funding for two years from the European commission. The main problem raised within the EURICE project was that, while the existence of SLD has been proved, means of compliance and engineering tools to accurately simulate these conditions are lacking.

Also many researchers have studied the different aspects of SLD icing using both experimental and numerical tools. Nevertheless, there are a few researches which are applicable and useful for the real SLD icing problem. Only a few numbers of experimental facilities worldwide are capable of dealing with SLD icing in the range of speed comparable to the real icing conditions. Also in the numerical studies, there is small number of researches which studied the dynamic of impact of SLD in high speed.

The effects of SLD in the modelling of icing could be categorized in the three different categories based on the significance and importance of them (Wright and Potapczuk, 2004; Li *et al.*, 2009, Mingione, 2007).

Low significance phenomena

It has been discovered that the following phenomena have a negligible effect on the simulation of ice shape in the SLD conditions. This is based on the numerical simulations results with and without taking in account the effect of these phenomena. Also one can investigate the importance of the different phenomena by calculating the corresponding non dimensional parameters for each of them as it will be discussed.

- Basset force: it is the forced caused by the changes of droplets drag with time which is also called the drag history term. This term is negligible when the viscosity of the surrounding fluid is much less of the viscosity of the droplet. However, for flow with high velocity gradients this term can significantly affect the droplets trajectories and it could be larger than drag force which is the main driver of droplet trajectory in the most conditions. Thomas (1992) studied the effect of Basset force on the motion of small particles crossing an oblique shock wave. He showed the relation between the velocity gradients through the shock wave and the

effect of Basset force on the motion of the particles. The acceleration of particles in that particular case was in order of 10^8 m/s^2 which is much higher than acceleration of droplets in the icing problem. In the icing problem as the surrounding fluid is air and the droplet fluid is water, the ratio of the viscosity is in order of 100 ($\mu_{water}/\mu_{air}\approx100$). Also the droplets acceleration in typical icing problem is in order of 10^3 m/s^2 which is much lower of what was suggested by Thomas (1992).

- Lift force: it is the lift force acting on the droplet while it is approaching the surface of the aircraft. This term is more important if the density of the surrounding fluid is much higher than the droplet density. In the case of icing, the density of the droplet is three orders of magnitude larger than surrounding fluid ($\rho_{water}/\rho_{air}\approx1000$) and subsequently the lift force is extremely negligible.
- Gravitational effect: the effect of the gravity on the dynamic of the droplets and their trajectories is negligible in the range of droplet size and velocities in the SLD icing. The ratio of the inertial force of the droplet to the gravity force is represented by the Froude number and it is defined as ($Fr = V^2/gd$). This number for the typical SLD icing is in order of 10^6 and this shows the relatively low importance of the gravity effect in the dynamics of the supercooled larger droplets.

Phenomena with medium significance

Some of the phenomena in SLD icing have second order effect and they should be considered for high accuracy simulations. They are (but not limited to):

- Droplet deformation: in the case of the large droplets and high velocity, the droplets are deformed from the initial spherical shape and this can cause different drag force from the assumption of spherical droplet. It has been shown that in the extreme cases, the maximum increase in the drag force is about 15% (Wright and Potapczuk, 2004). However, this increase in the drag force has a negligible effect on the collection efficiency (less than 1%) of the

surface but it could have more significant effect on the splashing of the droplet after impact on the thin water film (Quero, 2006).

- Droplets interaction: in the high values of LWC, the density of droplets is higher and it is more likely that droplet interact with each other while they are approaching the aircraft surface. This could result in the overall drag force on the droplets and this phenomenon has been studied experimentally and numerically (using Direct Numerical Simulation methods) for the case of heavy rains when LWC is greater than 3 g/m^3. The drag force showed a decrease of 5% but in the lower LWC (where the usual icing events happen) this effect was negligible (Mulholland *et al.*, 1988; Smyrnaios, *et al.*, 2000). This effect is more important near the solid surfaces where there is higher possibility of interaction between the incoming droplets and ejected droplets after the splashing.
- Droplet breakup: when the shear forces of air are high enough to overcome the surface tension of a droplet, that droplet will breakup to smaller droplets. This phenomenon is characterized by Weber number which is the ratio of the inertial force of a moving droplet to the surface tension force of it ($We = \rho_{air} V^2 d/\sigma$). When the Weber number is greater than 12, the water droplet will breakup in air to smaller droplets (Luxford, 2005). This phenomenon has important effect on the collection efficiency of the surfaces especially on the multi element wings (wings with slat and flap). It also is important to consider the breakup of droplets for the splashing modelling, as the smaller droplets have different behaviour when impacting a thin water film.

High significance phenomena

It is widely accepted within the icing community that splashing of large droplets is the more significant effect in the SLD icing. In the SLD icing, both the droplet size and droplet impact velocity are relatively high and the inertial force of the droplet overcomes the surface tension and surface viscosity of the droplets.

This will result in splashing of the droplet to smaller droplets which are ejected in the air field. The splashing is characterized with both Reynolds number ($Re = \rho_{water} Vd/\mu_{water}$) and Weber number ($We = \rho_{water} V^2 d/\sigma$) which show the ratio of inertial force to the viscous force and surface tension, respectively. The Ohnesorge number ($Oh = \sqrt{We}/Re$) is often used in experimental study of the splashing which is a combination of the Reynolds and Weber numbers (Mundo *et al.*, 1995).

Many correlations have been developed based on the experimental study of the splashing process, although most of these correlations are based on the experimental conditions out of the range of icing problem (Wright and Potapczuk, 2004). The outcome of the correlation usually is the velocity (magnitude and direction) of the secondary droplets, the ratio of the mass splashed after the impact to the total mass of the incoming droplets and the size of the secondary droplets.

A series of experimental activities has been undertaken at Cranfield icing facilities to study the impact of high speed large droplets on the thin liquid water film (Quero *e. al.*, 2006). Purvis has developed a numerical tool based on Volume of Fluid (VOF) modelling to simulate the impact of the large droplet into thin water film. The comparison between the simulation results and numerical modelling showed interesting agreement between the inviscid VOF model and the experimental measurements (Quero, 2006). More details of the modelling of impact of large droplets on thin water film are discussed in chapter four of this thesis.

1.6 Modelling the Water Film Dynamics and Solidification using LBM

The Lattice Boltzmann method is one of a family of computational methods based on particle kinetic theory (Succi, 2001). In this method the main parameter is the particle distribution function (PDF) which can describe the state of the system in conjunction with velocity space. In recent years this method has been developed and used widely in different areas of science and

technology (Sukop and Throne, 2006). The advantages of LBM which, make it a popular and efficient method, can be summarized as following:

- The governing equations are linear and mathematically simple
- It needs simple grids
- It is suitable for complex geometries
- It is very strong in modelling multi phase and multi component problem
- Its spatial accuracy is second order
- It is explicit and time accurate
- It has outstanding efficiency in parallel computing

We believe that these features of the LBM make it a suitable alternative to model the aircraft icing problem.

The most general form of transport equation is Boltzmann equation which can be written as Equation (1-2). This equation was introduced for first time by the famous scientist Boltzmann.

$$\frac{\partial f}{\partial t} + \vec{c}.\nabla_{\boldsymbol{x}} f + F.\nabla_{\boldsymbol{c}} f = \Phi(f) \qquad \textbf{(1-2)}$$

Where f is the particle distribution function in space and time, F is the external force applied to the system, $\vec{c}$ is the velocity space and Φ is the collision term. The discrete form of the Equation (1-2) can be used when a finite set of velocities are considered instead of infinite possible velocities and directions for the particle movement. The collision term is modelled by the idea of Bhatnagar–Gross–Krook (BGK) which considers the collision term as the tendency of system to get its equilibrium state (Succi, 2001). The details of the equilibrium distribution function are given in several LBM textbooks (Succi, 2001)

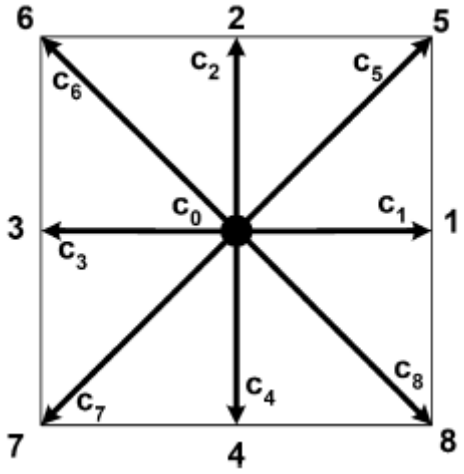

Figure 1-15 D2Q9 lattice used for the current LBM flow solver

It has been discussed that the solidification modelling and the associated difficulties caused by the geometry modification, are one of the big challenges for icing codes developers (Gent, 2000). The new idea is developed in this work to use LBM framework to model the process of the solidification in icing problem. The lattice Boltzmann method has been used widely in the recent years to model the solidification and melting for different applications including alloys processing (Semma *et al*, 2007) and crystal growth (Succi, 2000).

The first step to model the solidification is to model the thermal problem in the system. The LBM framework discussed in the beginning of this section is able to model the hydrodynamic aspects of the system but the system is assumed to be isothermal. There are several approaches to model the heat transfer and thermal problem using LBM.

- Multispeed Model
- Modified Collision Term
- Using another Distribution Function

The third approach has the minimum of numerical instabilities and it is used widely especially to model flow thermodynamics in the incompressible regime (He *et al*, 1998). In this approach another particle distribution function is used to model the temperature in the lattice.

The second part of solidification modelling is to consider the phase change problem from the liquid phase to the solid phase. One of the advantages of LBM is that this method can deal with the forming of new solid particles without any need to modify the grid and the geometry. The phase change process is considered to take place in a small range of temperature (typically 5% of total temperature change in the system) around the freezing point and in this zone the combination of the liquid phase and the solid phase is treated like a porous medium to model the resistance the flow would face because of solid phase. The details of the method and its implementation are discussed in chapter six.

2 Experimental Study of Thin Water Film Dynamics

2.1 Cranfield Icing Facilities

This research has been undertaken using the icing tunnel facilities at Cranfield University. Figure 2-1 shows a schematic of these facilities. There are two icing tunnels, vertical and horizontal. The horizontal tunnel has the larger test section and is used to study overall icing problems. This tunnel is used to model the real condition of icing happens for the airplanes. The vertical tunnel has very gentle converging geometry and it avoids breakup of large droplets. This tunnel is used to study SLD icing and fine scale phenomena in icing process. All the experiments of this work have been performed in the vertical icing tunnel.

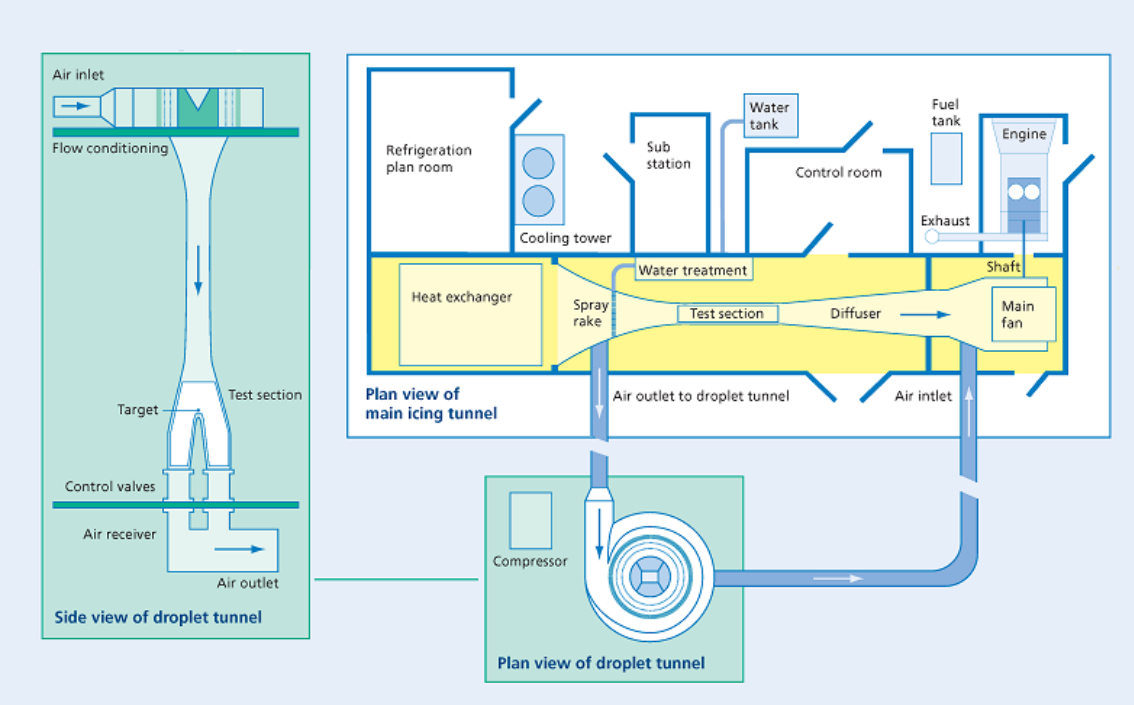

Figure 2-1 Cranfield Icing facilities [courtesy of Cranfield University]

This facility is able to launch droplets in the size range 20 to 2,000 microns at a target at velocities up to 90 m/s in an air flow. The droplet tunnel has a vertical

contraction of a design to minimise droplet break-up and a working section able to mimic the flow field near an aerofoil and favourable to imaging tasks.

Figure 2-2 the droplet generator and the mechanism of steering the droplet generator (Luxford, 2005)

The general construction of the droplet generator, which was used for generating a jet of water in the vertical tunnel, is shown in Figure 2-2. This droplet generator was developed in house as nothing commercially available appeared to be practical for this particular application (Luxford, 2005). Water is forced through a precision orifice (an electron microscope aperture). The pressure of the water is modulated using a series of piezoelectric elements to help synchronize the water jet breakup into a stream of mono-dispersed droplets. The generator permitted a relatively fast changeover of the orifice and driving frequency to deliver different sized droplets. The generator was mounted on a motorized translation stage at the top of the tunnel and the entire installation was kept a few degrees above freezing point (Hammond, 2005).

2.2 Set up of the Experiments

A flat polished Aluminium plate is used as a target to perform the experiments on the water film dynamic. Aluminium and its alloys are widely used on the surface of the aircraft and typical icing experiments are performed on this type of material. The surface was polished using a 1200 grit SiC (Silicon carbide)

grinding paper. In order to characterize the surface of the target, we have measured the contact angle of a water droplet in the static condition. The equilibrium contact angle in the static wetting is used as a characteristic of the surface in the dynamic wetting, when water flows on the surface in the different regimes.

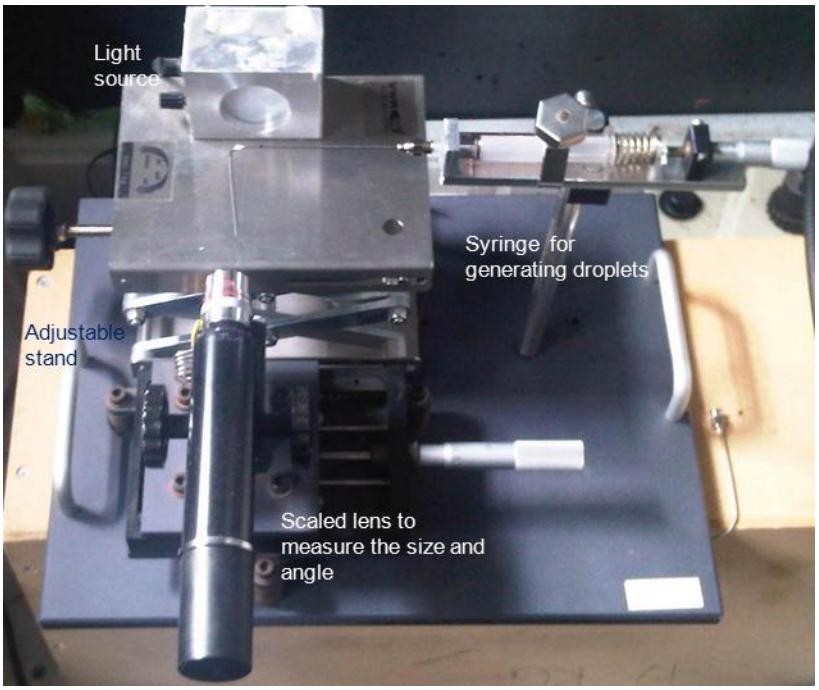

Figure 2-3 the experimental setup for the contact angle measurements

Figure 2-3 shows the experimental setup used to measure the contact angle of water on the different surfaces. In the process of measuring the contact angle, a range of angles can be observed in the triple contact point. In the two limits of this range, two different angles could be distinguished. When the droplet is formed on the surface, the contact angle is called advancing angle (θ_a) and when the droplet is removed from the surface the contact angle is called receding angle (θ_r). The equilibrium contact angle is expressed in term of advancing and receding angle as (Schrader, 1992; Johnson, 1993):

$$\theta_c = \cos^{-1}\left(\frac{\cos(\theta_a)\, d_a + \cos(\theta_r)\, d_r}{d_a + d_r}\right) \quad \textbf{(2-1)}$$

Where, d_a and d_r are the droplet size in the advancing and receding phases, respectively. For the aluminium polished surface used for the experiments, the contact angle was measured to 43º. This parameter is utilized as a measure to characterize the surface used in the experiments. This parameter was changing dramatically for the same surface depending on how clean and polished the surface is. For this reason, the target was cleaned and polished before any set of experiments.

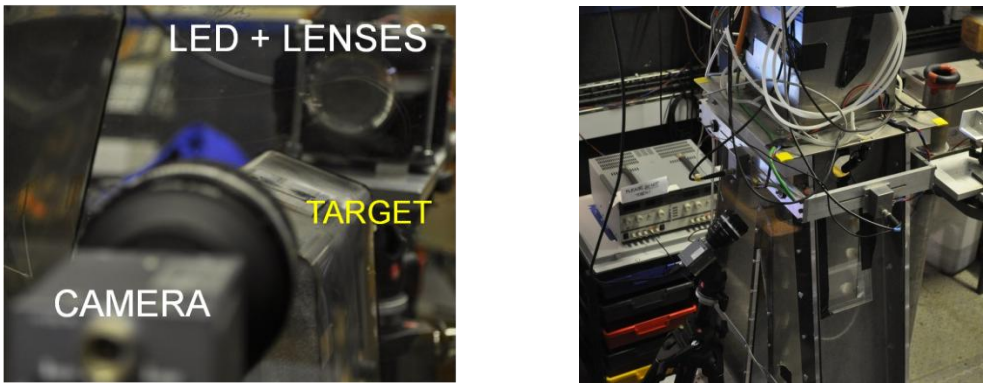

Figure 2-4 the arrangement of the target and the imaging system in the Vertical icing tunnel

Figure 2-5 shows the CCD (charge coupled device) camera chosen for imaging system along with a very short flash duration LED (up to 50ns) as the source of light for the imaging. The short flashing guarantees freezing of motion in each frame of images and avoid overlapping the different events during high speed impact of the droplets into water film. The most important features of this camera are the high resolution with small pixel size (3.75 micron) and high rate of connection to the host computer system. More details about LED (Light Emitting Diode) flash system and are given by Luxford (2005). This imaging

setup is used to study the features of the water film on the target in the vertical icing tunnel.

A green laser pointer with wavelength of 532 nanometre and 200 miliWatt power is used for forming a laser sheet (with a combination of appropriate lenses) in the cross section of the vertical icing tunnel in order to illuminate the incoming droplets. This technique is used to measure the local LWC above the target in the tunnel.

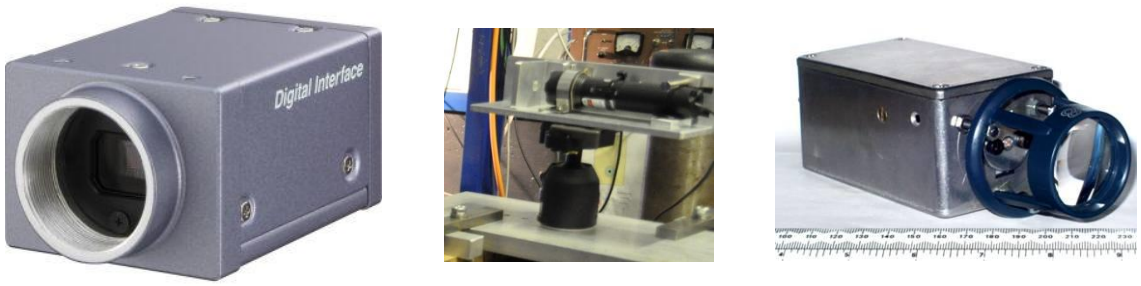

Figure 2-5 CCD camera (left), laser system (middle) and LED system (right)

The basic relations of lenses were used to predict the appropriate arrangement for the imaging system. These relations are found to predict the actual magnification of the lens with about 10% relative error. These relations are quite accurate for the parabolic single lens and this can explain error occurred in prediction of the magnification of a multi component lens using these relations. The basic relations for a single parabolic lens are as follows:

$$\frac{1}{f} = \frac{1}{p} + \frac{1}{q} \qquad \textbf{(2-2)}$$

$$M = q/p$$

Where, f is the focal length of the lens, p is the distance between the centre of the lens to the object, q is the distance of the image to the centre of the lens and M is the magnification of the lens. We have used a 50mm for the experiments and it was found to give reasonable magnification and clear imaging. For the arrangement of Figure 2-6 the parameters p and q are calculated as:

$$p = L + s + d, \qquad q = C - d \tag{2-3}$$

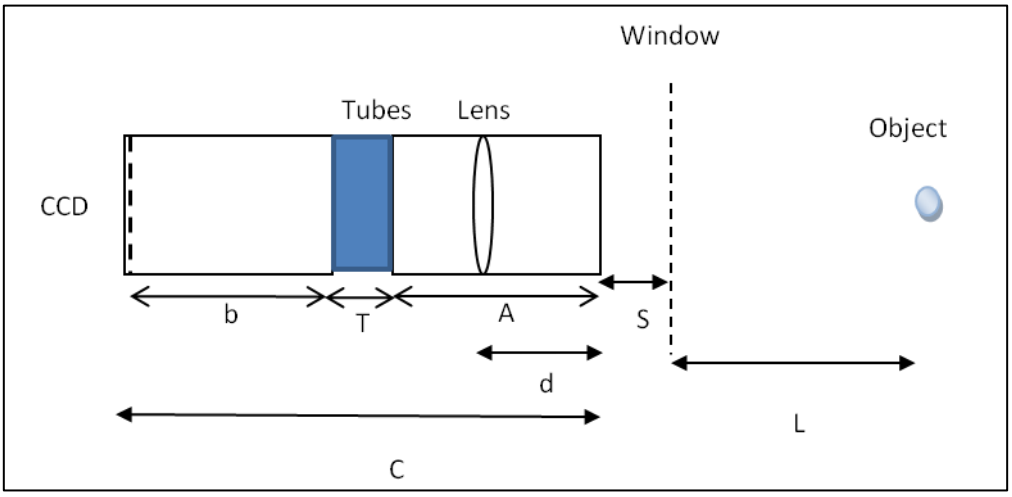

Figure 2-6 Schematic of the arrangement of the CCD camera and lens

However, for more accurate scaling of the images, which is important for measurement purposes, for any arrangement of imaging system an image was taken from a known-size object in the location of the interest on the target. When it was compared to the image on the screen of the computer, the actual magnification is calculated and was used to scale the images taken from the experiments.

2.3 Airflow Calculation of the Vertical Icing Tunnel

When the droplet impact, splashing and water film dynamics are studied, it is necessary to understand and take in account the surrounding airflow field. Specifically the dynamics of the water film is dominated by the airflow shear stress. Fluent is a commercial CFD software and used here to predict the airflow field in the vertical icing tunnel and especially around the target, where the water film is formed and the droplet impacts take place.

The full scale icing tunnel has been modelled in order to obtain a two dimensional CFD simulation in the tunnel from the inlet in the top to the bottom of it. The purpose of these calculations is to determine the pressure and velocity distribution around the target and to find the shear stress distribution on the target. These calculations are used to estimate the water film thickness, which flows over the target, as it will be discussed in the chapter three.

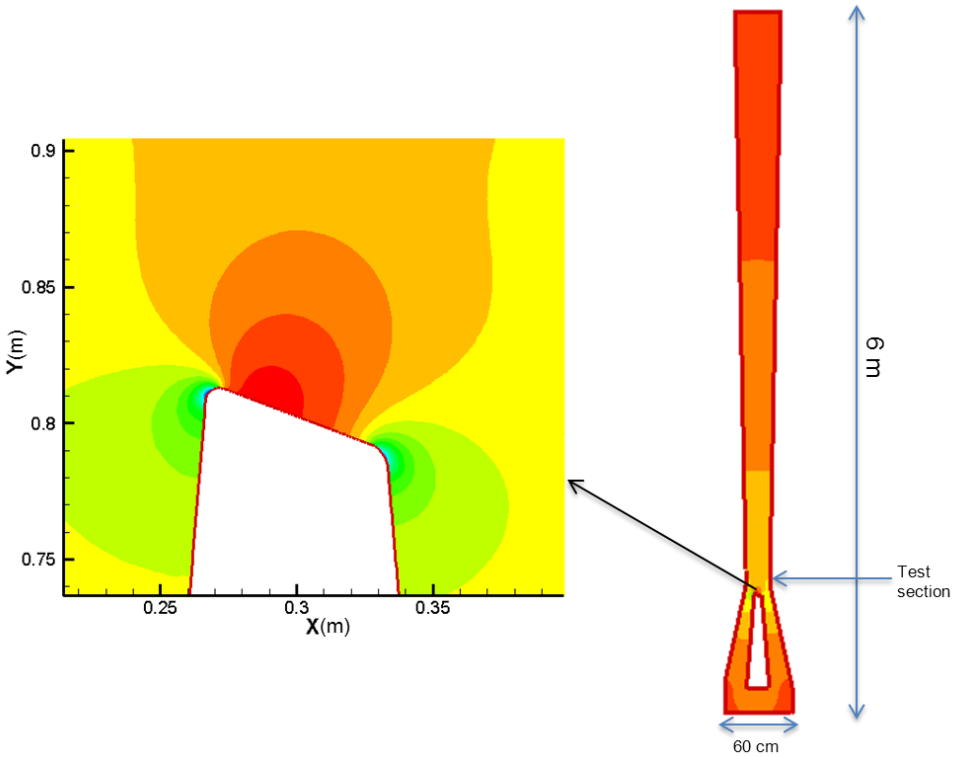

Figure 2-7 Pressure contours around the target (left) and pressure contours in the simulated part of the vertical icing tunnel (right), V_{air}=80 m/s

Speed calibration

The CFD calculations are made to investigate the air flow field around the target. Therefore the values of the boundary conditions in the CFD calculations should be set in such way to specify the velocity in the test section. We have set the inlet air velocity at the top of the vertical icing tunnel in order to control the air velocity in the test section (14 cm above the centre of the target) CFD modelling has been used to find the relation between the inlet velocity and the velocity in the test section. The ratio of velocity in the test section to the inlet velocity was found to be about 1.88 for the test section velocity range of 30 to 80 m/s.

The velocity in the test section is measured using a pitot static probe connected to a high accuracy digital microbarometer. The velocity was measured based on the difference between the total and static pressure in the test section. In the same test section a series of images were taken to measure the velocity of the droplets (maximum deviation of 10%). It has been found that the velocity of the droplets is close to the air velocity reading. This means that they have enough time and distance to move in the air field to achieve their equilibrium velocity which is the velocity of the air itself. One of the bases for design of the vertical icing tunnel was to meet this criterion (Luxford, 2005). Figure 2-8 shows typical images used to measure the droplets velocity in the test section of the icing tunnel. The CCD camera and LED flash were synchronised in such a way that any image contains three light flashes. Therefore, if a droplet is in the imaging area it would appears three times in the image. As we know the time interval of flashes and the scale of the image, the velocity of droplets can be calculated. More than 20,000 images have been analysed in order to verify that the droplets reach their equilibrium velocity.

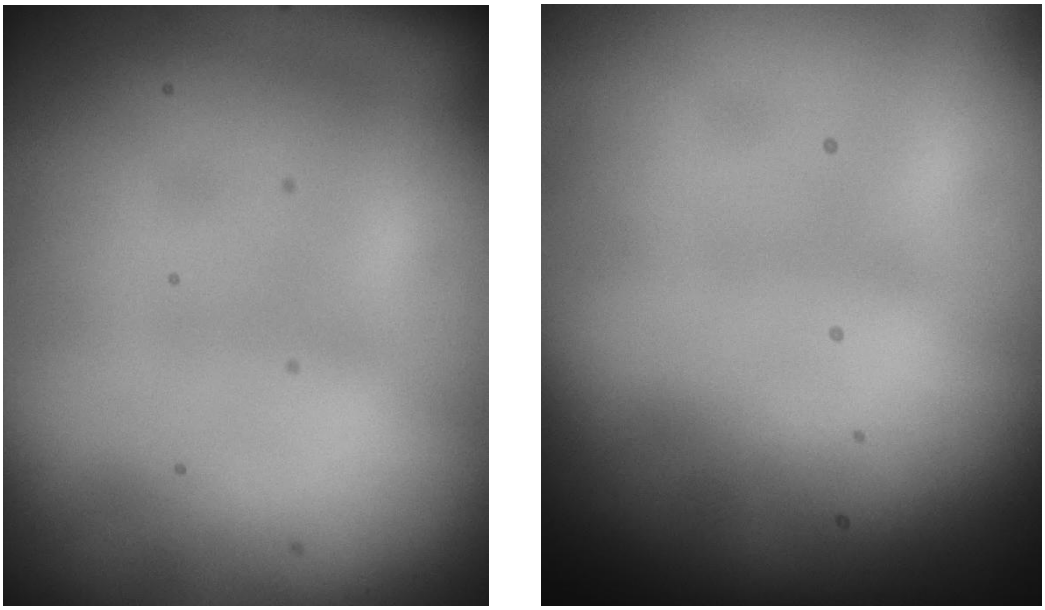

Figure 2-8 Typical images used to measure the velocity of the droplets in the test section of the vertical icing tunnel

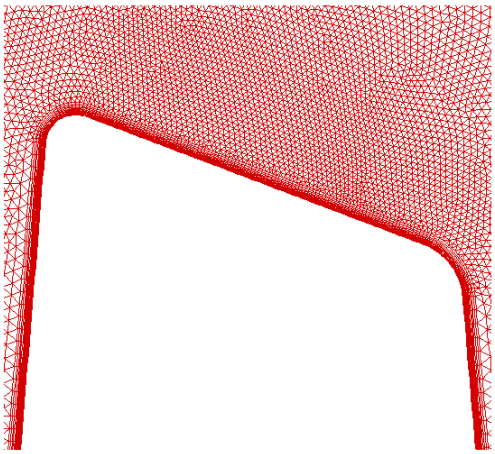

Figure 2-9 the grid used for CFD calculations

Boundary layer calculations

The main purpose of the CFD modelling in this stage is to predict the shear stress on the target in order to estimate the thickness of water film moving on the target due to the air shear force. The Reynolds number of the air flow in the tunnel is greater than 10^5 (based on width of the test section) in all conditions of the experiments. This suggests that the flow is completely in the turbulent regime and to capture the boundary layer, a fine mesh is needed near the walls.

Figure 2-9 shows the grid is used for the CFD modelling of the vertical icing tunnel.

The standard k-ε turbulence modelling with enhanced wall treatment is used to model the turbulence airflow. This model has proven capability to capture the air boundary layer in the incompressible flow regime (Wilcox, 2006). It is also capable of modelling the thermal effect and effects of pressure gradient on the boundary layer development. Generally high Reynolds number k-ε turbulence models (including the model we used) need wall functions to adequately capture the boundary layer near the solid walls. These models have difficulties around stagnation points where both the shear stress and the boundary layer thickness vanish and also they are generally not suitable for heat transfer prediction. Another family of k-ε turbulence models called Low Reynolds Turbulence Models[1] are more capable of capturing the boundary layer in vicinity of stagnation points. However here we are more interested in the area on the target, which is relatively far from the stagnation point, and this allows us to use standard k-ε turbulence model with enhanced wall treatment to capture the boundary layer.

The first layer of the grid (δ_0) should be small enough to capture the thin turbulent boundary layer. Equation **(2-4)** shows a semi empirical relation to

[1] Low Reynolds number means corresponds to the local flow near the walls where the flow speed is low and not to the global flow which has high Reynolds number anyway as it is turbulent

choose a suitable value for the first layer thickness. This equation is based on rough estimation of the boundary layer thickness for the largest length scale on the target (L). It is also assumed that the boundary layer is captured by ten mesh points in the normal direction on the target (Wilcox, 2006). For all CFD modelling here δ_0 is set to 10μm. This value satisfies Equation **(2-4)** for all range of velocities from 30 to 80 m/s.

$$\frac{\delta_0}{L} \leq \frac{1}{10\sqrt{Re}} \qquad \textbf{(2-4)}$$

Once the CFD simulations are made, the dimensionless turbulent wall distance should be calculated to make sure that it is in the right values region. For the turbulence modelling used here this parameter should not be larger than 5 to achieve accurate boundary layer prediction (Wilcox, 2006). Figure 2-10and Figure 2-11 show the variation of y^+ on the target for the complete range of velocities and target inclination used in the simulations. The maximum value of y^+ is about 2.5 and this mesh spacing is small enough to model the turbulent airflow around the target. It should be noted that y^+ could not be estimated before the simulation as it depends on the local shear stress on the target. Equation **(2-4)** is used to prevent trial and error between the mesh generation and CFD simulation in order to find the appropriate mesh spacing.

The boundary layer thickness on the target is calculated by measuring the location of 99% of stream velocity. Figure 2-13 and Figure 2-14 show the variation of air boundary layer thickness versus the air velocity in the test section. In Figure 2-12 an example of the air velocity vector around the stagnation point on the target is shown.

It must be noted that for CFD modelling we assumed here that the target is smooth and we neglected the effects of the waviness of the water film on the airflow field. The rationale behind this assumption is that the typical water film thickness is one order of magnitude smaller than air boundary layer thickness,

therefore for first order estimation we can neglect these effects. However in reality the waves on the water film act as small roughness on the wall and they affect the boundary layer thickness. The boundary layer in this case would be thicker than the case of clean and smooth wall.

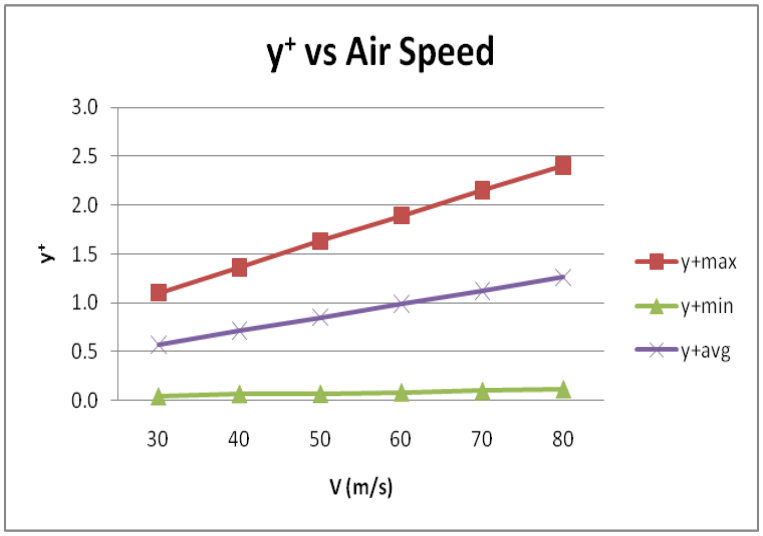

Figure 2-10 Variation of y^+ on the target for different air speed, impact angle=70º

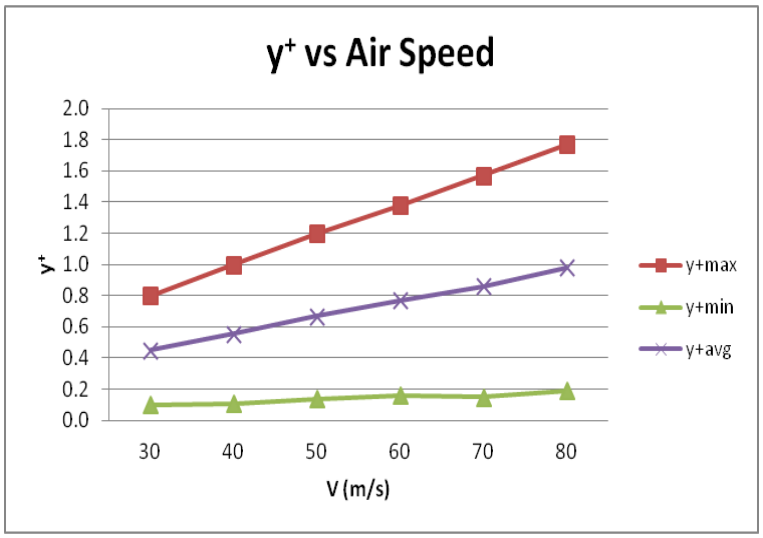

Figure 2-11 Variation of y^+ on the target for different air speed, impact angle=45º

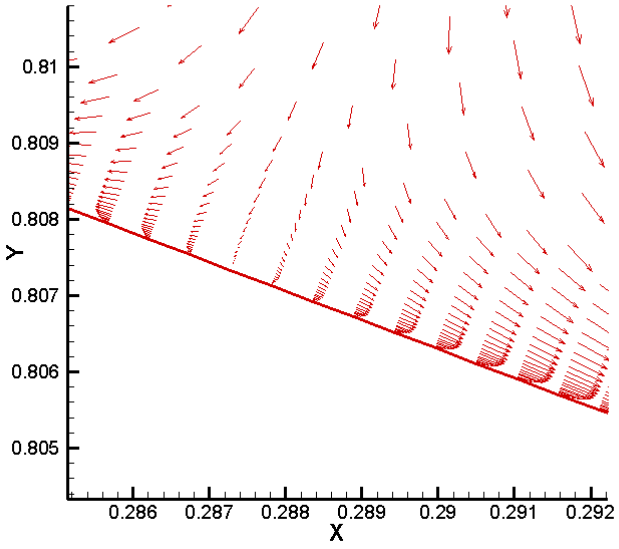

Figure 2-12 Boundary layer on the target around the stagnation point, V_{air}=80m/s (arrows layout and directions indicative of velocities)

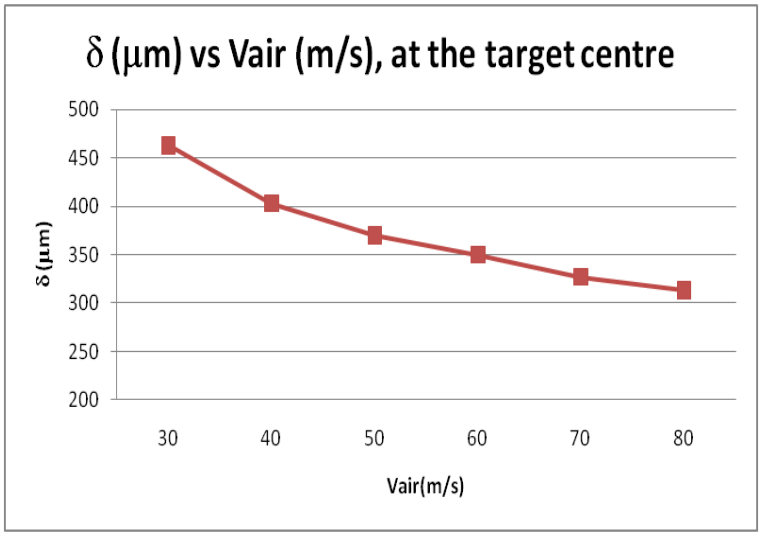

Figure 2-13 Boundary layer thickness in the middle of the target for different air speed, impact angle=70º

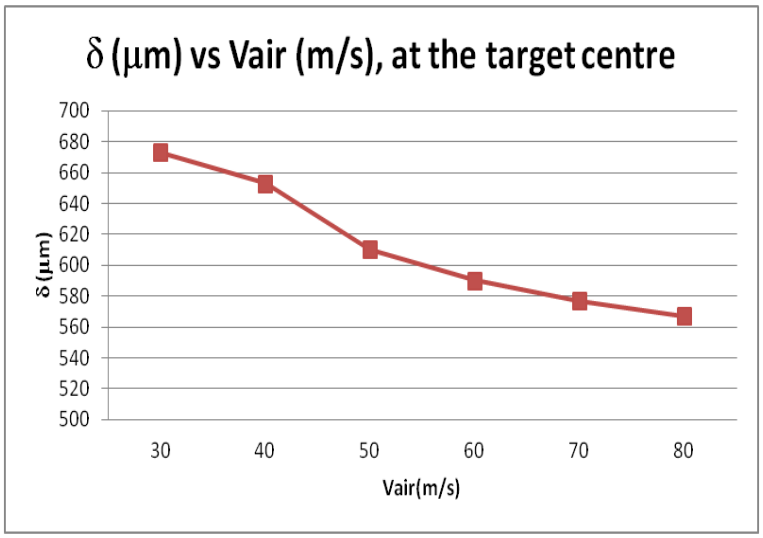

Figure 2-14 Boundary layer thickness in the middle of the target for different air speed, impact angle=45º

The wall shear stress distribution is calculated based on the normal distribution of the air velocity on the target for different conditions. The calculated shear stress for different air velocities in the test section are given in Figure 2-15. The horizontal axis is the distance from the stagnation point which has the minimum shear stress.

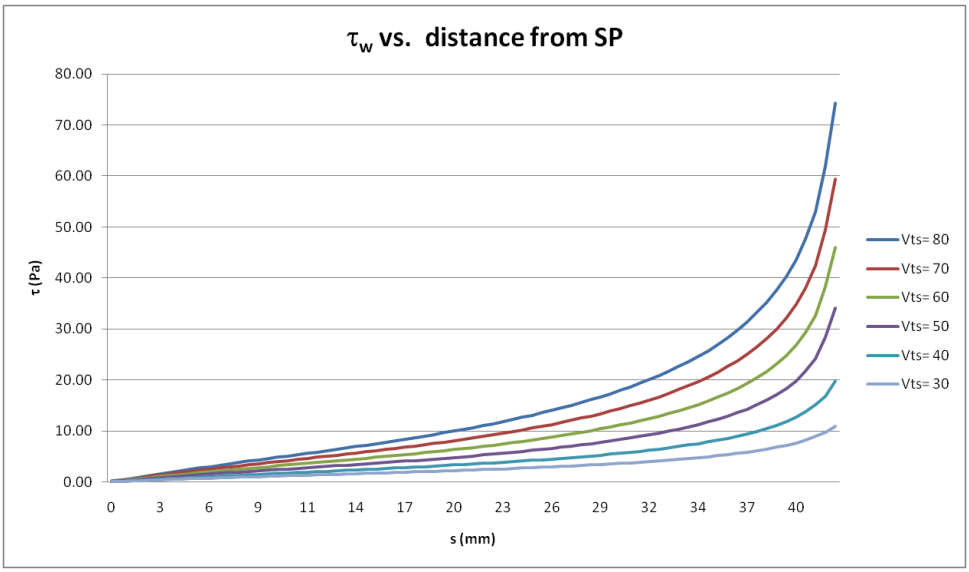

Figure 2-15 Shear stress distribution on the target (vs. distance from the stagnation point) for different air speed, impact angle=70º

The location of the stagnation point can be observed directly in the experiments in presence of the droplets spray. Figure 2-16 shows how different air flow direction can change the form and appearance of the splashing. The effect of the flow direction on the water film and splashing feature was used to estimate the location of the stagnation point on the target. The observations were in good agreement with the CFD calculations (in a few millimetres range). The location of the stagnation point in the CFD calculations was determined by finding the position of point with minimum shear stress on the target.

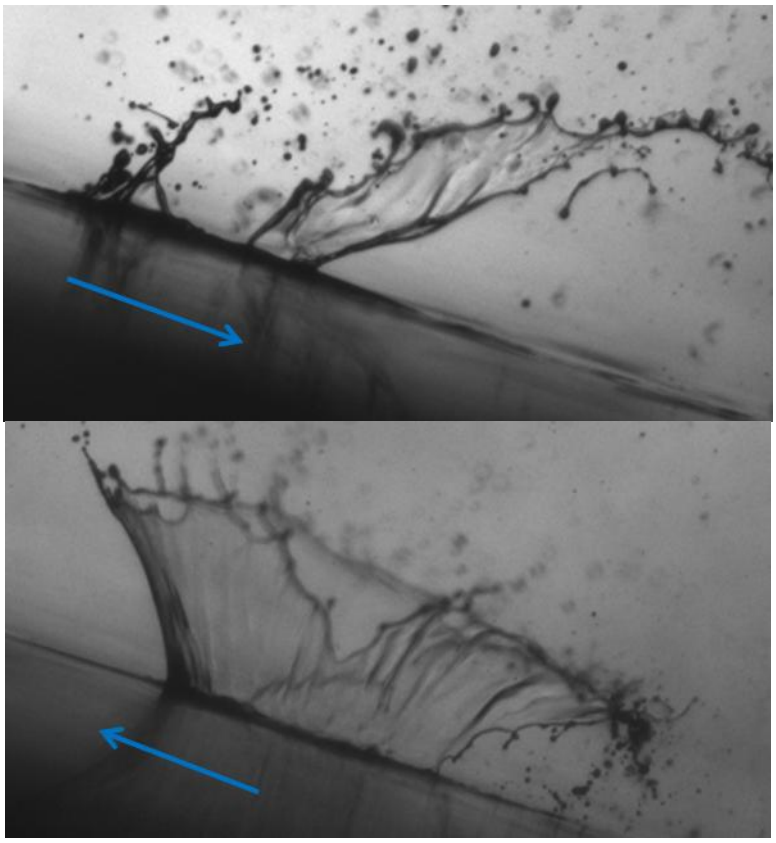

Figure 2-16 Different water film direction and splashing features depending on the air flow direction

Table 2-1 Summary of CFD calculation (shear stress and air boundary layer thickness in the middle of the target) for two inclination angles 45º and 20º

Case	V(m/S)	Inclination	τ_c (Pa)	$\delta_{air}(\mu m)$
1	30	45° Impact angle=45°	2.51	673
2	40		3.78	653
3	50		5.31	610
4	60		7.04	590
5	70		9.01	577
6	80		11.25	567
7	30	20° Impact angle= 70°	1.67	463
8	40		2.32	403
9	50		3.23	370
10	60		4.22	350
11	70		5.34	327
12	80		6.65	313

For estimating the water film thickness, the average shear stress on the target is used. The maximum and the average values of the shear stress on the target are given in graphs of Figure 2-17.

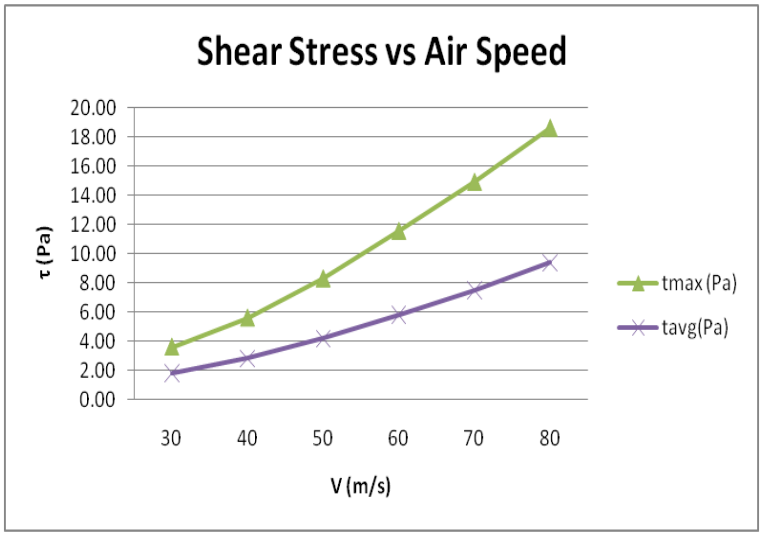

Figure 2-17 Maximum and average wall shear stress on the target for different air speed, impact angle=70°

2.4 Observations and Measurement of Thin Water Film

Three features for the thin water film have been studied experimentally: the water film velocity, wave celerity and its wavelength. The stability of the water

film for the different conditions has been studied to find a threshold for transition from continuous water film to non-continuous form. Water film velocity, wavelength and wave celerity are measured by comparing the sequence of images taken from continues water film flowing over the surface of the aluminium target.

2.4.1 LWC Measurement

The Liquid water content has significant effect on wetting condition and consequently the water film and icing characteristics. This parameter must be under control in order to study its effect on the water film. To measure overall LWC in the wind tunnel the wetted area of the test section is measured. This measurement was done by direct observation using a light source to estimate the wetted area dimension in the test section. Figure 2-18 shows the variation of the overall LWC versus the air velocity. Equation **(2-5)** is used to calculate the overall LWC in the test section.

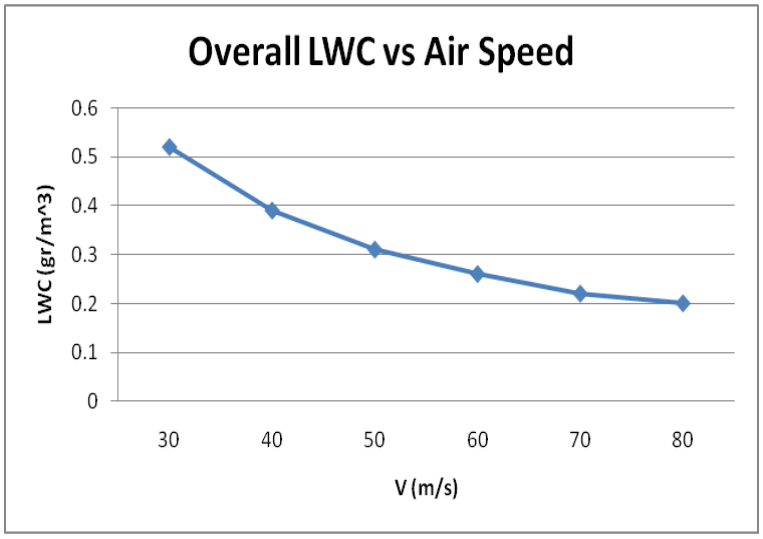

Figure 2-18 Measured overall LWC vs. air speed

The overall LWC on the test section of the icing tunnel can be calculated as:

$$LWC = \frac{\dot{m}_w}{\left(\frac{\dot{m}_w}{\rho_w}\right) + \left(\frac{\dot{m}_{air}}{\rho_{air}}\right)} \approx \frac{\dot{m}_w}{\dot{m}_{air}/\rho_{air}} = \frac{\frac{\pi}{6} d^3 \rho_w \dot{n}}{VA} \quad \textbf{(2-5)}$$

Where, $\dot{n}$ is the frequency of the incoming droplets, ρ_w is the density of water, d is the droplet size, V is the air velocity and A is the area of the total wetted area. A proper constant is used in equation **(2-5)** to convert the unit of LWC to (g/m^3) as it is common in icing study to express LWC in this unit. To obtain overall LWC the wetted area must be measured for any case. For the purpose of our experiments we have estimated the wetted area by the observation only.

To achieve a better accuracy in the measurement of the LWC, the local water concentration has been measured and used for study of the liquid water film dynamic. We have used a laser sheet to illuminate the droplets in the test section and the local LWC over the centre of the target is measured by counting the number of illuminated droplets. The CCD camera and a high resolution NIKON camera have been used to take images from the test section of the tunnel to capture the pattern of the droplets in the test section. Thus the local LWC is estimated as:

$$LWC = \frac{\frac{\pi}{6} d^3 N \rho_w}{VA\Delta t} \quad \textbf{(2-6)}$$

Where, N is the number of droplets in each frame and Δt is the exposure time of the camera which has been set to (1/30 sec) for all the measurements. Results of the local LWC measurements showed that LWC is changing with time and it is oscillating about a mean value which is considered for the purpose of analysis.

Figure 2-19 shows the variation of the measured local LWC with time for case of V=70 m/s and d=400 μm. The average value of LWC over the time (about 11

sec) is 0.58 g/m^3. This value is much higher than the overall LWC estimated for this velocity (Figure 2-18). The reason is that the water concentrate is higher in the middle of the test section when the droplet generator is pointed to the centre of the test section.

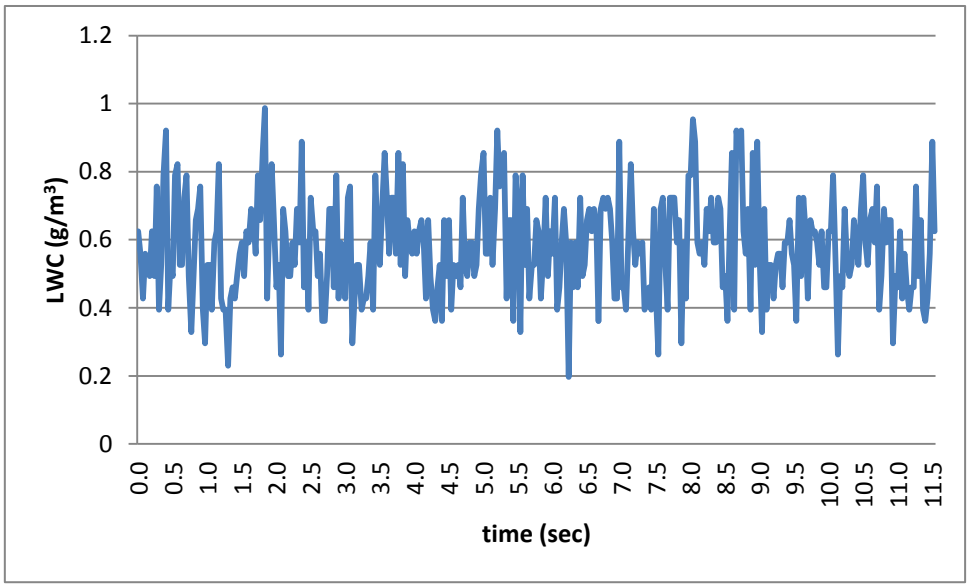

Figure 2-19 the variation of measured LWC with time in the vertical icing tunnel for V= 70 m/s and d=400 μm

The values of LWC in Figure 2-18 and Figure 2-21 are for the case of pointing the droplet generator to the middle of the test section. By changing the angle of the droplet generator we can achieve different values of LWC for the same velocity and droplet size. Because of sensitivity of LWC to change in position of the droplet generator, the LWC has been measured particularly for any experiment.

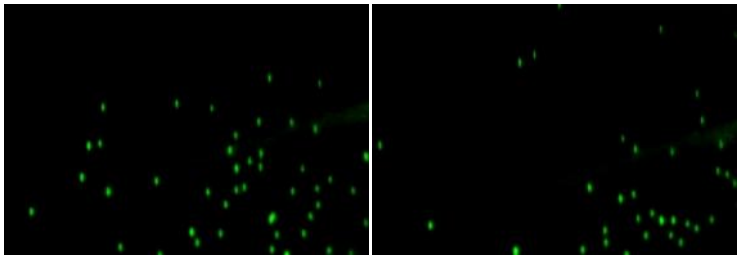

Figure 2-20 Sample of pattern of droplets in the test section of the vertical icing tunnel

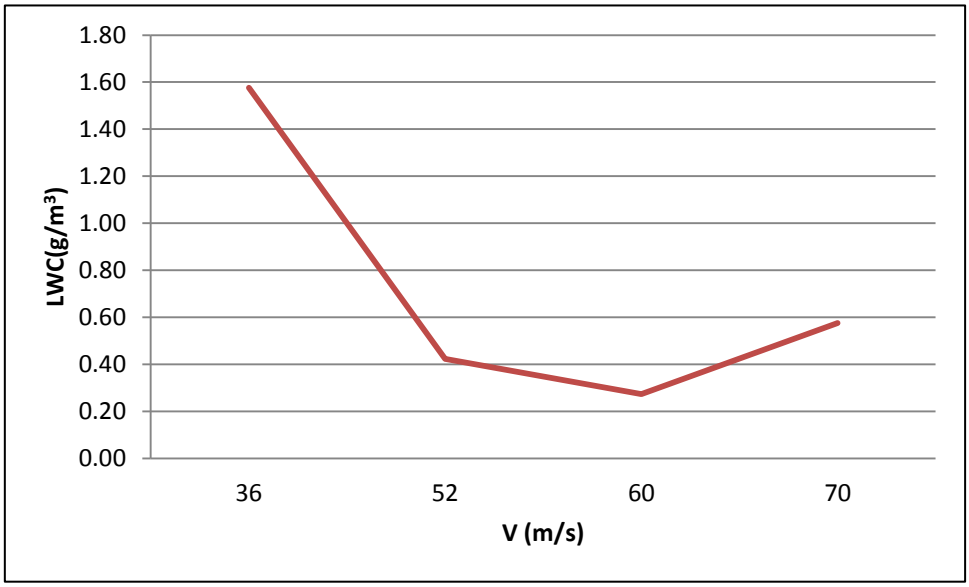

Figure 2-21 Measured local LWC in the centre of the test section vs. air speed

2.4.2 Water Film Formation and Stability

It has been observed that in the SLD conditions, a continuous water film is not always formed over the surfaces and depending on the conditions it could be in form of continues water film, rivulets or only individual beads over the target. We think that the following parameters are the most important in the wetting form over the surfaces:

- The nature of the surface, surface energy and the hydrophobicity of the surface

- The size of the incoming droplets
- Liquid water content
- Impact velocity (normal component)

Figure 2-22 Different wetting conditions for: left) V=35m/s, d=400μm, LWC=0.45gr/m^3, right) V=45m/s, d=400μm, LWC=0.35gr/m^3

We have performed a set of experiments to study different wetting behaviour for a specific surface (polished aluminium with equilibrium contact angle of 43º). We have a control over the droplet size and impact velocity. We can also test different surfaces to study the effect of surface energy on the wetting behaviour of the surfaces. What we need is to control LWC for different conditions to study the effect of this parameter on water film stability.

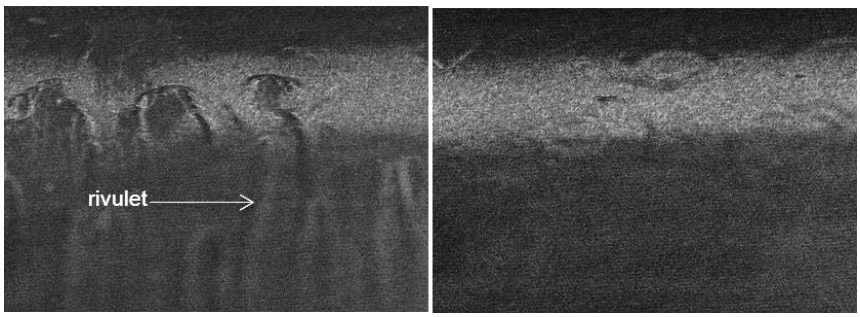

Figure 2-23 Breakup of the continues water film on the target (left) and continues water film (right)

The impact velocity range is between 30 m/s and 80 m/s. the droplets we are using for the experiments are in the size range of 100μm to 500μm. We tried to have control over LWC to achieve the values between 0.3 g/m^3 and 1.6 g/m$^{3.}$. More experiments have been performed in order to observe the impact of the different parameters on the wetting behaviour and water film stability.

Table 2-2 Threshold of continuous water film regime for different conditions

d (μm)	Impact Velocity (m/s)	LWC (gr/m^3)
300	52.50	0.08
300	60.00	0.06
300	71.25	0.07
400	52.25	0.22
400	59.75	0.08
400	70.25	0.40
500	50.25	0.68
500	59.00	0.51
500	70.50	0.92

Table 2-2 Threshold of continuous water film regime for different conditionsTable 2-2 shows the threshold of continues water film regime for different droplet size and impact velocity. For any case, twenty different positions of the droplet generator have been tested to find the threshold of the continuous water film regime. For the droplets smaller than 300 μm we couldn't observe continuous water film even with maximum LWC which was achieved by

pointing the droplet generator in the center. The results can be challenging, as it was widely accepted that in the region with high collection efficiency (such as leading edge of the wing) a continuous water film is formed which is in contradiction with our observation (Fortin, 2004).

2.4.3 Water Film Velocity

In order to use the parametric splash model, first of all we need to find a way to predict the thickness of water film in the different areas of the surface. As there wasn't a direct available method to do so, we undertook a series of the experiments in the icing tunnel to measure the velocity of the water film on the different conditions. In Table 2-3 we summarized the results of the measurement for the water film velocity V_f.

The conditions of the experiments were as follows:

- Air velocity: 50 m/s to 80 m/s
- Droplet size: 300 mm to 500 mm
- LWC: 0.17 g/m^3 to 1.84 g/m^3
- Impact angle: 45^0 and 70^0 (the acute angle between the velocity vector and the surface)

The data provided in Table 2-3 was extracted by processing of more than 16,000 images. The shear stress over the water film was calculated by CFD modelling using FLUENT software. The details of the CFD calculations are given in section 2.3.

Table 2-3 Result of measurement for the water film velocity in different conditions

#	V_{air}(m/s)	Imp. Angle	d(μm)	τ(Pa)	LWC/ρ_w*10^6	V_f(cm/s)
1	54	45	400	0.55	0.42	8.0
2	60	45	400	0.65	0.27	10.2
3	72	45	400	0.8	0.58	11.0
4	81	45	400	1.2	0.20	12.4
5	52	70	300	0.47	0.17	5.5
6	60	70	300	0.59	0.06	5.7
7	70	70	300	0.75	0.03	7.2
8	51	70	400	0.46	0.28	7.0
9	59	70	400	0.58	0.43	6.6
10	70	70	400	0.75	0.31	8.4
11	52	70	500	0.47	1.84	7.5
12	60	70	500	0.59	1.05	8.4
13	70	70	500	0.75	1.34	9.2
14	55	70	400	0.52	0.29	2.6
15	70	70	400	0.75	0.22	4.4
16	80	70	400	0.91	0.20	5.6

2.4.4 Water Film Wavelength and Wave Celerity

Another feature of the water film is the wave celerity. The observations show that there are tangential waves moving with the water film caused by the airflow.

The speed of these waves is measured using an imaging technique. Figure 2-24 shows the transverse waves in the water film and the direction of their propagation. Like any other mechanical wave, the waves moving on the water film could be characterized by their speed and wavelength. The wavelength of the waves is measured by the same imaging technique. The image processing for the thousands of high resolution image have been done manually.

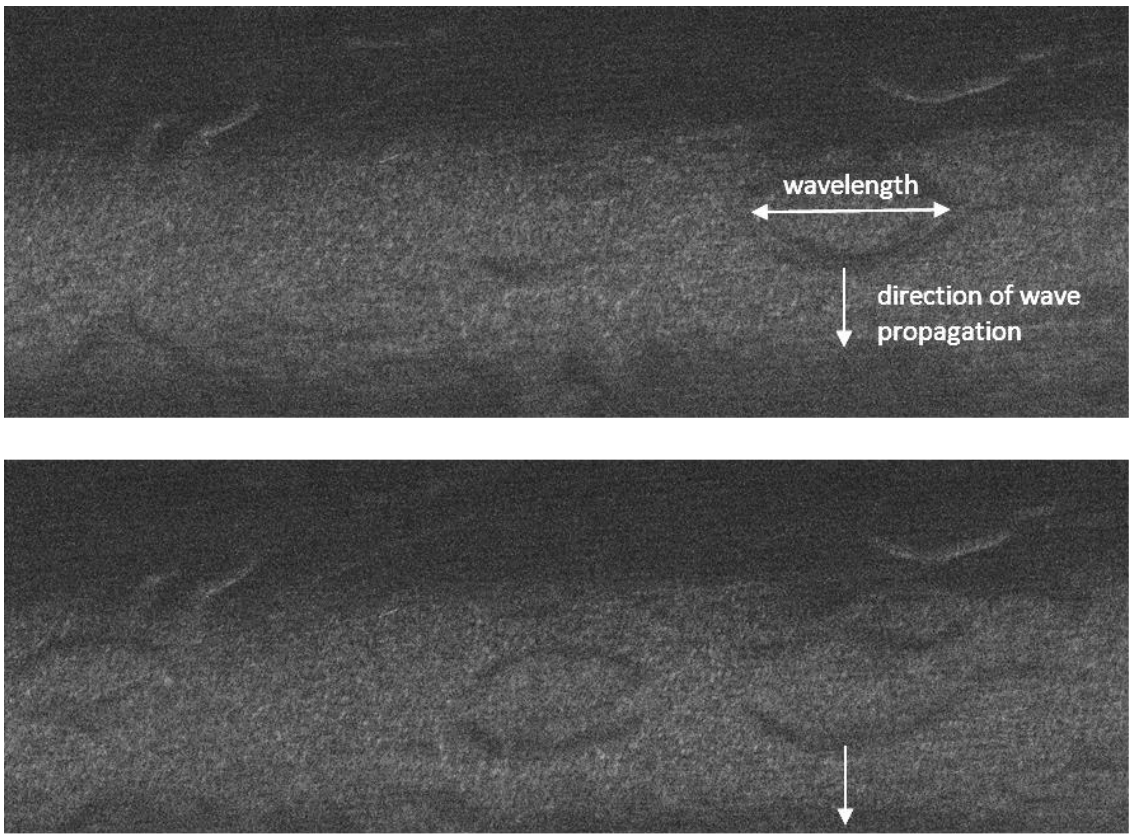

Figure 2-24 Transverse waves in the water film and their propagation direction

These features of the water film could have significant effect on the shape of the ice formation in the glaze regime. The waviness of the water film and the irregularity seen on it will affect the shape of ice feature forming from freezing water film. However, it does not seem practical to include such information in the existing structure of icing codes.

Table 2-4 Measured wavelength and wave celerity of the water film for different conditions

d(μm)	V(m/s)	Wavelength(mm)	Wave celerity (cm/s)
300	53.00	5.70	1.30
300	60.00	6.30	1.50
300	72.00	6.60	1.90
400	51.00	-	-
400	60.00	-	-
400	70.00	6.10	2.90
500	50.50	6.50	1.95
500	59.00	6.40	2.30
500	70.00	6.70	-

2.5 Correlations for Water Film Velocity

Based on the measurements presented in the previous section, we have extracted the following correlations for the water film velocity. The aim was to present the correlations in non-dimensional form to make as general as possible. Although the range of experimental conditions do not cover all the SLD conditions (according to Appendix O), we assume that the proposed correlations could describe the behaviour of the impact and forming of the water film beyond this range of conditions. We might suppose that the physics of high

velocity impact will remains the same outside this range of conditions and it could be modelled using the same correlations.

We define a series of non-dimensional parameters which can describe the physics of the water film formation.

$$Re_f = f(Re_d, w = \frac{LWC}{\rho_w}, Fr)$$

Where

$$Re_f = \frac{\rho_w V_f^2}{\tau} \quad \textbf{(2-7)}$$

$$Re_d = \frac{\rho_w V d}{\mu_w}$$

$$Fr = \frac{V_n^2}{gd \sin \alpha}$$

Where, V_f is the water film velocity, d is the incoming droplet, g is the gravity acceleration and α is the impact angle. In this formulation, LWC is the effective liquid water content, which is the production of overall LWC with local standard catch efficiency. The normal impact corresponds to 90^0. Equation **(2-8)** shows the form of the correlations for the water film velocity, which will be used in the next chapter to estimate the water film thickness.

$$Re_f = 4.84 Re_d^{0.13} w^{0.13} Fr^{-0.29} \quad \textbf{(2-8)}$$

However there is a simpler form of correlation which has acceptable accuracy in order to represent the measurements.

$$Re_f = 1.35 \quad \textbf{(2-9)}$$

This form of correlation has the benefit of not being dependent on the droplet size. It is an important issues in the icing simulation, as in the real cases we have different size of incoming droplets and we do not take that in the account in our experiments and it is assumed that we have only one droplet size in each case. The observations showed that because of unique design of the vertical icing tunnel at Cranfield, it would keep the droplets unbroken and undistorted before entering the airflow field of the target. However, by using Equation **(2-9)** we assume that the water film formation is largely dependent on the airflow field around the surface which seems in agreement with other works and investigation have been made in this subject (Rothmayer, 2002).

2.6 Measurement of Break-up time of Droplet after Splashing

We define the non-dimensional time based on the droplet velocity and size. A series of experiment were undertaken at Cranfield icing tunnel previously (Quero,2006) and we analyzed the available data of splashing in order to estimate the time of break up process.

$$t_{cd}^{*} = \frac{t_{cd}}{d/V_n} \quad \textbf{(2-10)}$$

Figure 2-25 shows the variation of the non-dimensional break up time with the Reynolds and Weber numbers of the droplet. There is no clear trend for this parameter verses Re and We and instead of that it oscillate around an average value. This shows that the break up time is mainly depends on the inertial forces. The average value of the break up time is about 50.

The range of different parameters in the experiments was as follows:

- Number of cases: 94
- $15 < V_{air}(\mathrm{m/s}) < 75$
- $100 < d\ (\mu m) < 500$
- Impact angle: $20^0, 45^0, 70^0$

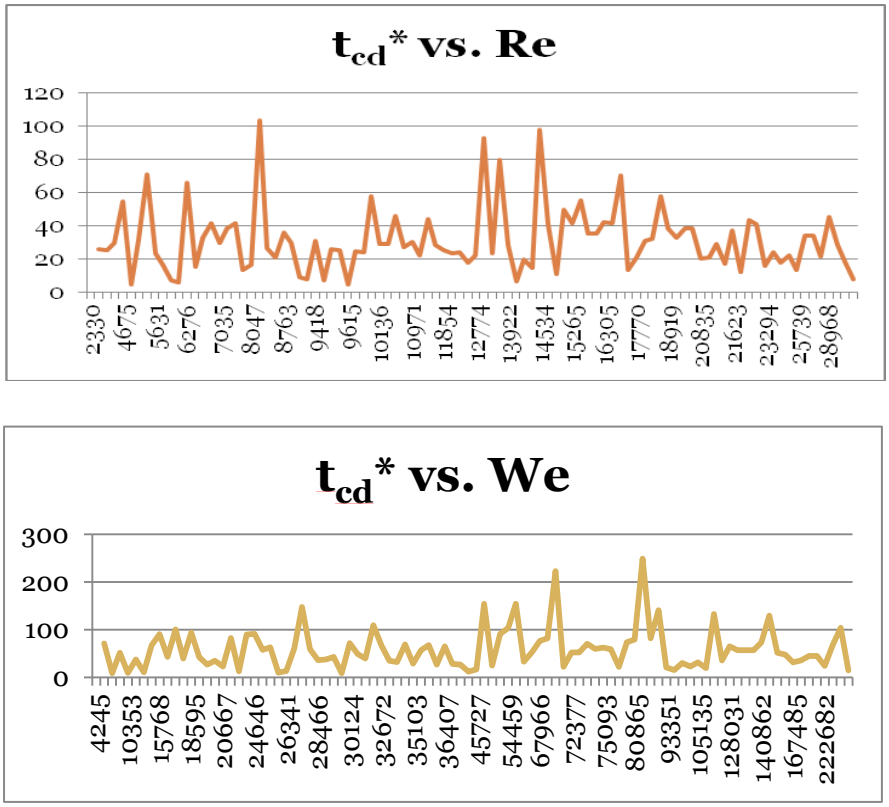

Figure 2-25 Change in non dimensional break up time versus Re and We

The Reynolds number varies from 2,000 to 290,000 and the Weber number range is from 4,000 to 225,000 based on properties of the liquid water.

As a result of the measurements, for this range of We and Re numbers, which are typical range of these parameter in the icing problem, we assume that the non-dimensional breakup time of the droplets on the impact into thin water film is 50. This result of measurement is used as empirical input for the method developed in this work to predict the splashing features and it will be discussed in chapter five.

3 Semi-Empirical Approach to Estimate the Water Film Thickness

3.1 Modelling of Thin Water Film Dynamics

One major factor which drove interest in the water film was the disparity in ice build-up rates in large droplet icing conditions. Ice prediction strategies based on the conversion of all impinging water into ice appeared to be greatly over predicting the volume of ice formed. The areas of uncertainly involved here are sublimation and other loss processes in the ice, the choice of the correct ice density, droplet behaviour immediately before impact (break-up and distortion) and the loss of liquid water from the surface due to splash (and possibly bounce), and due to re-entrainment of water into the flow due to instabilities in the water layer leading to the development of ligaments and free droplets.

The influence of the density value used for an ice prediction is circumscribed by the fact that real ice densities will not exceed the density of pore free ice (approximately 900 Kg/m^3). Lower density values would give larger ice shapes, not smaller.

Droplet behaviour in air flows has been studied by many including some in appropriate parameter ranges for aircraft. A droplet remains essentially spherical whilst the shear forces acting on it are of a similar order or are less than the surface tension forces acting on it. When higher shear forces act, then a combination of time and force can lead to distortion and disintegration. The drag on distorted droplets is a complex matter. Much particle trajectory modelling is based on droplets remaining essentially spherical where as they become elongated and able to rotate as they change shape. Once disintegrated the debris is composed of smaller ligaments and droplets, more able to follow the air flow around the body in question (less icing on an aerofoil, more water flow into a probe or an engine). The influence of droplet distortion and break-up is currently seen as secondary to the modelling of ice in SLD conditions as both analysis and experiments suggests that any significantly non spherical droplet behaviour is restricted to a small volume near enough to the body to not greatly

change the trajectory. It is worth noting however that for certain applications, the parameter space involved may not be covered by the work reported so far.

The coalescence of a water drop into a layer of water has also been the focus of a significant body of work though experiments and analysis in the speed and droplet size range of interest are not so numerous. We anticipate, form experiment and theory that a water layer on an aircraft will be of the order of tens of microns thick, thicker than the diameter of most cloud droplets but thinner than drizzle. The local thickness of any water layer will of course depend on many factors and where impingement is infrequent; the water film is likely to be intermittent, for instance existing as a series of rivulets. What happens when a water droplet strikes will depend on what is happening at that point on the surface.

One method of modelling the impingement problem is to group together the parameters which have the greatest influence on water retention by the surface and creating a semi-empirical descriptor which can be used to factor the catch efficiency to provide the effective water catch. It is even possible to produce a descriptor for the ejected water so that the trajectory it takes may be determined. This is still not an easy task as measuring water retention relies on problematical experiments and analysis. The approach is however appealing to engineering organisations as it can more easily be integrated into existing icing codes without the need to incorporate a model for the water film. For the longer term, it is interesting to speculate as to how we might model ice build-up if we were able to account more fully for the water film.

We have adopted the methodology of Myers and Hammond (1999) to analyse the water film analytically. This approach is based on balancing the force applied on the water film and the velocity distribution inside the water film. The velocity distribution inside the water film can be considered either linear or parabolic. In the linear only the shear force of the air flow considered as the acting force over the water film while in the parabolic distribution we are able to model the tangential acceleration of the flow which in some cases has significant effect on the motion of the water film. This includes the areas with

high pressure gradients and also location where the gravity acts on the tangential direction of the surface. Nevertheless, generally it is believed that the shear force has the most significant effect on driving the thin water film over the surfaces in the typical aircraft icing problems (Rothmayer *et. al*, 2002, Myers *et. al.*, 2004). In the adopted approach the surface tension effect of the water film could be modelled as well.

3.2 Simplified Model of Thin Water Film

We consider a surface exposed to an incoming air flow field and water impingement. In Figure 3-1, s is the tangential direction while n is the normal direction at any position on the body. The incoming air and water droplets have velocity of V which is in x-direction. The gravitational force acting in the direction of y-axis and α is the angle between the surface and x-axis. As was discussed in chapter 2, in some conditions whether a continuous water film will be flowing over the surface depends on the effective velocity (normal component of the air velocity), local LWC and droplet size. In this chapter we only consider the cases which the liquid water forms a continuous water film over the surface.

The dynamics of the thin water film can be modelled mathematically by the incompressible Navier-Stokes equations. The measurements of velocity of the water film, as discussed in chapter 2, are in order of a few centimetres per seconds which is far below (by five orders of magnitude) the speed of sound in the water. This suggests that the water film can be considered as an incompressible flow and also because of the low velocity (and subsequently low Re) the flow is considered as a laminar flow.

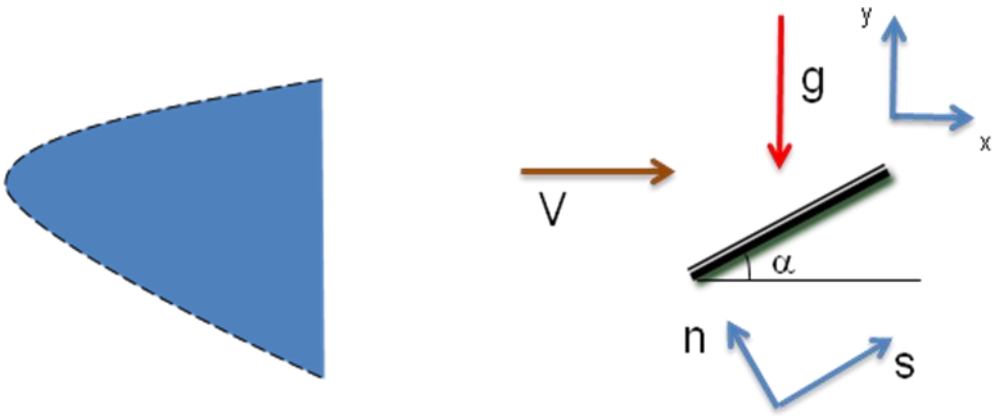

Figure 3-1 Schematic of a surface exposed to water impingement and air flow field and definition of the directions

The two dimensional incompressible Navier-Stokes equations in the steady state conditions for a Newtonian fluid such as water could be written as following (Schlichting, 2000):

$$\rho\left(u\frac{\partial u}{\partial s}+v\frac{\partial u}{\partial n}\right)=-\frac{\partial p}{\partial s}+\rho g_s+\mu\left(\frac{\partial^2 u}{\partial s^2}+\frac{\partial^2 u}{\partial n^2}\right)$$

$$\rho\left(u\frac{\partial v}{\partial s}+v\frac{\partial v}{\partial n}\right)=-\frac{\partial p}{\partial n}+\rho g_n+\mu\left(\frac{\partial^2 v}{\partial s^2}+\frac{\partial^2 v}{\partial n^2}\right) \quad \textbf{(3-1)}$$

Where, u and v are the components of the water film velocity in tangential and normal directions respectively. The gravity acceleration components in tangential and normal direction are g_s and g_n. The molecular viscosity of water is μ, density is ρ and p is the thermodynamic pressure. As the flow is incompressible ρ is assumed as a constant value and pressure will change independent of the density. Although the molecular viscosity is changing with the temperature, in aircraft icing problem the temperature deviation of the water film would be in the narrow range of temperatures above the freezing point of

water and a few degrees of centigrade higher than freezing point. For this reason and as a simplification of the problem the viscosity of the water is assumed constant. It can be noted that Quero (2006) in his experimental work showed that the effect of changes in the water viscosity with temperature has a minor effect on the supercooled droplet impact on the thin water film. It should be noticed that the other effects such the surface tension and free convection (caused by temperature deviation inside the water film) are not considered in this work. For more detailed and more accurate modelling these effects should be considered. The surface tension affects the shape of the interface between the film and air. The free convection effect can cause another mode of motion for the water film when the temperature difference between the solid surface and the air is considerable.

Equation **(3-1)** includes three unknowns ($u, v\ and\ p$) and only two equations. In order to solve this equation another equation is needed which is the mass balance equation in the water film. The mass balance equation for two dimensional steady state incompressible flow is:

$$\frac{\partial u}{\partial s} + \frac{\partial v}{\partial n} = 0 \qquad \textbf{(3-2)}$$

The set of Equations **(3-1)** and **(3-2)** can describe the motion of the water film in the steady state condition. In general this set of equations does not have any analytical solution and in order to solve the velocity field and the pressure, an appropriate numerical method must be used. It means that for a real icing problem, two different sets of Navier-Stokes equations should be modelled numerically, one for the air field simulation and one for much smaller scale for the water film on some parts of the solid surface. However, taking in account the great advancements in numerical simulation in both hardware and software sides, the numerical modelling of the whole problem it is feasible. In this work we are focusing on the analytical modelling of the water film motion as we are

adopting a semi empirical approach to model the water film based on some experimental data.

The assumptions made here to simplify the equation of motion for the water film are based on the observation and experimental data obtained in this work. These data and observations have been discussed in Chapter 2 of this thesis. We have made the following assumptions:

1. The thickness of the water film (h) is in order of 10^{-5} m and is much smaller than the scale of the surface length (L) which in the real problems is in order of 1m.
2. The main direction of the movement for the water film is the longitudinal direction. The normal component of the water film velocity is negligible in the steady state conditions. Also the lateral component of the velocity is negligible in the quasi two dimensional cases.

The water film thickness is the length scale of the water film motion in the normal direction while the surface length scale would be the length scale of the problem in the longitudinal direction. The main air flow is the longitudinal direction. The first assumptions states that ($h \ll L$) and this will lead to ($\frac{\partial}{\partial n} \gg \frac{\partial}{\partial s}$). This means that the changes in the properties, such as the water film velocity, are more significant in the normal direction rather than the longitudinal direction. The normal component of the velocity of the water film is considered zero ($v \approx 0$) based on the second assumption. Notice that mathematical representations of the first and second assumption state that ($\frac{\partial}{\partial n} \gg \frac{\partial}{\partial s}$) and ($u \gg v$) respectively. This in agreement with the mass balance equation **(3-2)** as this equation implies that ($\left|\frac{\partial u}{\partial s}\right| \sim \left|\frac{\partial v}{\partial n}\right|$).

Based on the above assumptions and their mathematical interpretations the set of equation of motion of the thin water film can be simplified and represented as following:

$$0 = -\frac{\partial p}{\partial s} + \rho g_s + \mu \frac{\partial^2 u}{\partial n^2}$$

$$0 = -\frac{\partial p}{\partial n} + \rho g_n \qquad \textbf{(3-3)}$$

The second equation states that there is a pressure gradient inside the water film due to the gravity component in the normal direction. In the stagnation zone this term is negligible as the normal component of the gravity is zero. However, in order to keep the analysis as general as possible this term is kept in at this stage. As was discussed in the previous section the gravitational force and pressure variations have a second order effect on the motion of the thin water film compared with the viscosity forces. The integration over the second equation in **(3-3)** from $n = 0\ to\ n = h$ leads to:

$$p(s,n) = \rho g_n n + C(s) \qquad \textbf{(3-4)}$$

Where $C(s)$ is the constant of the integration and it is only a function of s in general. Assume that $p_\infty(s)$ is the pressure in air just outside the water film obtained from CFD simulations on the clean surface. If we neglect the effect of the surface tension on the contact surface of air and water, we have that:

$$p(s,h) = \rho g_n h + C(s) = p_\infty(s)$$

$$C(s) = p_\infty(s) - \rho g_n h \qquad \textbf{(3-5)}$$

The pressure distribution inside the water film will be as following:

$$p(s,n) = p_{\infty}(s) + \rho g_n (n - h) \quad \textbf{(3-6)}$$

We are modelling the water film motion for any of the segments on the surface as is described in Figure 3-1. In this case we are interested in the variation of the water film thickness in the longitudinal direction as the observations showed that there are no significant changes in the water film thickness when liquid water on the surface is in a continuous water film form. However, when the regime of liquid water on the surface changes from continuous water film to rivulets or beads, there will be a significant change in the water film thickness. In this work, we are focusing on the continuous water film regime and therefore it is safe to assume that the change of the water film thickness is negligible over small segment of the surface. As a result of this assumption, the water film thickness will not have a smooth variation along the surface. This issue will be discussed in more detail in the next section. As a conclusion the variation of the water film pressure in the longitudinal direction is the same as the variation of air pressure (in vicinity of water film) in this direction.

$$\frac{\partial}{\partial s} p(s,n) \approx \frac{\partial}{\partial s} p_{\infty}(s) \quad \textbf{(3-7)}$$

If one combines Equations **(3-7)** and **(3-3)** it will lead to:

$$\mu \frac{\partial^2 u}{\partial n^2} = \frac{\partial p_{\infty}}{\partial s} - \rho g_s = a_s \quad \textbf{(3-8)}$$

The right hand side of **(3-8)** is the acceleration of the flow in the longitudinal direction. We use notation a_s for this term and it is only function of s and does not change in the normal direction. By integrating the Equation **(3-8)** one can have:

$$u(s,n) = \frac{a_s(s)}{2\mu} n^2 + C_1 n + C_2 \quad \textbf{(3-9)}$$

Where C_1 and C_2 are the constants of the integration and can obtained by applying an appropriate set of boundary conditions. The no-slip boundary condition on the surface states that u should vanish on the surface ($n = 0$). This means that ($C_2 = 0$). In general the constant (C_1) can vary in the longitudinal direction but for any segment on the surface, where the variation in s is small, it is constant and does not change in the normal direction. This constant can be obtained from the force balance on the contact surface of the water film and the air flow. We have assumed that the surface tension does not play significant role in the motion of the thin water film and subsequently the normal pressure gradient on the contact surface vanishes. In this case, the main force is the shear force acting on the thin water film. In other words, the shear stress in the water film needs to be balanced with acting shear force from the surrounding air flow field. Similar to the air pressure distribution on the surface, the shear stress of air on the surface is obtained from CFD simulation on the clean surface. For any location on the surface $\tau_w(s)$ is the shear stress of the air acting on that location. The shear stress inside the water film for the same location (it means same s) and at any normal distance from the surface (n) is calculated as:

$$\tau(s,n) = \mu \frac{\partial}{\partial n} u(s,n) \quad \textbf{(3-10)}$$

The force balance on the contact surface ($n = h$) implies that:

$$\tau_w(s) = \tau(s,h) = \mu \frac{\partial u}{\partial n} \; @ \; n = h \quad \textbf{(3-11)}$$

By applying Equation **(3-11)** into Equation **(3-9)** the constant C_1 can be obtained. Notice that in this equation $C_2 = 0$.

$$C_1(\mathrm{s}) = \frac{\tau_w(s)}{\mu} - \frac{h a_s(s)}{\mu} \qquad \textbf{(3-12)}$$

Subsequently the velocity distribution inside the water film is:

$$u(s,n) = \frac{a_s(s)}{2\mu}(n^2 - 2nh) + \frac{\tau_w(s)}{\mu} n \qquad \textbf{(3-13)}$$

At any location on the surface (it means a specific s), the following equations can describe the motion of a thin water film over the surface subject to air flow on it:

$$p(s,n) = p_\infty(s) + \rho g_n (n - h)$$

$$u(s,n) = \frac{a_s(s)}{2\mu}(n^2 - 2nh) + \frac{\tau_w(s)}{\mu} n \qquad \textbf{(3-14)}$$

$$v(s,n) = 0$$

3.3 New Empirical Boundary Condition for the Moving Thin Water Film

In the previous section we have derived a series of equations which can describe the motion of a thin water film subject to gravity, shear force and

pressure gradient caused by the surrounding air flow. The set of Equations **(3-14)** does not predict the thickness of the water film (h) as we need additional information in order to predict the thickness of the water film. The common methodology is to balance the incoming water with the flux of the moving water on the surface. Notice that this mass balance is different from mass balance in Equation **(3-2)** which was the local mass balance for the water film in the different locations on the surface.

We assumed that the flow of the water film is only in the longitudinal direction (s) and the other components of the water film velocity are zero. Therefore the volumetric flux of the water will have only one component in the longitudinal direction and is calculated as:

$$Q_s = \int_0^h u(s,n)dn \qquad \textbf{(3-15)}$$

$$Q_n = 0$$

We have developed an expression for the velocity profile in Equation **(3-14)** and it is used to perform the integration of the Equation **(3-15)**. The volumetric flux in any location of (s) is calculated as:

$$Q_s(s) = -\frac{a_s(s)}{3\mu}h^3 + \frac{\tau_w(s)}{2\mu}h^2 \qquad \textbf{(3-16)}$$

The variation of ($\vec{Q}$) in the longitudinal and normal directions is balanced by the incoming water into the water film and the change of the thickness of the water film. In fact the conservation of mass in any small segment on the surface will lead to the following partial differential equation:

$$\rho_w \frac{\partial h}{\partial t} + \rho_w \nabla . \vec{Q} = J = J_w + J_{evap.} + J_{freez} \quad \textbf{(3-17)}$$

This equation can describe the variation of the thickness of water film moving on the surface and subject to the external forces. The first term on the left hand side of Equation **(3-17)** is the temporal change of the water film thickness while the second term is the net volumetric flux and they are balanced with (J) which is the net of the incoming and outgoing water to and from the water film. The last term describes the following effects:

1. The incoming water from the supercooled droplets. The contribution of the incoming water into (J) can be calculated as:

$$J_w = \beta V_n (LWC) \quad \textbf{(3-18)}$$

   Where, (β) is the collection efficiency, (V_n) is the normal component of the local air velocity (which is assumed to be same as droplet velocity) and (LWC) is the liquid water content of the surrounding air.

2. The amount of water is reduced from the water film by evaporation. This term (J_{evap}) is normally small for unheated surfaces and can be neglected over a small distance.
3. The amount of water is changed to ice during the freezing process. This term (J_{freez}) is calculated as:

$$J_{freez} = -\rho_{ice} \frac{\partial b}{\partial t} \quad \textbf{(3-19)}$$

Where ρ_{ice} is the ice density and b is the thickness of the ice layer formed on the surface. In the case of rime ice, this term is balanced with J_w and all other terms in Equation **(3-17)** vanish as we can assume there is no water layer forming on the surface and all the water will freeze immediately upon impinging

to the surface. In this case the mass balance equation of the water on the surface reads:

$$\beta V_n(LWC) = \rho_{ice}\frac{\partial b}{\partial t} \quad \textbf{(3-20)}$$

Another extreme case is when there is no ice formed on the surface. This could happen when we study the dynamic of the liquid water film in presence of the anti-icing system. In this case we are interested to study the water film and SLD impact to study the effect of the secondary droplets which could re-impinge after the splash to a non-protected area. In this case the mass balance of the liquid water on the surface can be expressed as:

$$\rho_w\frac{\partial h}{\partial t} + \rho_w\nabla.\vec{Q} = \beta V_n(LWC) \quad \textbf{(3-21)}$$

In case of glaze ice the information on the ice layer thickness should be fed into the mass balance equation by balancing the energy on the water film and ice layer. Consider the case when the flux term (Q) is expressed by Equation **(3-16)**. In this case the mass balance equation will be expressed as a differential equation for the water film thickness (h) as:

$$\frac{\partial h}{\partial t} + \frac{\partial}{\partial s}\left(-\frac{a_s(s)}{3\mu}h^3 + \frac{\tau_w(s)}{2\mu}h^2\right) = \beta V_n(LWC)/\rho_w \quad \textbf{(3-22)}$$

This equation is a non-linear parabolic partial differential equation and subject to appropriate boundary conditions and initial condition can predict the evolution of the water film under the assumptions which were discussed in this section.

However, there is no general analytical solution for this equation and a suitable numerical method should be used to solve this equation. This method to predict the water film evolution has been implemented in ICECREMO icing code (Soufflet, 2008).

There are some difficulties associated with numerical solution of Equation **(3-22)**. One of the main difficulties is to define an appropriate set of physical boundary conditions in order to guarantee the well-conditioned behaviour of the equation for different conditions. Another problem in solving this equation occurs when the water film thickness vanishes. It can be shown mathematically that this will lead to numerical instability in solution of water film thickness equation. One way to prevent the numerical instability is to define the "precursor water film thickness" which acts as a limiter on the lower bound of the water film thickness (Myers, *et al.*, 2002).

Although the precursor thickness method provides a stable solution and resolves the evolution of the water film, it does not seem that it is based on the physical observation of the water film formation and development. In other words this type of limiter and boundary conditions can give a well-condition framework to solve the water film equation but it does not necessarily model the development of the water film in the real condition. Another boundary condition used to solve the equation is the assumption of no water film in infinity. It means that as ($s \to \infty$) the water film goes toward zero ($h \to 0$). The reality is that there is a limit on the surface which after that the water does not exist in film form and it starts to break down to other forms specifically rivulets and individual beads. This mechanism is too complicated to be modelled and described by a single differential equation which only characterizes the water film by its thickness.

Figure 3-2 shows an example of a numerical solution of Equation **(3-22)** and water film evolution in time. The peaks in the solution are related to the type of the applied boundary conditions and are seemingly non-physical. What we have seen in the experiments, was a region with continuous water film and a zone where the water film started to break down to other forms of the wetting on the surface.

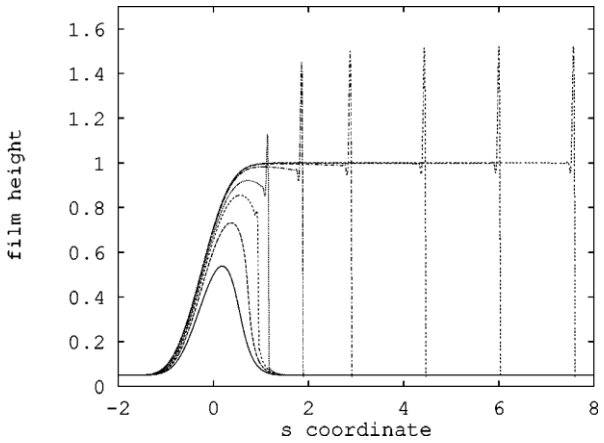

Figure 3-2 Example of numercal solution of water film thickness for film driven by shear force in different times (Myers, *et al.*, 2002)

Other researchers have tried to model the wetting behaviour in the icing problem in different ways. Fortin (2004) and his colleagues defined and modelled three forms of the wetting on the surfaces. The most basic modelling of the water film had been performed by Al-Khalil (1992) where he characterized the water film only by its thickness and related the water film thickness to the air shear force. Despite in depth and sophisticated mathematical modelling of the dynamics of the water film, they have not provided a systematic improvement in the icing simulation. We relate this to lack of models available for individual droplet impact, film formation, stability of the film and its breakup. Further we think that the fine scale interaction between the liquid and the surface has significant effect on the wetting behaviour which in turn affects the ice accretion and roughness development on the surface.

In this work we are interested in modelling the water film in conjunction with the splashing process of the large droplets. We proposed a model for the water film which takes into account the behaviour of the water film in the different conditions. Based on the available experimental data, which have been presented in chapter two, we have developed a new method to estimate the water film thickness. This method uses both analytical and experimental

approaches in order to predict the water film thickness in the different conditions.

In this approach we have extracted a new boundary condition for the water film development process from the experimental data. In chapter two we have presented experimental data of the water film velocity and other features of the water film such as the ripple wavelength and wave speed. We also have presented the condition which we can expect continuous water film in the case of large droplet impact. By implementing the new boundary condition we can estimate the water film thickness using a simple algebraic equation rather than solving the partial differential equation of **(3-22)**.

Let us recall the velocity distribution in the water film which is in the form of Equation **(3-14)**. This equation expresses the velocity of the film in different locations normal to the surface for any longitudinal position on the surface. The parameters in this equation are the water viscosity (considered as a constant) and the external forces acting on the water film. These forces are the shear force, pressure gradient and the gravity. The range of variation of the normal coordinate is between ($n = 0$) and ($n = h$) which are the wall and the tip of the water film respectively. It can be shown that this expression of the velocity is an ascending function of the normal coordinate ($\frac{\partial u}{\partial n} > 0$). If we consider the conventional case of the wing section as it is described in Figure 3-1, it is clear that in the entire impact area, the longitudinal component of velocity (u) is positive. The expression for the velocity gradient in the normal direction is as follows:

$$\frac{\partial u}{\partial n}(s,n) = \frac{a_s(s)}{\mu}(n-h) + \frac{\tau_w(s)}{\mu} \qquad \textbf{(3-23)}$$

As ($u > 0$) and according to Equation **(3-14)** one can find that:

$a_s(n-2h)+\tau_w>0$ therefore

$a_s(n-h)+\tau_w>0$ **(3-24)**

If we compare the last inequality to Equation **(3-23)** it will lead to ($\frac{\partial u}{\partial n}>0$). This shows that the maximum velocity in the water film is the tip velocity. On the other hand we have presented a correlation for the tip velocity of the water film based on the experimental data in chapter two. In the Equation **(3-14)** if we know the acting forces ($\tau_w \; and \; a_s$) and the tip velocity ($u(n=h)$) therefore we can calculate the water film thickness (h). The force terms are calculated using standard CFD simulation which is already a part of any standard icing code as it is described in Figure 1-7. The tip velocity of the water film (V_f) is function of the acting forces on the water film and impact conditions and it is expressed in Equations **(2-7)**,**(2-8)** and **(2-9)**.

Assume that we know the shear force (τ_w) and the acceleration term (a_s) in any longitudinal location of (s) and also the tip velocity of the water film (V_f) is known from icing tunnel experiments. If we substitute the known velocity of (V_f) for ($n=h$) in Equation **(3-14)** we will have:

$$0.5a_s h^2-\tau_w h+\mu V_f=0 \quad \textbf{(3-25)}$$

If we only consider the shear forces as the acting force on the last equation will be simplified to:

$$h=\frac{\mu V_f}{\tau_w} \quad \textbf{(3-26)}$$

It can be shown that Equation **(3-25)** always has real solution for (h). We need to show that:

$$\tau_w^2 > 2\mu a_s V_f \qquad \textbf{(3-27)}$$

If ($a_s \leq 0$) the statement is true as (μ) and (V_f) are both positive real numbers. When ($a_s > 0$) it means that the acceleration term is acting in favour of the shear forces. In other words is similar to case when we are increasing the shear force for the same condition. We recall from Equation **(2-9)** that the water film velocity is characterized mainly by the air shear force, therefore the acceleration term (a_s) does not affect it largely. This means that in case of ($a_s > 0$) the effective shear force is greater than the case of ($a_s = 0$) but the water film is moving at the same speed. The conservation of momentum[2] implies that the water film thickness should be greater in case of ($a_s > 0$) than the case of ($a_s = 0$). The greater the acting forces are the thicker the water film should be in order to maintain the same speed. The water film thickness for case of ($a_s = 0$) is determined using Equation **(3-26)**. As ($h_{a_s>0} > h_{a_s=0}$) one can find easily that:

$$\tau_w > \frac{\mu V_f}{h} \qquad \textbf{(3-28)}$$

As the inequality of **(3-24)** is valid for any (n), we can apply it for ($n = 0$) and this will lead to the following inequality:

$$\tau_w > 2ha_s \qquad \textbf{(3-29)}$$

[2] The total momentum of the water film is proportional to ($V_f . h$). In case of ($a_s > 0$) the momentum is higher and for same V_f the water film is thicker.

By combining the inequalities of **(3-28)** and **(3-29)** one can show that the inequality of **(3-27)** is valid and subsequently the Equation **(3-25)** always has real roots which are the water film thickness. It is obvious that only the positive value root, which satisfies **(3-29)**, is accepted as the water film thickness. The final expression for the water film thickness is:

$$h = [1 - |\mathrm{sign}(a_s)|]\frac{\mu V_f}{\tau_w} + |\mathrm{sign}(a_s)|\frac{\tau_w - \sqrt{\tau_w^2 - 2\mu a_s V_f}}{a_s + \epsilon} \qquad \textbf{(3-30)}$$

Where, ϵ is a small parameter in order of the machine's zero to avoid dividing by zero in case of ($a_s = 0$).

The method as discussed here will be implemented in the deterministic approach to model the splashing process in chapter five of this thesis. The water film thickness is one of the inputs of that model and to predict it in different conditions we will use the semi-empirical method we discussed here.

4 Numerical Modelling of Impact of Large Droplets on Thin Water Film

Numerical modelling and theoretical analysis of impact of droplets on the dry surfaces and into liquid film has been and continues to be of great interest to many researchers. This problem continues to pose a great challenge when modelled numerically as it includes complicated physics, such as surface tension effect and the interaction between the surrounding gas and the liquid phase. Generally the analytical approach in studying the droplet impact is restricted to low speed impact, where there are some analytical solutions for this problem.

The problem of droplet impact into water film is categorized as a multiphase fluid mechanics problem. In terms of numerical modelling there are several approaches to deal with the multiphase problems. The most commonly used approaches are briefly as follows:

- Volume of Fluid (VOF) method, which is suitable for free-surface and stratified flows.
- Mixture method, for modelling bubble and droplet dynamics and granular flows.
- Discrete Phase Model for modelling bubble and droplet dynamics when one phase is extremely dominated.
- The Eulerian approach which is based on advanced particle modelling and kinetic theory of granular flows.

We used a VOF method to model the impact process as we are interested in characterization of the liquid phase after the impact which is a free-surface type problem. The details of the VOF approach are discussed in the next section.

As discussed in chapter one, in SLD icing simulation the most important effects, which are related to the size of the supercooled droplets, are the splashing and re-impingement of the secondary droplets. These effects are related to the impact of the large droplets on either dry surfaces or into water liquid film formed on the surface. The existing icing codes do not model the impact of the

droplets directly as it is extremely time consuming compared to the other computation of the icing codes. It can be showed that for uniform clouds, the frequency of the impact of droplets in any location of the surface is determined as follows:

$$f_{imp} = \frac{V_n}{d}\left(\frac{6\beta LWC}{\pi\rho_w}\right)^{1/3} \quad \textbf{(4-1)}$$

Where, f_{imp} is frequency of impact in (Hz), V_n is the normal component of the local impact velocity, β is the local collection efficiency, d is the droplet size (the mean value) and LWC is the liquid water content in the cloud. For typical SLD icing conditions the frequency of impact is $\sigma(10^4)Hz$ which means that typically around 10,000 drops impact any small segment of the surface at each second. Modelling all of this impact processes requires huge computing efforts and it does not seem practical considering the available computing hardware. However, we can assume that the impact processes for all the events are quite similar and therefore one set of modelling for any condition is sufficient to model the rest of impact events.

In the current work, we adopted a numerical tool in order to model the impact of a large droplet into thin water film. This method has been developed by Purvis (2004) and the results of the simulation have been tested by Quero (2006) and shown promising agreement with the experimental results. We have defined a series of cases, which we believe to be a good representative of a wide range of conditions in SLD icing. We have performed the numerical simulation for these cases in order to extract a model to characterize the splashing process. Here, the main point was to relate the splashing characteristics to the water film thickness. Our observations and previous work of Quero (2006) had shown the effect of water film thickness on the splashing process.

4.1 The Volume of Fluid (VOF) Method

The Volume of Fluid (VOF) is a method used in Computational Fluid Dynamics (CFD) in order to model the multiphase flows, which includes free surfaces in interface (fluid to fluid interface) of the different phases. This method can track and locate these interfaces on a computational mesh which can be either a static or dynamic mesh. Here we constrain the discussion to the static meshes which are used in this work. However, using a dynamic mesh for tracking and locating the interfaces is beneficial as it can reduce the size of required mesh significantly. It is essential to understand that the VOF is not a flow solver; it resolves the location of the free surfaces only. The flow motion equations remain the standard Navier-Stokes equations, in conjunction with the continuity equation, to conserve the total mass of the system. The VOF, similar to many Navier-Stokes solution schemes, is designed to work in a standard Eulerian framework. As we are studying the flow of water in low Mach numbers, it is not necessary to couple the energy equation to the mass and momentum equations. The energy equation can be treated separately to obtain the temperature field in the domain.

The VOF method was developed first by Hirt and Nichols (1981) although that was based on some earlier works and the so-called Marker and Cell (MAC) method. The main advantage of the VOF method over MAC method was in reducing the required memory usage of the modelling (Purvis 2004, Quero 2006). The idea of the VOF method can be described briefly as follows:

- Solving the flow equations using an adequate scheme
- Solving an equation for fraction function for each phase. This parameter defines the volume fraction of each phase in any computational cell.
- Resolution of the free surfaces between different phases using the fraction function.

The equations of motion for the flow of fluids are the momentum conservation and the continuity, which for two dimensional incompressible flows can be expressed as follows:

$$\frac{\partial u}{\partial x}+\frac{\partial v}{\partial y}=0$$

$$\rho\left(\frac{\partial u}{\partial t}+u\frac{\partial u}{\partial x}+v\frac{\partial u}{\partial y}\right)=-\frac{\partial p}{\partial x}+\mu\left(\frac{\partial^2 u}{\partial x^2}+\frac{\partial^2 u}{\partial y^2}\right)+f_x \quad \textbf{(4-2)}$$

$$\rho\left(\frac{\partial v}{\partial t}+u\frac{\partial v}{\partial x}+v\frac{\partial v}{\partial y}\right)=-\frac{\partial p}{\partial y}+\mu\left(\frac{\partial^2 v}{\partial x^2}+\frac{\partial^2 v}{\partial y^2}\right)+f_y$$

Where, t is time,p is pressure, μ is the molecular viscosity, ρ is the density and u and v are the velocity component in x and y directions respectively. The external forces applied to the flow are f_x and f_y in both directions. The external forces may include gravity, surface tension effects, etc. This set of equations is solved numerically with a suitable set of boundary and initial conditions.

The fraction function (φ) is defined on the domain for any phase. For k-th phase (φ_k) shows the fraction of volume is occupied by the k-th phase in any cell. The mathematical behaviour of this scalar function is dominated by the convective nature of the flow and it is described as (Hirt and Nichols, 1981):

$$\frac{\partial \varphi_k}{\partial t}+\frac{\partial (u\varphi_k)}{\partial x}+\frac{\partial (v\varphi_k)}{\partial y}=\Psi_k \quad \textbf{(4-3)}$$

Where Ψ_k is the source term of the k-th phase and includes any exchange between the k-th phase with the other phases in the system. However in many cases this term can be neglected safely if there is no phase change occurring in the system. This is the case in the large droplet impact in the icing problem as we can assume the water does not react with the air and the evaporation can be neglected in a first order modelling. It is clear that the sum of the fraction function for all phases is unity in any computational cell.

$$\sum_{k=1}^{phases}\varphi_k=1 \quad \textbf{(4-4)}$$

4.2 Inviscid Modelling of Large Droplet Impact into Thin Water Film

The problem of single droplet impact can be modelled by considering three different phases of air, droplet and the water film. There are numerical difficulties associated with modelling both air and water flows because of extreme differences between their densities and viscosities (Lee and Lin, 2005; Purvis and Smith, 2004). This problem can cause a serious numerical instability in the solution which becomes more significant at higher velocity regimes. Nevertheless, the airflow has important effects on the liquid phase which cannot be neglected. Here, we decided to use a more reliable numerical model, which does not include the airflow, and to use experimental data to model the effects of airflow on the impact process. The main effect of airflow is in the breakup stage where the velocities are lower compared to the early impact stages.

The set of equations **(4-2)** describes the flow of the fluid and it includes the effects of diffusion and gravity. In typical droplet impact events in the icing problem, the convective forces are the dominated drivers for the flow and the diffusion effect, surface tension and gravity have much lower effect on the dynamics of the flow. To illustrate this lets consider the non-dimensional form of the motion equations as follows:

$$\frac{\partial u}{\partial x}+\frac{\partial v}{\partial y}=0$$

$$\frac{\partial u}{\partial t}+u\frac{\partial u}{\partial x}+v\frac{\partial u}{\partial y}=-\frac{\partial p}{\partial x}+\frac{1}{Re}\left(\frac{\partial^2 u}{\partial x^2}+\frac{\partial^2 u}{\partial y^2}\right)+\frac{1}{We}\frac{\partial \Upsilon}{\partial x} \qquad \textbf{(4-5)}$$

$$\frac{\partial v}{\partial t}+u\frac{\partial v}{\partial x}+v\frac{\partial v}{\partial y}=-\frac{\partial p}{\partial y}+\frac{1}{Re}\left(\frac{\partial^2 v}{\partial x^2}+\frac{\partial^2 v}{\partial y^2}\right)+\frac{1}{We}\frac{\partial \Upsilon}{\partial y}-\frac{1}{Fr}$$

The surface tension effect is modelled as an external force of ($\sigma\nabla\Upsilon$) and (Υ) represents the curvature of the free surfaces Here the velocity is

nondimensionalized by the total velocity of the incoming droplets (V), pressure by (ρV^2), time by (d/V) where (d) is the droplet size. The non-dimensional density is equal to unity and for the incompressible flow is assumed to be constant.

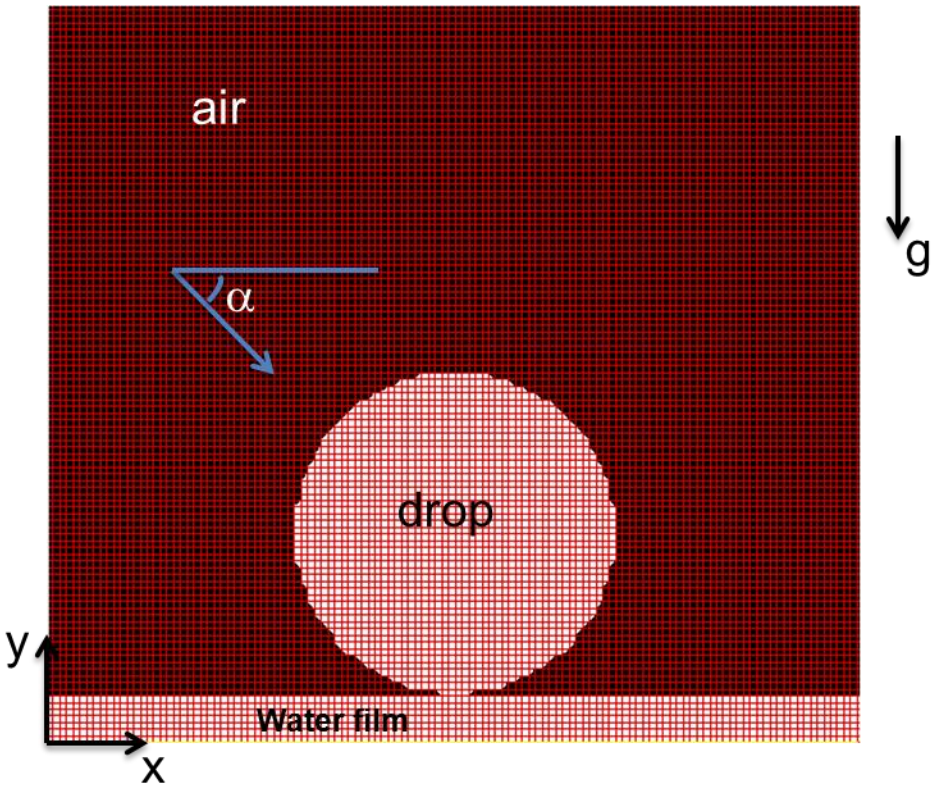

Figure 4-1 Schematic of the droplet impact problem and the mesh used for the numerical simulation

The dimensionless parameters in the set of equations **(4-5)** are:

- The Reynolds number $Re = \rho_{water} V d / \mu_{water}$
- The Weber number $We = \rho_{water} V^2 d / \sigma$
- The Froude number $Fr = V^2 / gd$

Where, σ is the surface tension of water and it is about $0.072\,N/m$ for the standard conditions. For a typical SLD icing problem when $V = 100m/s$ and $d = 100\mu m$:

- $Re = \mathcal{O}(10^4)$
- $We = \mathcal{O}(10^4)$
- $Fr = \mathcal{O}(10^7)$

This clearly suggests that for first order simulation, the effects of the diffusion, surface tension and gravity can be neglected. However for a phenomenon such as breakup, it is necessary to model the surface tension effects as no physical breakup can occur during the modelling if the surface tension term is neglected. Quero (2006) used the VOF flow solver developed by Purvis (2004) and has testified that in the early stages of impact these terms can be safely neglected as they do not have much effect on the simulations. The inviscid flow equations in the non-dimensional form are as follows:

$$\frac{\partial u}{\partial x} + \frac{\partial v}{\partial y} = 0$$

$$\frac{\partial u}{\partial t} + u\frac{\partial u}{\partial x} + v\frac{\partial u}{\partial y} = -\frac{\partial p}{\partial x} \qquad \textbf{(4-6)}$$

$$\frac{\partial u}{\partial t} + u\frac{\partial v}{\partial x} + v\frac{\partial v}{\partial y} = -\frac{\partial p}{\partial y}$$

The droplet is just above the water film in the beginning of the simulation and its velocity initialized according to the impact angle. The total velocity is equal to unity in the nondimensional form.

$$u_{drop} = \cos(\alpha),\ v_{drop} = -\sin(\alpha)$$

$$u_{film} = 0, \qquad v_{film} = 0 \qquad \textbf{(4-7)}$$

It should be noted that the simulations are independent of the actual size of the droplet and the actual thickness of the water film but dependent on the ratio of $(\hat{h} = h/d)$. Also the simulations are independent of the physical velocity of the droplet but they depend on the direction of the impact. This means that the non-dimensional parameters of the simulations are:

- The non-dimensional film thickness $(\hat{h} = h/d)$
- The impact angle (α) as defined in Figure 4-1.

The non-dimensional time of simulation is $(t^* = t_{sim}V_n/d)$, where, d is the droplet size in (μm), V_n is the normal component of the impact velocity in (m/s) and t is the physical time in (μs).

We have tried to use ANSYS Fluent commercial CFD software to simulate the impact of droplet into thin water film. Gattringer (2009) in his work has performed a series of simulations to model the impact of droplet in the water film for low velocities. His work included the effects of airflow on the impact process and also the surface and diffusion effects. We used VOF model and inviscid flow model without taking in account the effect of surface tension. As a limitation of Fluent the air was part of the simulation and this caused numerical instabilities after the impact. It was not possible for us to run the simulations long enough to reach the breakup time which was suggested by our experimental data.

4.3 Study of Accuracy of the Adopted Numerical Model

In a joint project between University College of London and Cranfield University, the accuracy of the VOF model developed by Purvis (2004) has been studied. In that work, the results of numerical simulations of the VOF model have been compared with experimental data of single droplet impact onto thin water film

(Quero, 2006). The corona formed after the splashing was characterized by several features as it is described in Figure 4-2.

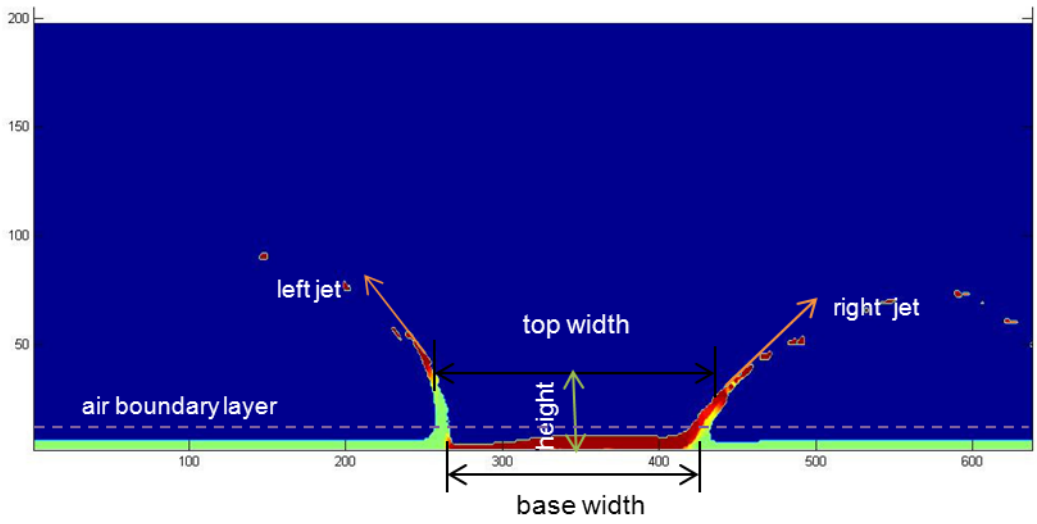

Figure 4-2 Corona features used for splashing charecterization

The outcome of aforementioned work was that in general the results of numerical simulation of the VOF model are in good agreement with the experimental data. Figure 4-3 to Figure 4-10 show different comparisons of the numerical results of Purvis's VOF tool with the available experimental data of Quero's work. In some cases there is a significant difference between the numerical simulations and experimental data. For example, in the case of $h = 50\mu m$ the geometry of corona has not been predicted accurately (Figure 4-9 and Figure 4-10). Not surprisingly for the thicker water film the numerical results are in better agreement with the experiments in terms of predicted values of the different features and also the trend of variation with the droplet size.

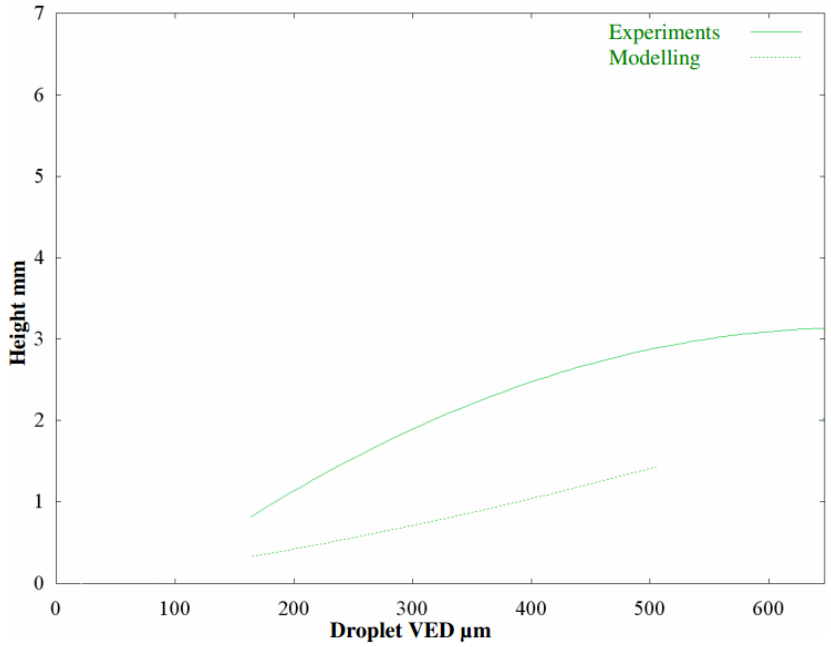

Figure 4-3 Comparison of corona height for impacts into a 150µm water film at 70°impact angle (Quero, 2006)

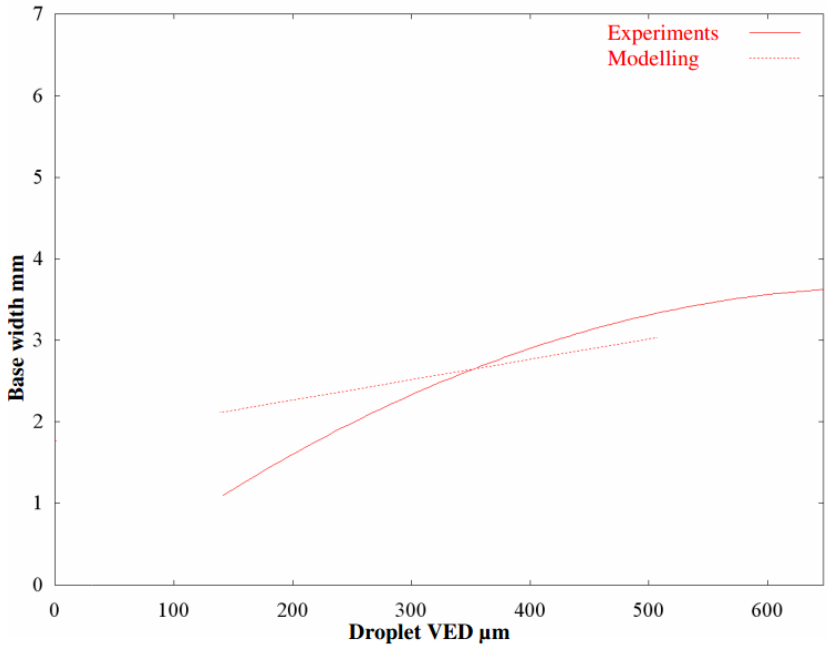

Figure 4-4 Comparison of corona base width for impacts into a 150µm water film at 70° impact angle (Quero, 2006)

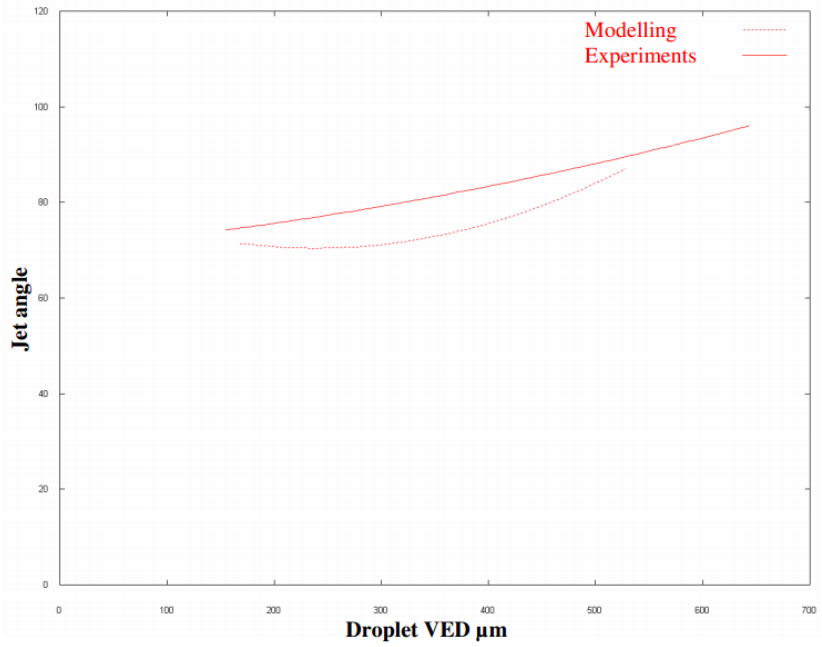

Figure 4-5 Comparison of corona left jet angel for impacts into a 150µm water film at 70° impact angle (Quero, 2006)

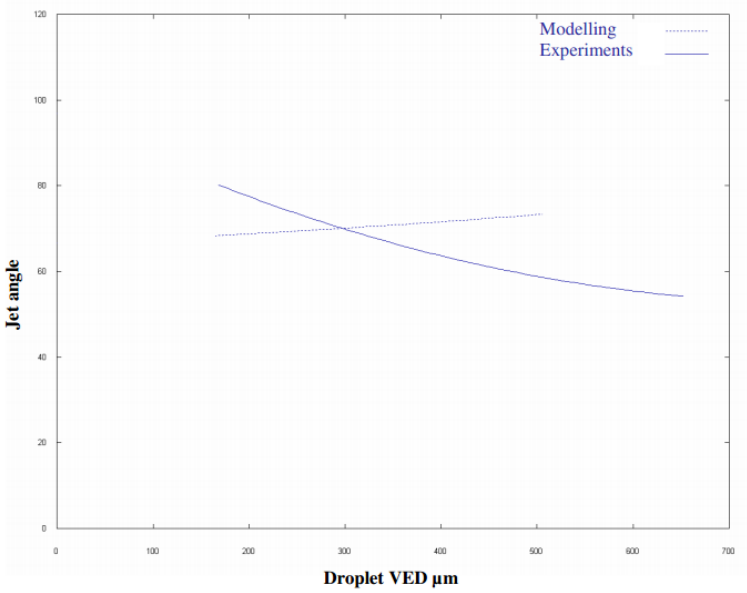

Figure 4-6 Comparison of corona right jet angel for impacts into a 150µm water film at 70° impact angle (Quero, 2006)

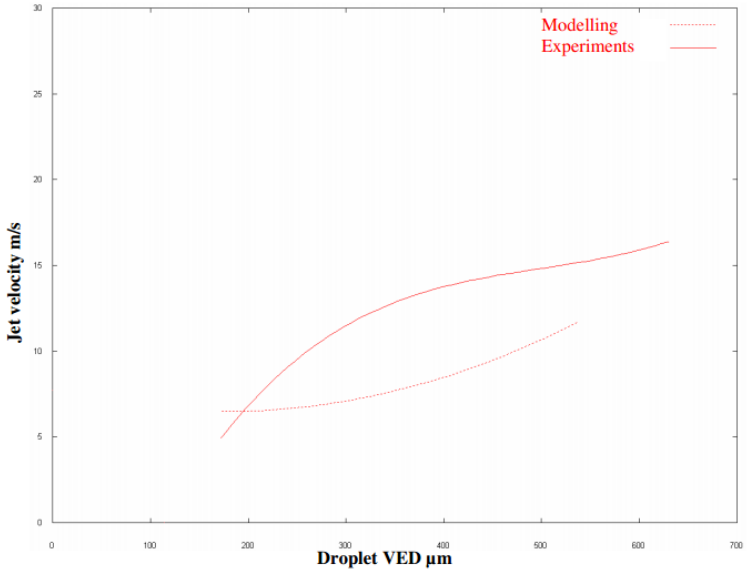

Figure 4-7 Comparison of corona left jet velocity for impacts into a 150µm water film at 70° impact angle (Quero, 2006)

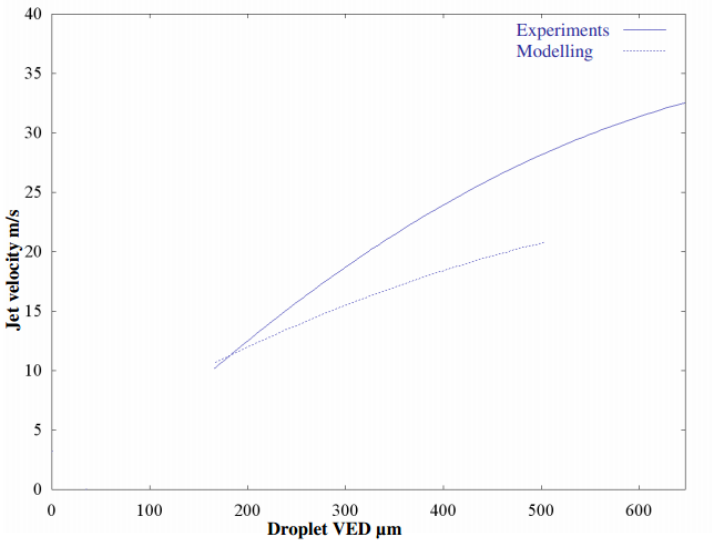

Figure 4-8 Comparison of corona right jet velocity for impacts into a 150µm water film at 70° impact angle (Quero, 2006)

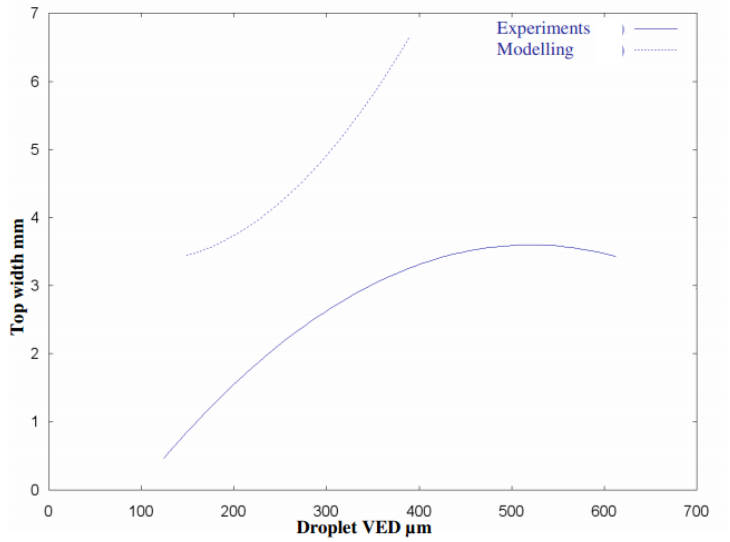

Figure 4-9 Comparison of corona top width for impacts into a 50µm water film at 70° impact angle (Quero, 2006)

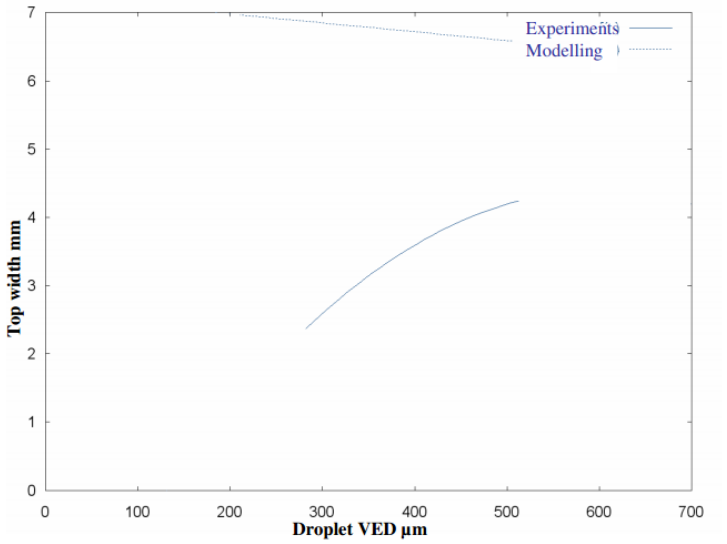

Figure 4-10 Comparison of corona top width for impacts into a 50µm water film at 45° impact angle (Quero, 2006)

4.4 Numerical Results of the Simulations

The input parameters are the film thickness relative to the droplet size ($\hat{h}$) and the impact angle (α). As the solution is inviscid, droplet velocity may be scaled so whilst it is an input, no separate analysis is required to determine its role. The parameter range being analysed covers the range of $\hat{h}$ from 0.1 to 0.5 and α from 20º to 90º, where α the acute angle between the droplet path and the surface as is shown in Figure 4-1.

The output parameters being determined are the velocities of the outgoing jets (speed and angle) and the amount of water splashed beyond a nominal plane within a cut off time. The location of this plane and the choice of the time will come from a consideration of the local air flow. Some further definition of this splashed mass criterion will be undertaken as trends in the results become apparent.

Figure 4-11 shows a sample of the impact simulation for normal impact. The only consideration here is the cut-off time of the simulations, as the modelling does not take in account the effect of the surface tension which is the main role player in the break up process.

We define the non-dimensional time based on the droplet velocity and size. As it was discussed in chapter two, a series of experiments were undertaken at Cranfield icing tunnel previously and we analysed the available data of splashing in order to estimate the time of the break up process. The average value of the break up time of 50 is used here as a cut-off time for the simulations. We also assumed that all the water above a certain plane will be ejected in the air and what is below this plane stays on the water film. The position of this plane is related to thickness of the air boundary layer. For the range of velocity and droplet size in typical SLD icing, we can assume roughly that the air boundary layer thickness is in same order of the droplet size (see Figure 2-13 and Figure 2-14). This will help to keep the simulations in their non-dimensional form without adding any further information on the actual thickness of the air boundary layer.

$$\delta^* = \frac{\delta}{d} = 1 \qquad \textbf{(4-8)}$$

In Equation **(4-8)**, δ^* is the nondimensional air boundary layer thickness which is scaled with the droplet size. In a more realistic case δ depends on the air velocity, which is assumed to be the same as droplet velocity. The CFD calculations of air boundary layer in the icing tunnel are given in chapter two. However, these calculations are for a clean and smooth surface and here we are interested in the air boundary layer over the water film. For these reasons we believe that Equation **(4-8)** can do the job for a first order analysis.

We perform the simulations up to this time or in some cases until we achieve steady features of the splashing. This time could be less than 50 in some cases. We have used up to 1 million cells for the 2D simulations with time steps in order of tenth of micro second.

Figure 4-11 and Figure 4-12 show the captured free surface of the liquid water after the impact for two set of conditions. Using the geometry and velocity of the free surface, we determined the geometrical features of the jets, splashed mass and the corona. Figure 4-13 shows the pressure distribution on the wall after the impact. We have used the pressure distribution in the domain as an indicator for the stability of the simulations. Figure 4-18 shows the pressure instability in some areas as time progresses. The numerical analysis does not have the capability to model the splashing for the dry impacts. In Figure 4-14, the amount of the splashed mass is much lower than the observations of the drop impact. Some examples of the variation of the splashed mass, jet velocity and jet angle which are presented in Figure 4-15 and Figure 4-16.

Table 4-1 and Table 4-2 show the results of the simulations for 20 different cases. The dry impact cases ($\hat{h} = 0$) show poor results and we do not take them into account.

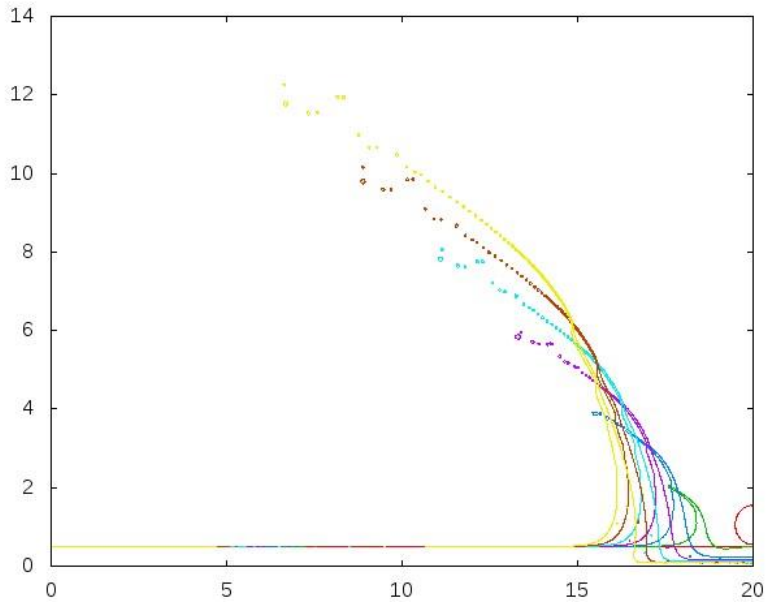

Figure 4-11 the shape of the jets after the impact for $\hat{h} = 0.5$ and $\alpha = 90°$

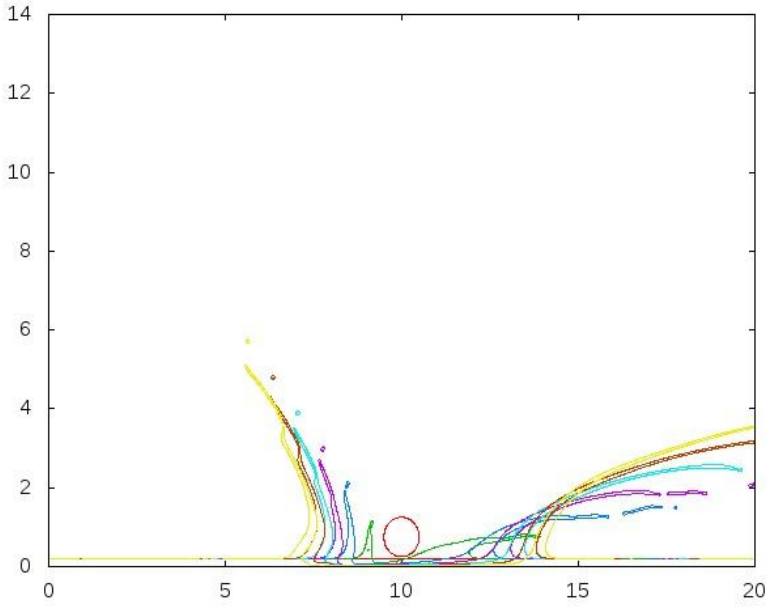

Figure 4-12 the shape of the jets after the impact for $\hat{h} = 0.2$ and $\alpha = 45°$

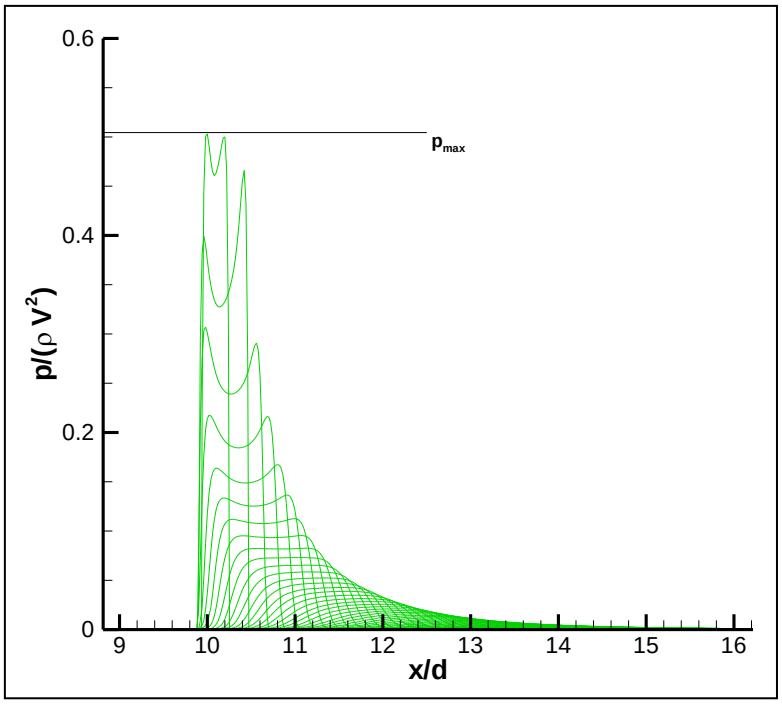

Figure 4-13 Pressure distribution on the wall at different times, 20^0 impact angle on dry surface

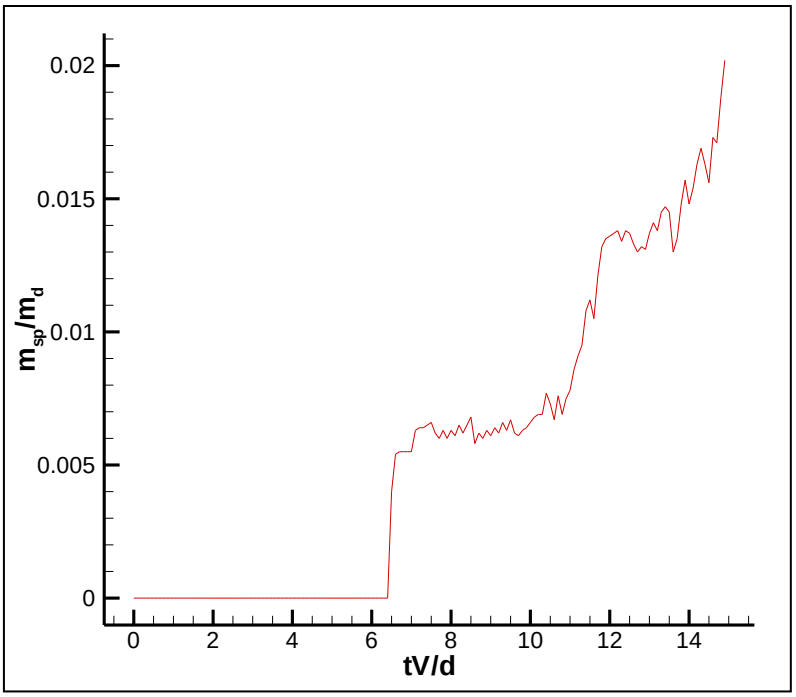

Figure 4-14 Variation of mass splash ratio in time, normal impact on dry surface

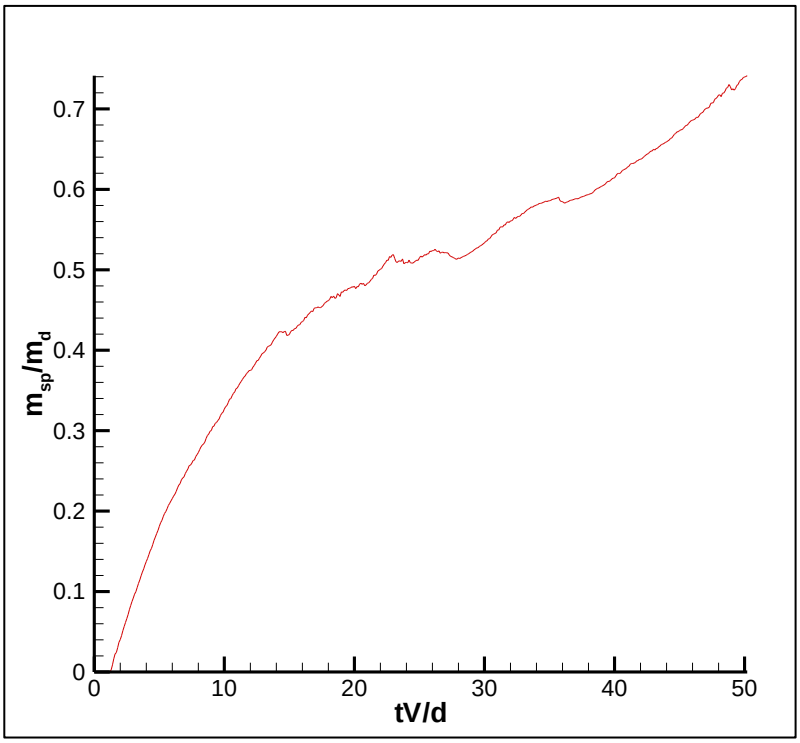

Figure 4-15 Variation of mass splash ratio in time for for $\hat{h} = 0.5$ and $\alpha = 90°$

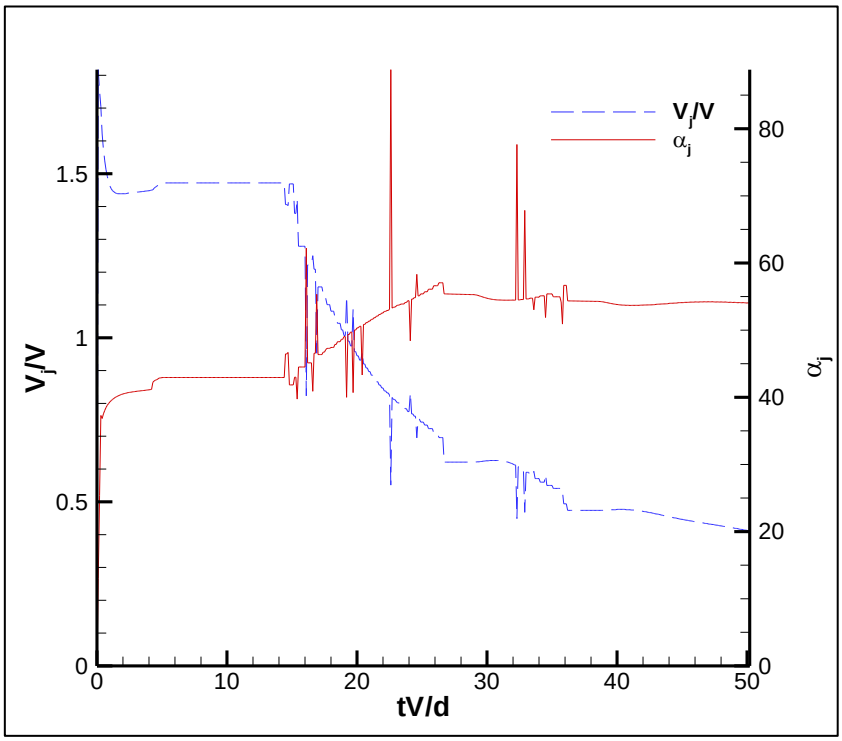

Figure 4-16 Variation of jet velocity and jet angle in time for for $\hat{h} = 0.5$ and $\alpha = 90°$

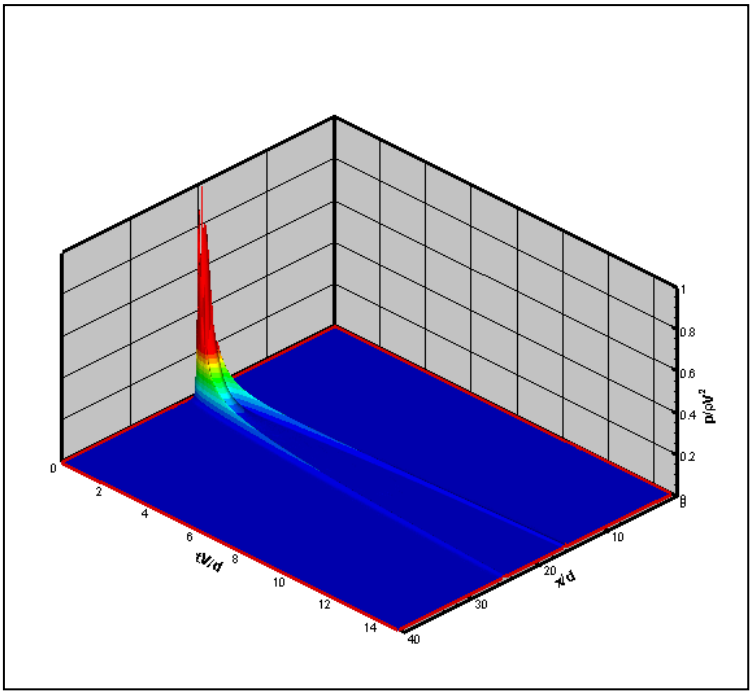

Figure 4-17 Pressure evolution in time for $\hat{h} = 0.2$ and $\alpha = 90°$

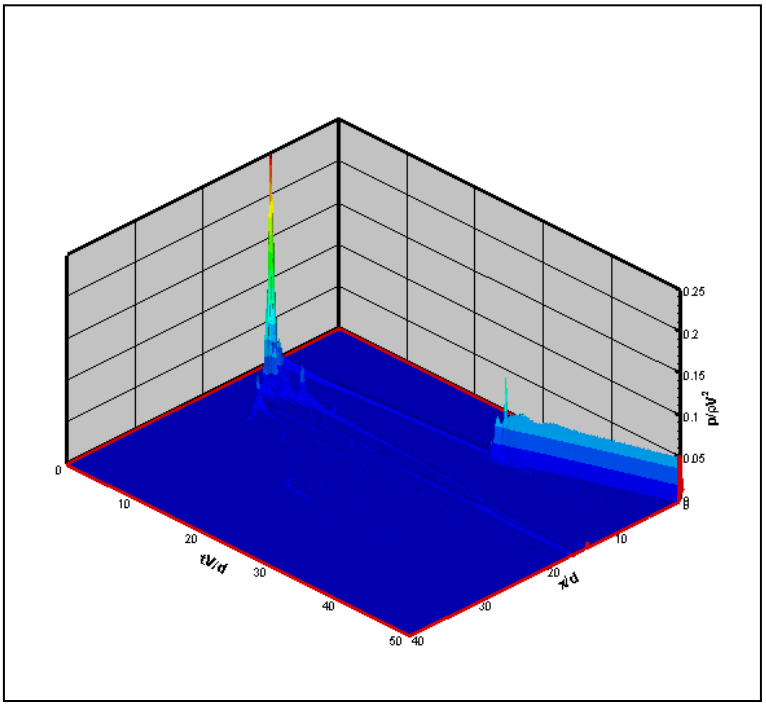

Figure 4-18 Pressure evolution in time for $\hat{h} = 0.3$ and $\alpha = 20°$

Table 4-1 result of simulation on splashed mass after the impact for different conditions

#	$\hat{h}$	α	t*	$m_{sp,total}/m_d$	m_{sp}/m_d
1	0.0	20	50.2	0.06	0.01
2		45	22.8	0.06	0.02
3		70	15.3	0.05	0.03
4		90	14.9	0.24	0.03
5	0.2	20	29.2	5.96	1.06
6		45	19.9	2.80	0.68
7		70	16.1	2.44	0.58
8		90	14.7	2.36	0.64
9	0.3	20	50.2	6.22	0.68
10		45	31.5	4.55	0.54
11		70	15.3	2.96	0.51
12		90	50.2	5.99	0.82
13	0.4	20	50.2	6.66	0.39
14		45	25.8	4.61	0.52
15		70	18.0	3.87	0.49
16		90	50.2	7.28	0.84
17	0.5	20	40.2	6.52	0.46
18		45	23.7	4.67	0.47
19		70	18.6	4.60	0.47
20		90	50.2	8.05	0.84

Table 4-2 result of simulation on ejected jets after the impact for different conditions

#	$\hat{h}$	α	t*	$V_{j,L}/V_d$	$\alpha_{j,L}$	$V_{j,R}/V_d$	$\alpha_{j,R}$
1	0.0	20	50.2	0.278	90	0.649	88
2		45	22.8	0.799	90	0.970	90
3		70	15.3	1.137	90	0.603	89
4		90	14.9	1.651	90	1.651	90
5	0.2	20	29.2	2.201	75	0.886	35
6		45	19.9	0.568	52	0.419	90
7		70	16.1	0.378	90	2.097	26
8		90	14.7	1.673	38	1.673	38
9	0.3	20	50.2	0.325	87	0.450	43
10		45	31.5	0.521	56	0.569	89
11		70	15.3	1.207	90	2.242	31
12		90	50.2	0.444	49	0.444	49
13	0.4	20	50.2	0.322	64	0.423	47
14		45	25.8	0.465	58	1.306	48
15		70	18.0	1.130	90	1.314	40
16		90	50.2	0.412	51	0.412	51
17	0.5	20	40.2	0.367	68	0.546	39
18		45	23.7	0.427	60	1.586	26
19		70	18.6	0.951	90	1.214	41
20		90	50.2	0.411	54	0.411	54

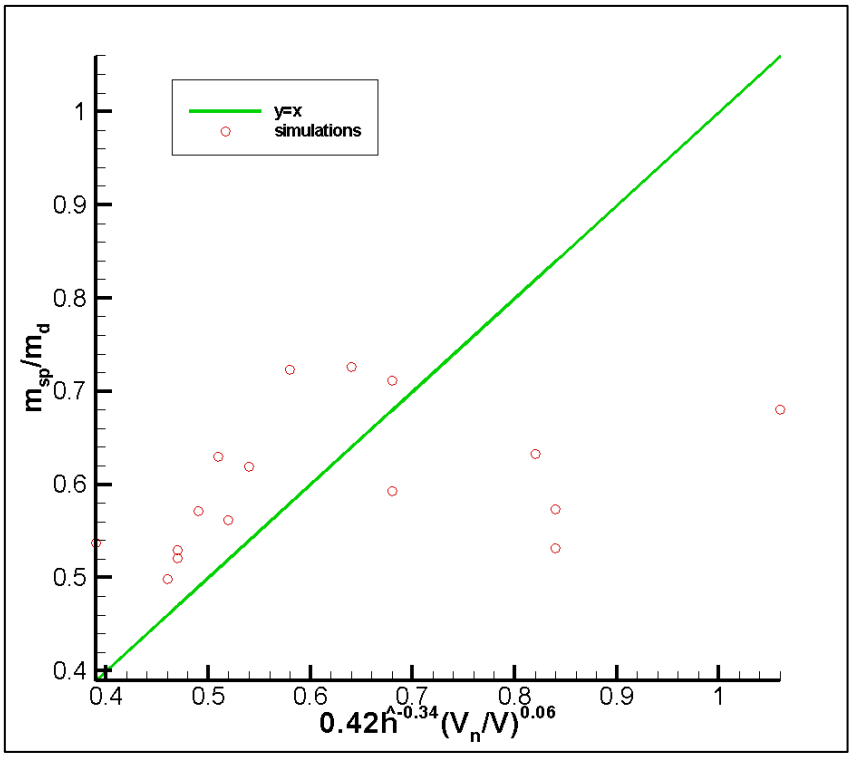

Figure 4-19 Splashed mass ratio for different water film thickness ratios and impact angles

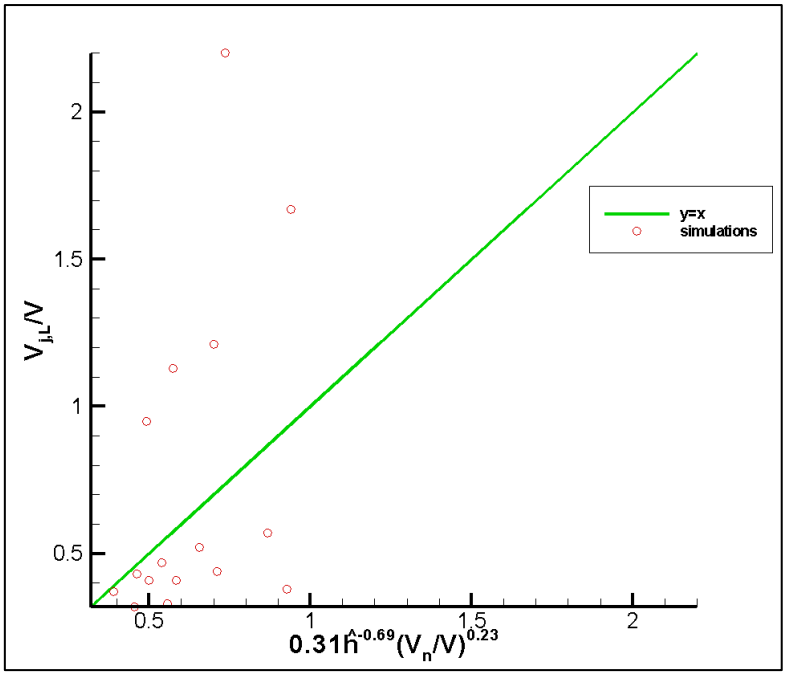

Figure 4-20 Left jet total velocity ratio for different water film thickness ratios and impact angles

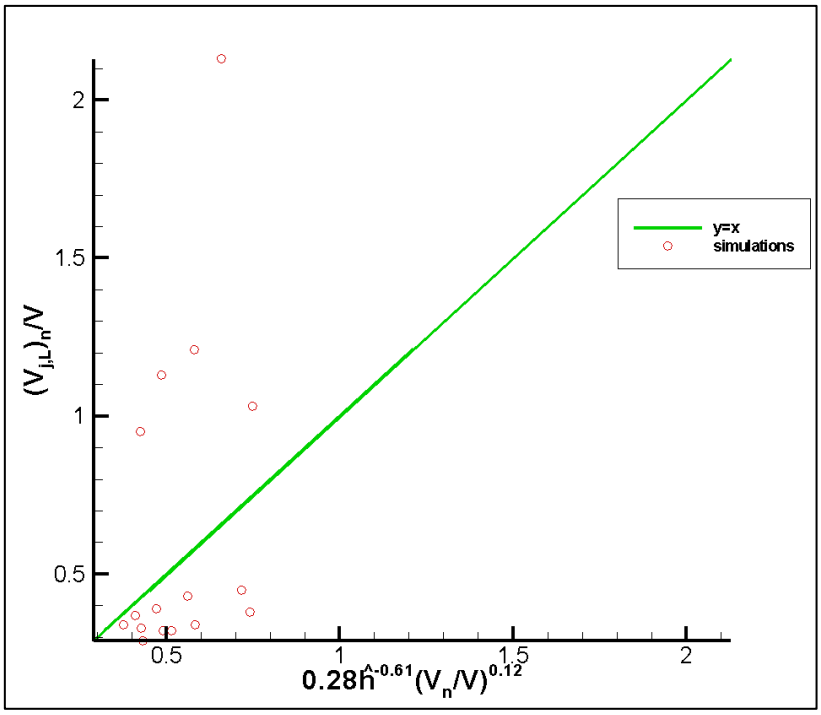

Figure 4-21 Left jet normal velocity ratio for different water film thickness ratios and impact angles

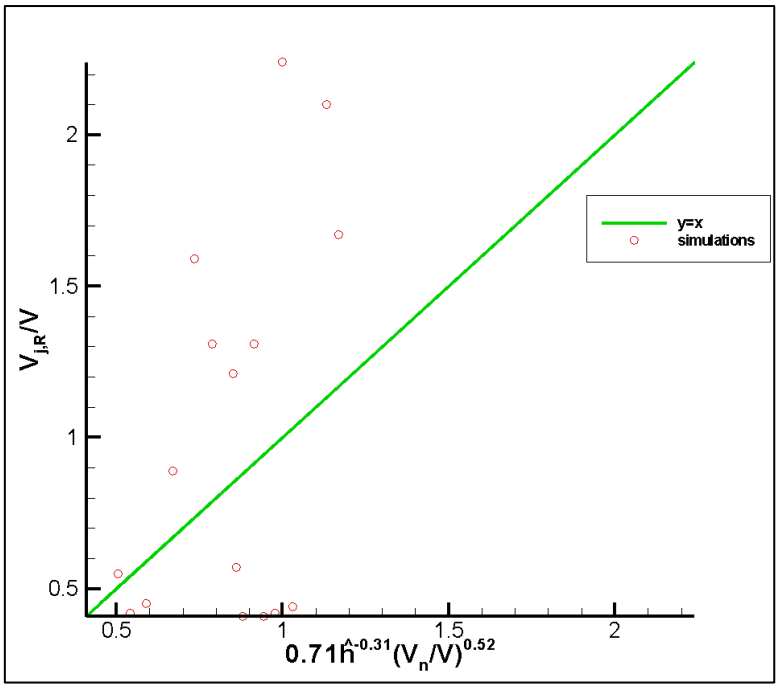

Figure 4-22 Right jet total velocity ratio for different water film thickness ratios and impact angles

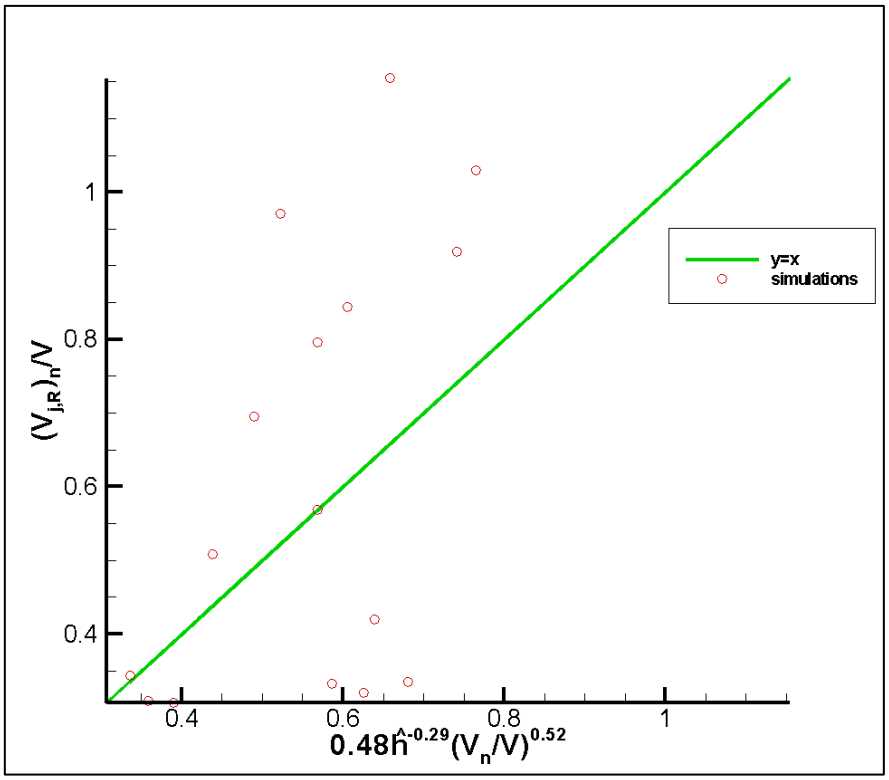

Figure 4-23 Right jet normal velocity ratio for different water film thickness ratios and impact angles

Figure 4-19 shows the plot of the result of the splashed mass as a function of the water film thickness ratio ($\hat{h}$) and the impact angle which is represented by (V_n/V). We have used a logarithmic linear regression to extract a correlation for variation of (m_{sp}/m_d) versus ($\hat{h}$) and (V_n/V). The same method has been used to extract the correlations for the jet parameters. The results of the simulations have been plotted in Figure 4-20, Figure 4-21, Figure 4-22and Figure 4-23.

Final Correlations

Based on data in Table 4-1 and Table 4-2, we have extracted the following correlations which can model the splashing process based on the made assumptions.

$$\frac{V_{j,L}}{V_d} = 0.31\hat{h}^{-0.69}\left(\frac{V_n}{V_d}\right)^{0.23}$$

$$\frac{(V_{j,L})_n}{V_d} = 0.28\hat{h}^{-0.61}\left(\frac{V_n}{V_d}\right)^{0.12} \quad \textbf{(4-9)}$$

$$\frac{V_{j,R}}{V_d} = 0.71\hat{h}^{-0.31}\left(\frac{V_n}{V_d}\right)^{0.52}$$

$$\frac{(V_{j,R})_n}{V_d} = 0.48\hat{h}^{-0.29}\left(\frac{V_n}{V_d}\right)^{0.52} \quad \textbf{(4-10)}$$

$$\frac{m_{sp}}{m_d} = 0.42\hat{h}^{-0.34}\left(\frac{V_n}{V_d}\right)^{0.06} \quad \textbf{(4-11)}$$

$\hat{h}$ is the ratio of water film thickness over the droplet size

V_n is the normal component of the incoming droplet velocity

V_d is the incoming droplet velocity

$V_{j,L}$ is the velocity of left jet (the incoming droplet is coming from left)

$V_{j,R}$ is the velocity of right jet

$(V_{j,L})_n$ is the normal component of velocity of left jet

$(V_{j,R})_n$ is the normal component of velocity of right jet

m_{sp} is the splashed mass

m_d the mass of incoming droplet

5 Deterministic Approach to Characterize the Splashing in Icing Problem

In this model, we have combined both experimental and observation data with numerical modelling of the splashing process. The experimental work has been undertaken at Cranfield University Icing facilities and has been discussed in chapter two of this thesis. The numerical modelling has been tested and proven to have good agreement with the experimental data, and the results of the numerical modelling are presented in chapter four (Quero *et al.*, 2006). The key points and related results from the aforementioned work are as follows:

- Good agreement between the proposed numerical modelling and the experimental data
- The effect of the water film thickness on the splashing features in the SLD conditions
- Minor effect of temperature on the splashing

These findings led us to undertake a series of experiments to explore the water film thickness for the different conditions. Furthermore, they suggested that a reliable numerical model can be used to predict the splashing features. The numerical model is based on the relative water film size (the ratio of water film thickness to droplet size) and the impact angle of the incoming droplet. This model considers water flow as an inviscid flow with a moving interface between the two different phases of the droplet and the water film. The multiphase modelling is treated using VOF (Volume of Fluid) method.

In order to model the icing process explicitly, forces, heat and mass transfer must be dealt with, surfaces tracked and states determined, over length scales ranging possibly form tens of metres, in principle down to tens of microns and with time scales of many tens of minutes but with resolutions of a few hundreds of nanoseconds. As this seems currently impractical, the option of smaller analytical steps is explored here. A general flow diagram for a water film and splash model is set in Figure 5-1.

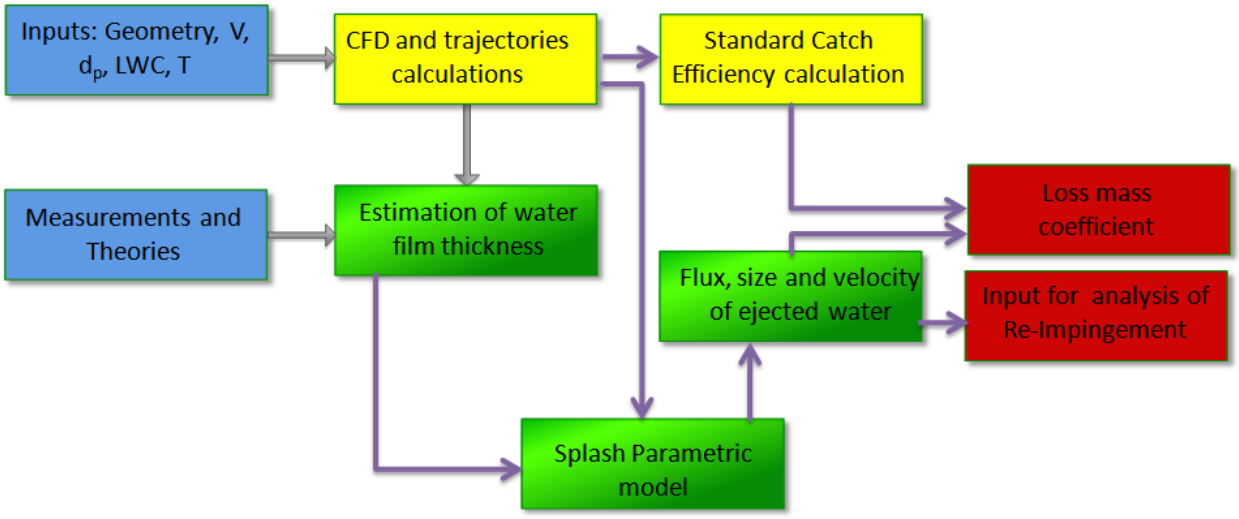

Figure 5-1 the proposed methodology to model the splashing in SLD conditions

In the icing modelling strategy described in Figure 5-1, the usual elements in an icing code, the definition of inputs, the CFD analysis and the standard catch efficiency calculation are included as basic modules to minimise changes needed in methodology. In addition to these steps, the output of the CFD is used, together with the input conditions, to determine local water film thickness. This was explained in detail in chapter three. The parametric splash model is a new element which embodies an array of analysis results for models of water droplets of a range of sizes striking water layers of a range of thicknesses over a range of angles and speeds. This element produces parameters relating to the velocity, scale and mass of splashed water based on short time fine scale inviscid modelling of droplet impact. The output from this element may be used directly, or as in the case of the illustration, used to compute a loss mass coefficient to factor into a conventional icing simulation.

The different elements of the proposed methodology are discussed in this chapter. In the end, the proposed model is compared with some of available model for SLD modelling. Also the limitation of the model and its applicability are discussed. Although the final assessment of the model depends on the

results of the ice shape prediction in an icing code, this is outside the scope of the current work.

5.1 CFD and Catch Efficiency Calculations

The catch efficiency or collection efficiency, which is usually shown by β is a parameter to determine the local water liquid content on the surface. Consider a cloud with liquid water content of (LWC). The aerodynamic field around the surface affects the path of the travelling droplets and diverts them from the free stream path. Thus the local water concentration, which would impact the surface at each location on the surface, is not always the liquid water content in the free stream but the effective water concentration which is $(LWC)_{eff} = \beta(LWC)$. In the icing simulation process, the catch efficiency is calculated using the CFD calculations of the airflow field. Some detail of the CFD modelling was discussed in chapter two.

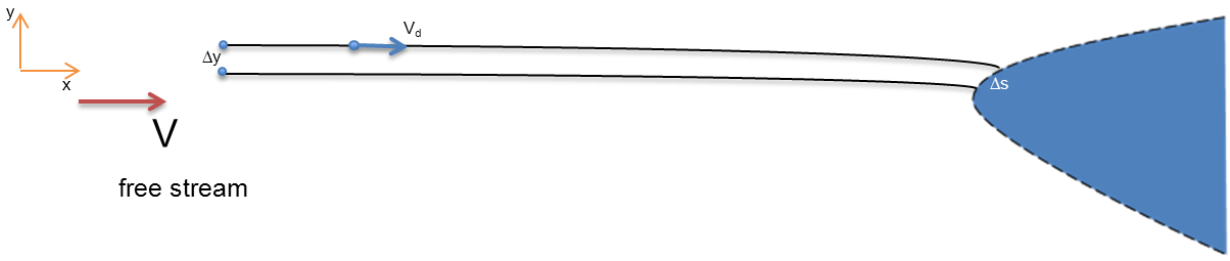

Figure 5-2 the schematic of the droplets trajectories in a typical aircraft icing problem

The catch efficiency determines the ratio of impinging droplets mass flux on the surface, to the mass flux that would occur on the surface if droplets were not deflected by the air and is calculated as:

$$\beta = \frac{\Delta y}{\Delta s} \qquad \textbf{(5-1)}$$

The illustration of terms Δy and Δs is given in Figure 5-2. For any pair of droplet in the upstream with a known spacing of (Δy) the impingement area (Δs) is determined by calculating the trajectories of the droplets. The initial location of the droplets must be far enough from the body to not be affected by the body. Typically this distance is about five times the scale of the body. As it was discussed in chapter one, the Lagrangian approach is more suitable for the SLD icing regime. In this approach force balance is made for each individual droplet and this helps to model the droplet impact. In most cases (two dimensional simulations) it is sufficient to consider about 50 droplets in order to determine the catch efficiencies. The initial velocity of the droplets is usually taken equal to the flight speed (Wright, 2002).

The most significant force acting on the droplets is the drag force caused by the relative velocity between the droplet and the airflow. The equation of the motion for the droplets can be expressed as follows (Figure 5-2):

$$\ddot{x}_d = -\frac{D}{m_d}\cos\gamma + g\sin\gamma$$

$$\ddot{y}_d = -\frac{D}{m_d}\sin\gamma - g\cos\gamma$$

$$\gamma = \tan^{-1}\left(\frac{\dot{y}_d}{\dot{x}_d - V}\right) \qquad \textbf{(5-2)}$$

$$\frac{D}{m_d} = \frac{3}{4}\frac{c_d V_{rel}^2}{d}$$

$$V_{rel} = \sqrt{(\dot{x}_d - V)^2 + (\dot{y}_d)^2}$$

$$V_d = \sqrt{(\dot{x}_d)^2 + (\dot{y}_d)^2}$$

Where, (x, y) is the position vector of the droplet, $(\dot{x}, \dot{y})$ is the velocity vector and $(\ddot{x}, \ddot{y})$ is the acceleration vector of the droplet. If the droplet reaches the

terminal velocity, its velocity will remain constant prior to the impact. The terminal velocity of the water droplet of the air can be estimated as suggested by Wright (2002):

$$V_{terminal} = \sqrt{\frac{4g(\rho_w - \rho_{air})}{3c_d d\rho_{air}}} \qquad \textbf{(5-3)}$$

Many different expressions have been introduced and have been implemented for the drag coefficient of the droplet (c_d). They are generally based on the theoretical modelling of the drag coefficient for the solid spheres. Some models take into account the distortion of the droplets when it is subjected to strong aerodynamic fields. However as it was discussed in the first chapter, the effects of the distortion and the breakup are second order effects for the SLD regime. A comprehensive study has been performed by Luxford (2005) on the drag coefficient, distortion and breakup of the SLD's. One set of the correlations for the SLD drag coefficient is the model introduced by Clift and his colleagues (Clift et al., 1987) which takes into account the effect of the distortion.

$$c_d = (1 - \tilde{e})c_d^{sphere} + \tilde{e}c_d^{disk}$$

$$c_d^{sphere} = \frac{24}{Re} + 0.3 + \frac{6}{1 + \sqrt{Re}} \qquad Re > 1000$$

$$c_d^{sphere} = \frac{24}{Re} + 0.4 + \frac{6}{1 + \sqrt{Re}} \qquad Re \leq 1000 \qquad \textbf{(5-4)}$$

$$c_d^{disk} = 1.540 \qquad Re > 1000$$

$$c_d^{disk} = \frac{87.168}{Re}\left(1 + \frac{Re^{2/3}}{6}\right) \qquad Re \leq 1000$$

$$\tilde{e} = 1 - \frac{1}{(1 + 0.007\sqrt{We})^6}$$

Where, $\tilde{e}$ is the distortion factor and We is the Weber number based on air density and the relative velocity of the droplet and the airflow. For the low We numbers, the distortion factor is close to zero and not surprisingly the drag coefficient obeys the drag law for a sphere. On the other hand when We number is large, which is the case in most aircraft icing condition, this model takes in account the effect of the distortion.

In reality the clouds do not consist of only one droplet size but a range of different droplet sizes. Also in the icing test facility the cloud has a range of the droplet sizes with large variation. Figure 5-3 shows one example of cloud in the icing test facility. In this case the size of the droplets varies from $30\mu m$ to $500\mu m$ and the MVD is around $215\mu m$.

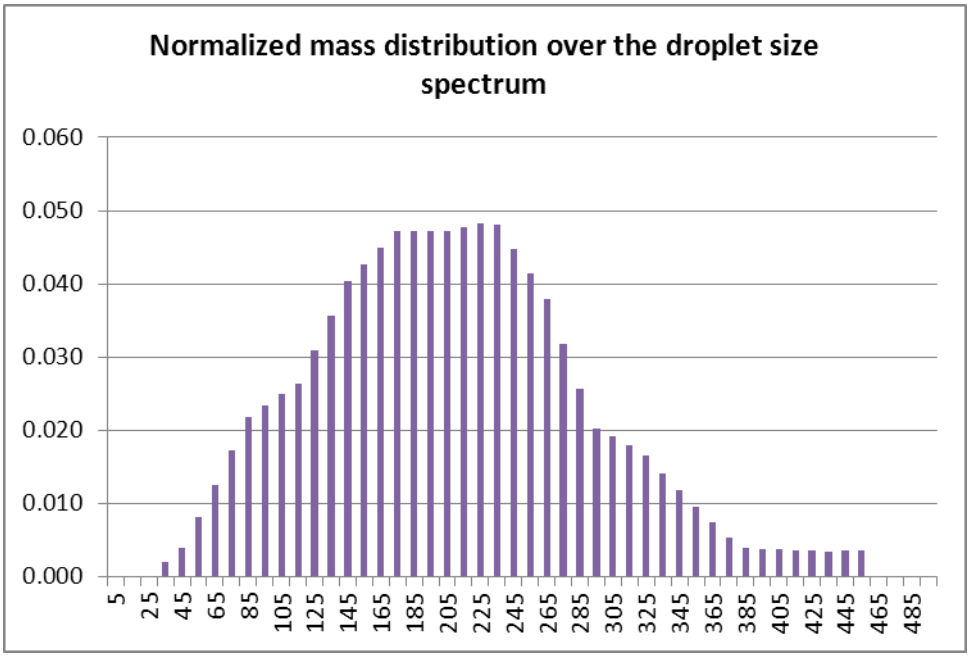

Figure 5-3 the mass distribution of different droplet size on NACA0012 airfoil at M=0.2 for MVD=215μm. [EXTICE icing test campaign DGA, France 2010]

To determine the catch efficiency in such cases, the calculations should be repeated for any droplet size. The resultant catch efficiency will be the weighted

summation of the catch efficiencies for any droplet size. However, in practice only about ten representative droplet sizes is considered for the calculations.

$$\beta_0 = \sum_{bins} \beta_r p_r \qquad \textbf{(5-5)}$$

In this equation, β_0 is the resultant catch efficiency, β_r and p_r are the catch efficiency and weight factor of the *r-th* bin.

The catch efficiency can be measured in the icing facility by accreting the ice in very low temperatures (rime regime ice). In this condition we can assume that all of incoming water freezes immediately and even for SLD condition it can be assumed that splashing process does not have significant effect on the ice accretion.

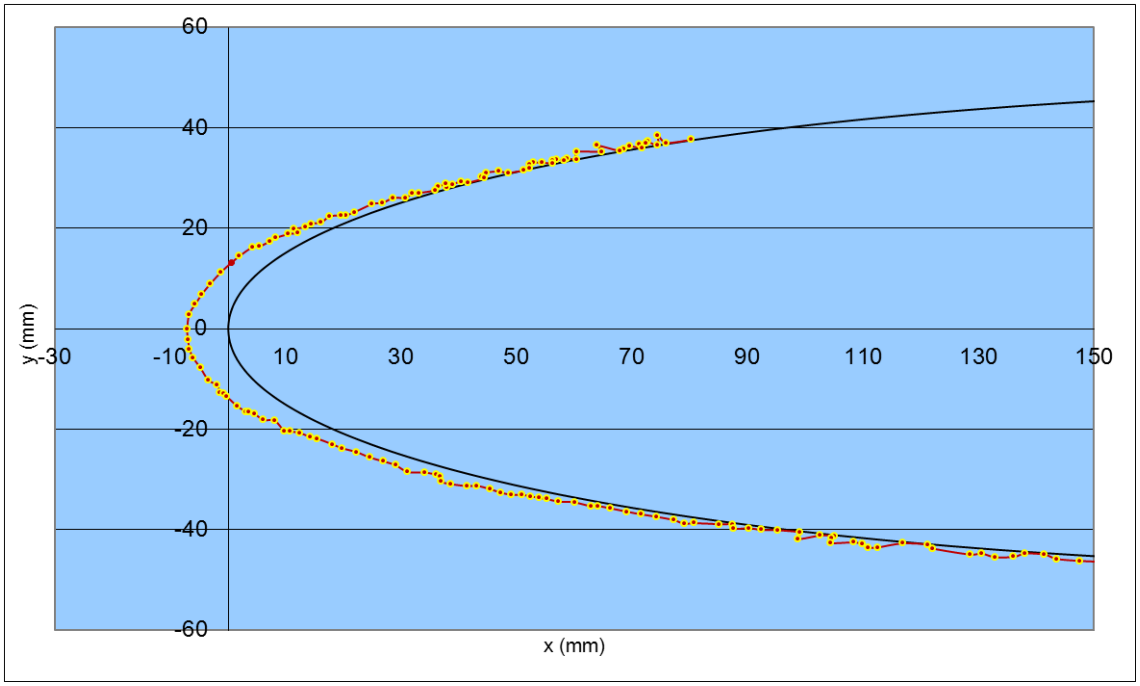

Figure 5-4 the ice shape in rime ice regime on NACA0012 wing airfoil. M=0.2, LWC=0.22 g/m^3, T=-25ºC and MVD=215 μm. [EXTICE icing test campaign DGA, France 2010]

Figure 5-4 shows an example of the ice accretion in SLD rime regime which can represent the catch efficiency of the wing section.

5.2 Water Film Thickness Estimation

As illustration of how to use the semi-empirical method we have discussed in chapter three, we have estimated the water film thickness on a flat plate inside the vertical icing tunnel. Table 5-1 summarizes the acting forces in the middle of the target for a range of velocities and two different impact angles. The CFD calculations have been made as it was discussed in chapter two.

Table 5-1 acting forces on the water film for different airflow conditions

V(m/S)	Impact angle	τ_c (Pa)	$(\partial p/\partial s)_c$ (Pa/m)	$\delta_{air}(\mu m)$	$\tau_c+\delta_{air}\rho_w g.\sin(\alpha)$	$\tau_c+\delta_{air}[\rho_w g.\sin(\alpha)-(\partial p/\partial s)_c]$
30	45°	2.51	-8745	673	7.17	13.06
40		3.78	-15009	653	8.31	18.11
50		5.31	-23116	610	9.54	23.64
60		7.04	-32951	590	11.13	30.57
70		9.01	-44748	577	13.01	38.83
80		11.25	-58639	567	15.18	48.43
30	70°	1.67	-7504	463	3.22	6.70
40		2.32	-12015	403	3.67	8.51
50		3.23	-18733	370	4.47	11.40
60		4.22	-26815	350	5.39	14.78
70		5.34	-36379	327	6.44	18.33
80		6.65	-48258	313	7.70	22.80

We have considered three cases:

- Only airflow shear force as the acting force
- Airflow shear force and the gravitational force
- Combination of the airflow shear force, gravity and pressure gradient

The thickness of the water film (Figure 5-5 and Figure 5-6) is estimated using the semi-empirical methodology presented in chapter three of this thesis.

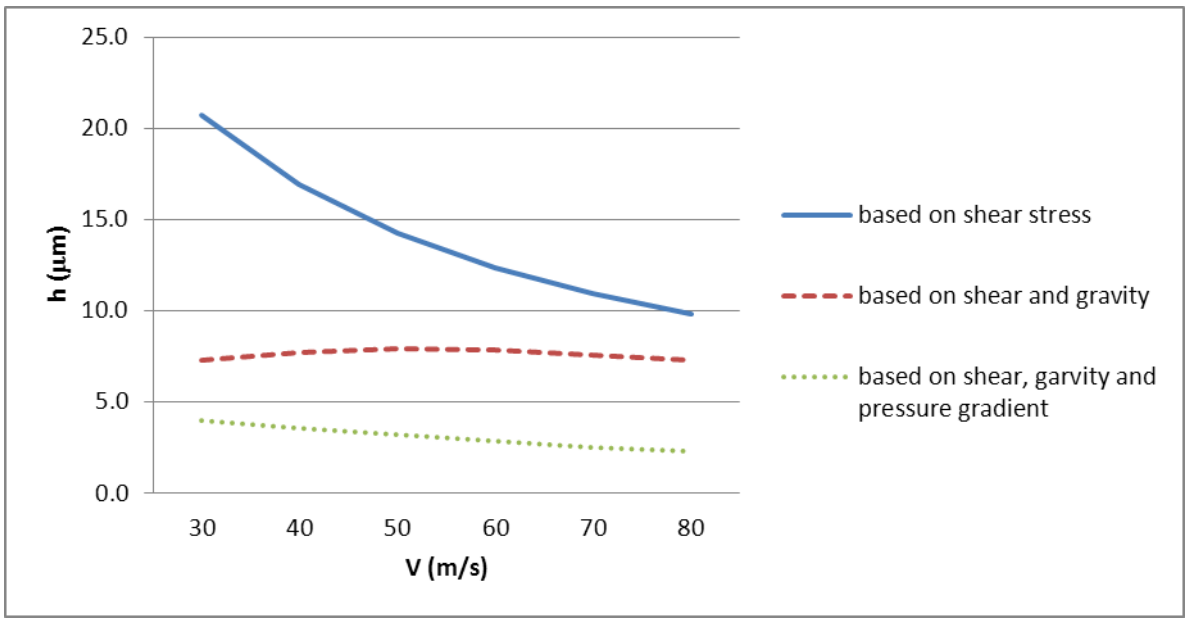

Figure 5-5 water film thickness considering different acting forces for impact angle of 45º

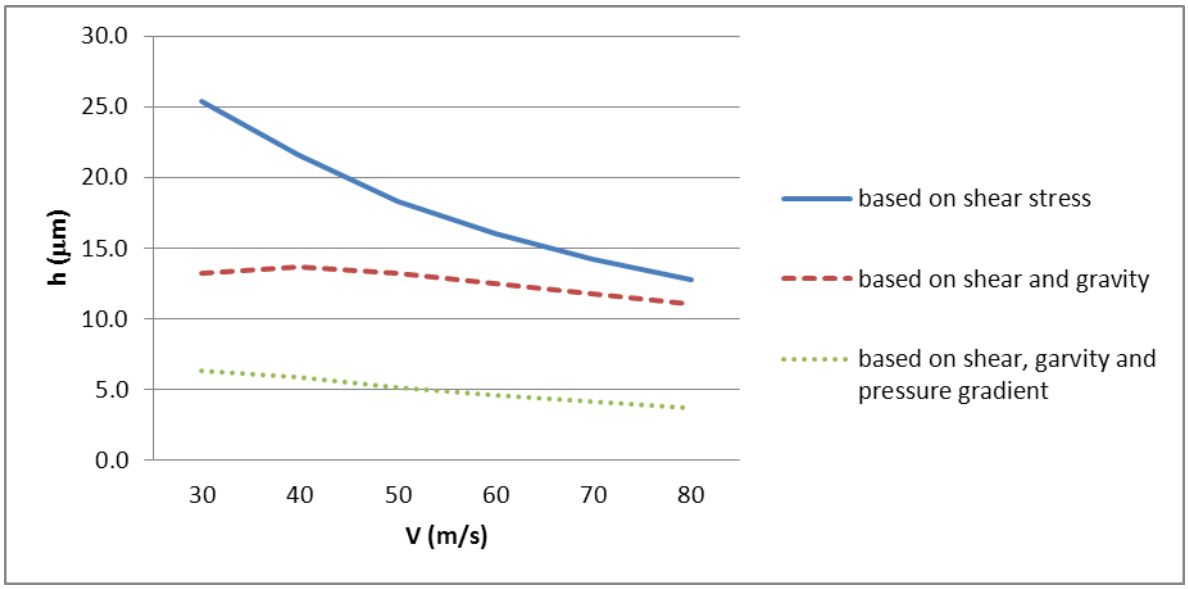

Figure 5-6 water film thickness considering different acting forces for impact angle of 70º

5.3 Characterization of Splashing and Re-impingement

The ratio of the splashed mass is estimated using the final correlations presented in chapter four. The catch efficiency is modified as:

$$\beta_{SLD} = (1 - \frac{m_{sp}}{m_d})\beta \quad \textbf{(5-6)}$$

Where, β is the standard catch efficiency and β_{SLD} is the modified catch efficiency considering the effects of the splashing.

We have not studied the distribution of the secondary droplets size in this work and this was out of the scope of the current research. However, other partners in the EXTICE project were responsible for studying the effects of the different parameters on the size of the secondary droplets. Our partners at ONERA have studied the effect of temperature, velocity and droplet size on the average size of the secondary droplets (Berthoumieu and Feuillebois, 2010). The colleagues at TUD (Technischen Universität Darmstadt) have performed a series of tests on the dry impact conditions (Li *et al.*, 2012).

The conclusion of these works is presented in Figure 5-7 and for wide range of conditions the ratio of the average secondary droplets size can be estimated using the following correlation:

$$\frac{d_{sec}}{d} = 20/\sqrt{Re}$$

$$n_s = (\frac{m_s}{m_d})/\left(\frac{d_{sec}}{d}\right)^3 \quad \textbf{(5-7)}$$

Where, d_{sec} is the average secondary droplets size and n_s is the number of the ejected droplets after impact of droplet with size of d and the Reynolds number

of Re. Some investigations have been made by colleagues in TUD on the distribution of the secondary droplets for the dry impact. The preliminary results have been presented as following (Li *et al.*, 2012).

$$pdf(\xi) = 2.38\xi^{0.94}\exp(-1.23\xi^{1.94})$$

$$\xi = \frac{d_{sec}}{d} \qquad \textbf{(5-8)}$$

In the current work we have characterized the splashed mass by two jets based on the observations of the splashing process. However the idea of the double jet can be expanded to consider more directions for the ejected droplets.

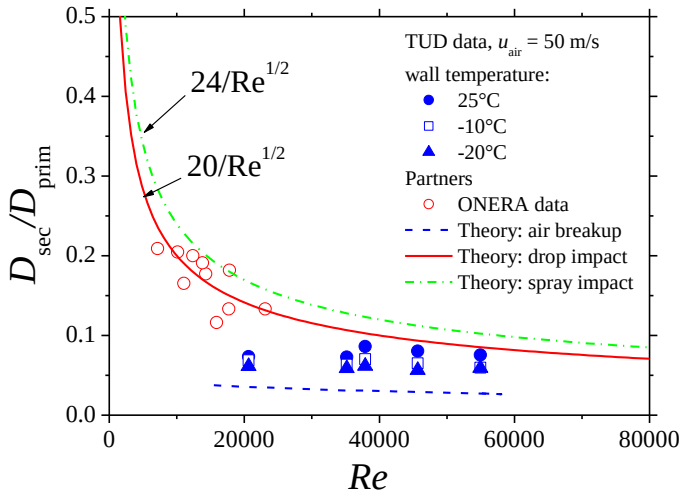

Figure 5-7 the ratio of average secondary droplets size to the initial droplet size vs. Re number: theoretical modelling and experimental data (EXTICE project, 2012)

5.4 Implementation of the Proposed Method in Icing Simulation Codes

The general structure of the icing codes, which has been described in the first chapter, include the CFD calculations, trajectories and catch efficiency calculations, ice accretion and geometry treatment procedures. In practice, the proposed model only affects the procedure of trajectories and catch efficiencies calculations. In standard practice the catch efficiency should be modified taking into account the splashed mass. The trajectories of the secondary droplets should be added to the procedure of the primary droplets trajectories calculations.

In order to implement the proposed methodology in the icing codes, we suggest the following steps:

1. For any element (panel) on the surface, the average acting forces should be obtained using appropriate CFD methods. They are shear stress, gravity and the pressure gradient.
2. The water film velocity is estimated using Equation **(2-8)** or Equation **(2-9)**
3. The water film thickness is estimated using **(3-25)**
4. The ratio of water film thickness over the droplet size (h/d) and the local impact angle (α) should be calculated
5. The splashed mass ratio and the modified catch efficiency are calculated using Equation **(4-11)** and Equation **(5-6)** respectively.
6. The average size of the secondary droplet and the number of ejected droplets are estimated using Equation **(5-7)**. The direction and the velocity of the secondary droplet are estimated using Equations **(4-9)** and **(4-10)**.
7. Re-impingement calculations are made using Equations **(5-2)**, **(5-3)** and **(5-4)**.

A joint work has been started with a team from CIRA who are working in development of MULTICE code to include SLD capabilities. The proposed model will be implemented to the code to perform a series of ice simulation and compare them with experimental results of SLD ice shape. The experimental ice shapes have been provided by DGA, France as a part of the EXTICE icing test

campaigns. The work will include the comparison of the proposed model with other splashing models in the different conditions especially in the glaze regime where we think this model has the potential of improving the simulations. However, this work would be out of the scope of this thesis.

5.5 Comparison of the Proposed Model with other Splashing Models

There are many models developed in order to model the splashing process in relation to the icing problem. They are generally based on the experimental data of the droplet impact but have been modified and tuned for simulation of ice growth. It is a common practice in ice modelling to adjust different models, here the splashing model, to best predict the ice shapes. The disadvantage of these kinds of models is that their relatively accurate for the set of ice shapes which have been adjusted for. The approach of the EXTICE project was to come out with some models and theories which are based on the droplet dynamics, water film behaviour and surface conditions rather than adjustment of a proposed model to best fit with the available ice shapes. Although we believe that even such models cannot necessarily improve the SLD ice prediction significantly, these are currently the most appropriate solutions to deal with the SLD icing problem.

Li and his colleagues (2009) have been performed a critical review on the available SLD models which has been used in the EXTICE project for the purpose of the comparison. Also Wright and Potapczuk (2003) summarized many different SLD models especially for splashing process which is categorized as the first order effect of SLD icing problem. One of the widely used models for splashing is the model that was proposed by Mundo (Mundo *et al.*, 1995). This model has been chosen for comparison purposes; the other models have similar general form and methodology to model the splashing process.

In this model, splashing is characterized by a single factor which depends on the velocity and the size of the droplet.

$$K = \left(\frac{\rho_w^3 d^3 V_n^5}{\sigma^2 \mu_w}\right)^{1/4} \quad \textbf{(5-9)}$$

According to this model splashing occurs when $K \geq 57.7$. This result is widely accepted within the icing community and we have tested the validity of this assumption at the beginning of this work for droplet size between $400\mu m$ and $1.2mm$. Our own experimental findings showed that the threshold of splashing (i.e. the minimum speed which splashing occurs at) is in good agreement with the Mundo's model (Mundo *et al.*, 1995). In our proposed splashing model, we use the same splashing threshold. It should be noted that the splashing threshold depends on the ratio of the water film thickness to droplet size ($\hat{h} = h/d$). When $\hat{h}$ is small, the effects of splashing becomes more important (Purvis and Smith, 2004). For typical SLD icing problems, the K parameter is big enough to satisfy ($K \geq 57.7$). On other hand, as was seen in estimation of the water film thickness, the ratio of $\hat{h}$ is small and thus splashing will take place. Generally when we are dealing with droplet size in the order of $100\ \mu m$ and larger, we assume that splashing is taking place.

The outcomes of the splashing model of Mundo are the average size of the secondary droplets, number of the secondary droplets (or equivalently the splashed mass) and the average direction of the secondary droplets. The ratio of secondary droplet size to the incoming droplet size and number of the secondary droplets are assumed to be function of Kfactor as follows:

$$\frac{d_{sec}}{d} = 8.27e^{-0.0281K}$$
$$n_{sec} = 1.676 \times 10^{-5} K^{2.539} \quad \textbf{(5-10)}$$

Where, d_{sec} is the average size of the ejected (secondary) droplets and n_s is number of the secondary droplets. It is clear that the splashed mass is related to these parameters by:

$$\frac{m_s}{m_d} = n_s \left(\frac{d_{sec}}{d}\right)^3 \quad \textbf{(5-11)}$$

The secondary droplets are modelled by a single velocity vector and the tangential and vertical component of the ejected drops are given as:

$$\frac{V_{sec,t}}{V_t} = 1.337 - 1.318\frac{d_{sec}}{d} + 2.339\left(\frac{d_{sec}}{d}\right)^2$$
$$\frac{V_{sec,n}}{V_n} = -0.249 - 2.959\frac{d_{sec}}{d} + 7.749\left(\frac{d_{sec}}{d}\right)^2 \quad \textbf{(5-12)}$$

Where, $V_{sec,t}$ and $V_{sec,n}$ are the tangential velocity of the ejected drops and the normal velocity respectively. When the structure of this model is compared with our proposed model we can notice the following points:

- Although the models address the splashing threshold from different aspects, both models indicate that in the typical SLD icing problem, splashing is taking place for droplets of size of $100\mu m$ and larger.
- In Mundo's model splashing characteristics are only dependant on the incoming droplet velocity and size while in the proposed model we try to relate the splashing characteristics not only to the incoming droplet velocity and size but on the surrounding airflow field and the presence of the liquid water film.
- In Mundo's model the splashing is taking place in one singular point, which is in clear contradiction with the observations of the splashing in

the icing tunnel. In our proposed model, we defined geometry for the corona (base width, top width and height) and this allows as modelling the splashing in more realistic manner.

- As a result from the observations and the modelling we have characterized the secondary droplets with two ejected jets, while in Mundo's model the secondary droplets are modelled with a single jet.
- The upper limit of the splashed mass in the Mundo's model is about 15% of the incoming droplet mass. In our model this ratio can be up to 90% in some cases of the large droplets and high velocity impact near the stagnation zone. However, it should be noticed that our model it can be valid only if the re-impingement is taken in account. Generally the SLD models overestimate the collection efficiency (and subsequently the ice thickness) near the stagnation zone especially in the glaze regime. We believe that the type of SLD model, which take into account the local airflow condition, have the potential to deal with this problem. This should be investigated in more detail in the future works when the proposed model is implemented in icing codes.

6 Numerical Modelling of Solidification of Thin Water Film and Roughness Development using LBM

6.1 Lattice Boltzmann Method

The Lattice Boltzmann method is one of the computational methods based on the particle kinetic theory (Succi, 2001). In this method the main parameter is the Particle Distribution Function (PDF) which can describe the state of the system in conjunction with velocity space. The lattice Boltzmann method was introduced in the early 1990's as an alternative to discrete lattice methods which had the disadvantage of statistical noises. In the LBM instead of tracking the discrete particles and modelling their collision, a continuous PDF models the convection and collision of the particles. In other words in the LBM we do not distinguish between different particles and this would decrease the computations dramatically.

In recent years this method has been developed and used widely in different areas of science and technology (Sukop and Throne, 2006). The advantages of LBM which, make it a popular and efficient method can be summarized as followings:

- The governing equations are linear and mathematically simple
- It needs simple grids
- It is suitable for complex geometries
- It is very strong in modelling multi-phase and multi component problems
- Its spatial accuracy is second order
- It is explicit and time accurate
- It has outstanding efficiency in parallel computing

The most general form of transport equation is Boltzmann equation which can be written as **(6-1)**. This equation was introduced for the first time by the famous scientist Boltzmann at the end of 19^{th} century.

$$\frac{\partial f}{\partial t} + \vec{c}.\nabla_{\boldsymbol{x}} f + F.\nabla_{\boldsymbol{c}} f = \Phi(f) \qquad \textbf{(6-1)}$$

Where f is the particle distribution function in space and time, $\boldsymbol{F}$ is the external force applied to the system, $\vec{c}$ is the velocity space and Φ is the collision term. The term on the left of **(6-1)** is the total rate of the change in the PDF caused by changes in time, position and the momentum of the particles. The right hand term is the change in the PDF because of the collision between the particles. The discrete form of the **(6-1)** can be written as **(6-3)** when a finite set of velocities are considered instead of infinite possible velocity and directions for the particle movement. The collision term is modelled by idea of Bhatnagar–Gross–Krook (BGK) which considers the collision term as the tendency of system to get its equilibrium state (Succi, 2001). The details of the equilibrium distribution function are given in several LBM textbooks (Succi, 2001; Sukop, 2006; Wolf-Gladrow, 2005). The continuous Boltzmann equation with assumption of single relaxation time (BGK model) can be expressed as follows:

$$\frac{\partial f}{\partial t} + \vec{c}.\nabla_{\boldsymbol{x}} f + F.\nabla_{\boldsymbol{c}} f = -\frac{1}{\tau_f}(f_k - f_k^{eq}) \qquad \textbf{(6-2)}$$

and the discrete version of this equation can be written as:

$$f_k(\vec{x} + \Delta t\vec{c}_k, t + \Delta t) - f_k(\vec{x}, t) + F_k = -\frac{\Delta t}{\tau_f}(f_k - f_k^{eq}) \qquad \textbf{(6-3)}$$

Where, f_k is the probability of particle moving in the $k-th$ direction with velocity of $\vec{c}_k$ in position of $\vec{x}$ and in time t. The external force in the $k-th$ direction is F_k, and f_k^{eq} is the PDF in the equilibrium state. The BGK model considers the collision term as the tendency of the system to reach its equilibrium state. The term f_k^{eq} is defined for the hydrodynamic system in such a way to satisfy the incompressible Navier-Stokes equation. For the hydrodynamic systems the mechanism of pushing the system towards its equilibrium is the diffusion and characteristics of the diffusion, which is the viscosity, is related to the relaxation time as follows:

$$\nu = {c_s}^2(\tau_f - \frac{1}{2}) \quad \textbf{(6-4)}$$

It can be proven that for the isothermal flows the speed of sound in the lattice units is $\sqrt{1/3}$ and therefore the relation between the relaxation time and the fluid viscosity is:

$$\tau_f = 3\nu + \frac{1}{2} \quad \textbf{(6-5)}$$

The lattice units are different from the physical and non-dimensional units although the dimensionless parameters (such the Reynolds number) are the same for all three systems of units. Consider a hydrodynamic problem with length scale of L_0, velocity scale of U and viscosity of ν. For the purpose of discretization of the system, the length scale is divided into N elements and the time scale t_0, is reached in N_{iter} iterations. In the lattice units (discrete space), we use the number of elements and the number of the iterations as the scales of length and time respectively. This would help to study the errors associated

with the discretization and also the stability of the numerical solutions. This means that in the lattice units both values of the grid size and the time step are unity. Thus in Equation **(6-3)** we have that ($\Delta t = 1$), also the lattice speed $\vec{c}$ has the magnitude of unity and only their direction varies. This equation is rewritten as:

$$f_k(\vec{x} + \vec{e}_k, t + 1) - f_k(\vec{x}, t) + F_k = -\frac{1}{\tau_f}(f_k - f_k^{eq}) \qquad \textbf{(6-6)}$$

Where, $\vec{e}_k$ is the direction of $k - th$ lattice velocity.

Notice that all the variables in **(6-6)** and other discrete LB equations are in the lattice units. Table 6-1 summarizes the different expression of the scales for physical, non-dimensional and lattice unit systems. It can be seen that for all systems, the Reynolds number, which defines the hydrodynamic problems, is the same.

Table 6-1 the scales in different systems of units

Unit system	Length scale	Velocity scale	Time Scale	Viscosity	Grid size	Time step
Physical	L_0	U	$t_0 = L_0/U$	ν	L_0/N	t_0/N_{iter}
Non-dimensional	1	1	1	$\frac{1}{Re} = \frac{\nu}{UL_0}$	$\delta_x = 1/N$	$\delta_t = \frac{1}{N_{iter}} = \frac{1}{N\widetilde{U}}$
Lattice	N	$\widetilde{U} = \frac{\delta_x}{\delta_t}$	$N_{iter} = \widetilde{U}N$	$N\widetilde{U}/Re$	1	1

The size of the grid spacing (or the number of elements) is the major parameter to have control over the accuracy of the simulations. In practice, the length

scale and the velocity scale in the lattice system are chosen based on the following constraints:

1. As the LBM is a second order scheme, the error of the discretization is proportional to (δ_x^2). This term should be small enough to achieve accurate simulations ($\delta_x^2 \ll 1$).
2. The LBM presented here is valid for the incompressible limit; therefore the lattice Mach number should be small enough to avoid the compressibility effects. The Mach number of the lattice is:

$$M = \frac{\widetilde{U}}{c_s} = \frac{\widetilde{U}}{\sqrt{1/3}} \qquad \textbf{(6-7)}$$

The error associated with the compressibility errors is in the order of (M^2). Thus the constraint here is ($M^2 \ll 1$).

3. The relaxation time should be close to the unity to avoid the numerical instabilities. The relaxation time is a function of the lattice viscosity as it was stated in Equation **(6-5)**. The lattice viscosity depends on the simulation parameter (Re), number of cells (N) and the lattice reference velocity ($\widetilde{U}$). Then the constraint reads that ($N\widetilde{U} \sim Re/6$).
4. The error associated with the compressibility error should be in the same order of the discretization error to keep the scheme with second order accuracy ($\delta_t \sim \delta_x^2$).
5. The hydrodynamic limit of the LB equations is valid with the continuum assumption which considers the fluid to be continuous. To satisfy this, the ratio of the mean free path of the particles to the length scale should be small. This ratio is proportional to the Knudsen number and also is proportional to the ratio of the Mach number to the Reynolds number ($M/Re \ll 1$).

The equilibrium particle distribution function (f^{eq}) is worked out for any particular lattice in order to satisfy the Navier-Stokes equation in the continuum limit where ($M/Re \ll 1$). It can be shown that appropriate values of the relaxation time and equilibrium function satisfy the flow equations of this form:

$$\frac{\partial \vec{u}}{\partial t} + \vec{u}\nabla\vec{u} = -\frac{1}{\rho}\nabla p + \nu\nabla^2\vec{u} + \vec{F}$$

$$\nabla.\vec{u} = 0 \qquad \textbf{(6-8)}$$

Where, p is the thermodynamic pressure. It is more convenient to use the non-dimensional form of the equations in the simulation process. By choosing appropriate scales for the velocity and length for any system, the set of Equation **(6-8)** can be expressed in the non-dimensional form. The only difference is to substitute the viscosity with ($1/Re$).

In this work we have used two different lattice arrangements for the two and three dimensional problems. The details of the flow and the thermal solvers are discussed in the next sections. Then a potential method to deal with the solidification in the icing problem is presented. Some preliminary results on modelling the solidification of the moving water film and the roughness development inside the water film are presented in the end of this chapter.

6.2 Developing Two Dimensional Flow and Thermal Solver

A two dimensional lattice Boltzmann flow solver has been developed to simulate the flow of the moving thin water film. Figure 6-1 shows the lattice is used in the current work. This lattice is known as D2Q9 and means that it is a two dimensional lattice with nine possible directions for the movement of the particles. There are other lattices used for the two dimensional problem with higher and lower number of directions compared to D2Q9. The higher order lattices are generally used to simulate the compressible flow with effects such

as shock waves. They are used for modelling the thermal flow too as it will be discussed later. The low order lattices such as D2Q5 and D2Q7 are less common because of their poor accuracy to simulate the hydrodynamic problems.

In the last section we explained how to set the value of the relaxation time. In order to solve Equation **(6-6)** we need to find an explicit expression for the equilibrium particle distribution function (f^{eq}). There are several methods to find the equilibrium state of a system based on the statistical approach and also based on the relation between the macro features of the system and the dynamics of the particles. The first approach is not in the interest of this work but the second approach is the method with more potential applicability in the engineering problems.

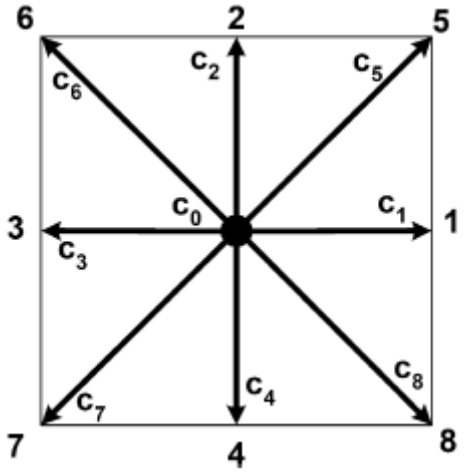

Figure 6-1 D2Q9 lattice used for the two dimensional LBM flow solver

The mass conservation for any lattice states that the summation of the all PDF's is the mass (or density) of the fluid on that lattice. Also the mean momentum of the flow on the lattice is the summation of momentums of the particles travelling in the all directions. The requirement of the conservation of energy is that the sensible energy (the internal energy or temperature) of the flow should be the

summation of the kinetic energy of the particles in all directions. These can be expressed mathematically for D2Q9 lattice (with $|c| = 1$) as follows:

$$\sum_{k=0}^{8} f_k = \rho$$

$$\sum_{k=0}^{8} f_k \, \vec{e}_k = \rho \vec{u} \qquad \textbf{(6-9)}$$

$$\sum_{k=0}^{8} f_k (\vec{e}_k)^2 = \rho e$$

Where, ρ is the density, $\vec{u}$ is the mean velocity of the flow and e is the internal energy. For an isothermal system, the internal energy is constant and it is equal to $(1/3)$ in the lattice unit system (Succi, 2001). On other hand according to Equation **(6-3)** and with some mathematics, one can show that:

$$\sum_{k=0}^{8} f_k^{eq} = \rho$$

$$\sum_{k=0}^{8} f_k^{eq} \, \vec{e}_k = \rho \vec{u} \qquad \textbf{(6-10)}$$

$$\sum_{k=0}^{8} f_k^{eq} (\vec{e}_k)^2 = \rho e$$

The last set of equations with some other assumption, which can be found in the textbooks, lead to the following expression for the equilibrium particle distribution functions:

$$f_k^{eq} = \frac{\rho w_k}{9}\left(1 + 3\vec{u}.\vec{e}_k + \frac{9}{2}(\vec{u}.\vec{e}_k)^2 - \frac{3}{2}\vec{u}.\vec{u}\right)$$

$$w = \{4,1,1,1,1,0.25,0.25,0.25,0.25)$$ **(6-11)**

$$e_x = \{0\ ,1\ ,0\ ,-1,0\ ,1\ ,-1,-1,1\ )$$

$$e_y = \{0\ ,0\ ,1\ ,0\ ,-1\ ,1\ \ ,1\ ,-1,-1\ )$$

It should be noted that f^{eq} is only a function of the macro variables. In each time step f^{eq} is calculated based on macro variables calculated from the f of the previous time step to guarantee the full explicitly of the scheme. The initial condition for a hydrodynamic system is usually specified by ρ and $\vec{u}$. According to **(6-11)** this means that f^{eq} is specified for the first time step and the same scenario happens for the next time steps.

For the sake of simplicity, the Equation **(6-6)** is solved in three steps in order to update $f(x,t+1)$ based on $f(x,t)$. The first step is to evaluate the collision term and update $f(x,t+1)$ according to **(6-6)** and **(6-11)**. If there is any external force such as gravity, the force term F_k should be added to $f(x,t+1)$. The final step is to stream the PDF's on the different directions which means assigning $f(x,t+1)$ to $f(\vec{x}+\vec{e}_k,t+1)$. This step insures the modelling of the convection of the hydrodynamic system. Some of the details of the LBM code are given in Appendix B of this thesis.

In the developed code, we have implemented many different boundary conditions in order to be able to model different conditions that the water film could face. The implemented boundary conditions are solid wall, immersed solid body, inlet with known velocity, inlet with known pressure, outlet with known velocity, outlet with known pressure, moving solid wall and periodic condition. On any boundary some of the PDF's are known as they are coming from inside the domain by streaming. However, the unknown PDF's are evaluated using the known macro variables on that boundary using **(6-9)**. For the no-slip boundary

condition on the walls, the bounce-back boundary conditions is used, which simply swap any PDF with the PDF of the opposite direction to satisfy no-slip condition. Consider a two dimensional flow and a Cartesian uniform grid to be used to simulate the flow using a LBM solver. The flow is moving from left to right and the lattice used is one shown in Figure 6-1. The boundary conditions are specified as following:

- Inlet flow (from left side of the grid) with known velocity, u_{in} and v_{in}. In this case f_1, f_5 and f_8 are unknown and the rest of PDF's are coming from inside the domain. The unknown PDF's are calculated as:

$$
\begin{aligned}
f_1 &= f_3 + \frac{2}{3}\tilde{\rho}u_{in} \\
f_5 &= f_7 + \frac{1}{6}\tilde{\rho}u_{in} + \frac{1}{2}\tilde{\rho}v_{in} - \frac{1}{2}(f_2 - f_4) \\
f_8 &= f_6 + \frac{1}{6}\tilde{\rho}u_{in} - \frac{1}{2}\tilde{\rho}v_{in} + \frac{1}{2}(f_2 - f_4) \\
\tilde{\rho} &= f_0 + f_2 + f_4 + \frac{2}{1 - u_{in}}(f_3 + f_6 + f_7)
\end{aligned}
\qquad \textbf{(6-12)}
$$

- Outlet flow (from right side of the grid) with known velocity, u_{out} and v_{out}. In this case f_3, f_6 and f_7 are unknown and the rest of PDF's are coming from inside the domain. The unknown PDF's are calculated as:

$$f_3 = f_1 - \frac{2}{3}\tilde{\rho}u_{out}$$

$$f_6 = f_8 - \frac{1}{6}\tilde{\rho}u_{out} + \frac{1}{2}\tilde{\rho}v_{out} - \frac{1}{2}(f_2 - f_4) \quad \textbf{(6-13)}$$

$$f_7 = f_5 - \frac{1}{6}\tilde{\rho}u_{out} - \frac{1}{2}\tilde{\rho}v_{out} + \frac{1}{2}(f_2 - f_4)$$

$$\tilde{\rho} = f_0 + f_2 + f_4 + \frac{2}{1 + u_{out}}(f_1 + f_5 + f_8)$$

- Outlet flow (from right side of the grid) with known pressure (or density as the system is isothermal) of ρ_{out}. In this case f_3, f_6 and f_7 are unknown and the rest of PDF's are coming from inside the domain. The unknown PDF's are calculated as:

$$f_3 = f_1 - \frac{2}{3}\tilde{u}\rho_{out}$$

$$f_6 = f_8 - \frac{1}{6}\tilde{u}\rho_{out} - \frac{1}{2}(f_2 - f_4) \quad \textbf{(6-14)}$$

$$f_7 = f_5 - \frac{1}{6}\tilde{u}\rho_{out} + \frac{1}{2}(f_2 - f_4)$$

$$\tilde{u} = -1 + (f_0 + f_2 + f_4) + \frac{2}{\rho_{out}}(f_1 + f_5 + f_8)$$

- Inlet flow (from left side of the grid) with known pressure (or equally known density) of ρ_{in}. In this case f_1, f_5 and f_8 are unknown and the rest of PDF's are coming from inside the domain. The unknown PDF's are calculated as:

$$f_1 = f_3 + \frac{2}{3}\tilde{u}\rho_{in}$$

$$f_5 = f_7 + \frac{1}{6}\tilde{u}\rho_{in} - \frac{1}{2}(f_2 - f_4) \qquad \textbf{(6-15)}$$

$$f_8 = f_6 + \frac{1}{6}\tilde{u}\rho_{in} + \frac{1}{2}(f_2 - f_4)$$

$$\tilde{u} = 1 - (f_0 + f_2 + f_4) + \frac{2}{\rho_{in}}(f_3 + f_6 + f_7)$$

- Moving wall (from left to right) with known velocity u_{lid}. In this case f_4, f_7 and f_8 are unknown and the rest of PDF's are coming from inside the domain. The unknown PDF's are calculated as:

$$f_4 = f_2$$

$$f_7 = f_5 - \frac{1}{2}\tilde{\rho}u_{lid} + \frac{1}{2}(f_1 - f_3) \qquad \textbf{(6-16)}$$

$$f_8 = f_6 + \frac{1}{2}\tilde{\rho}u_{lid} - \frac{1}{2}(f_1 - f_3)$$

$$\tilde{\rho} = f_0 + f_1 + f_3 + 2(f_2 + f_5 + f_6)$$

The similar method can be adopted for any other boundary condition. It should be noted that the method we have used for implementation of the boundary conditions is not unique. Nevertheless we have tried to use stable and accurate boundary conditions implementation based on the literature and the related works.

The first step after developing the code is to validate it using standard benchmark problems. One of these standard test cases is the two dimensional

cavity lid-driven flow problem. There are a number of high accuracy solutions for different Reynolds numbers which can be used to validate the LBM code results (Ghia *et al*, 1982). Figure 6-2 and Figure 6-3 show the streamlines of flow in the cavity for two different Reynolds numbers of 400 and 800. The flow pattern in the both cases is similar to other numerical simulations of the cavity problem for the same Re numbers (Chen *et al*, 1994). For quantitative comparison of the results, the locations of centres of the vortexes are compared to other numerical results. There are three vortexes in both of the test cases. The results of the current LBM code are compared with other LBM results (Chen *et al*, 1994) and results of high resolution CFD simulations (Ghia *et al*, 1982) and very good agreement is found between them. The difference in predicting the location of the centres of vortexes is only about 1% as it can be seen in Table 6-2 and Table 6-3.

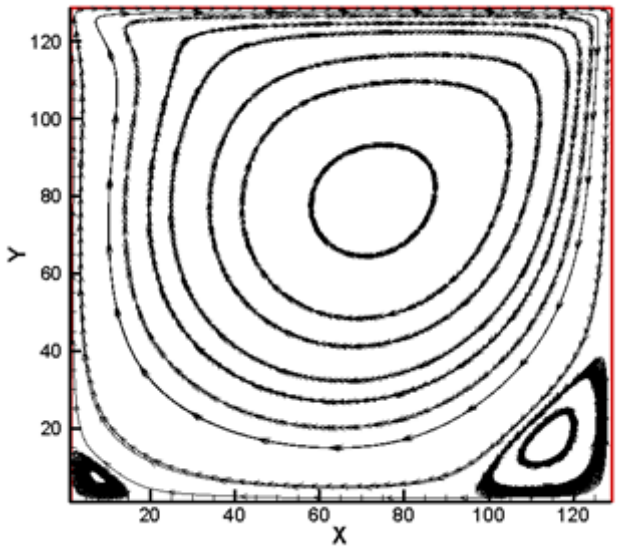

Figure 6-2 Cavity lid driven flow simulation by LBM, Re=400, grid 128x128

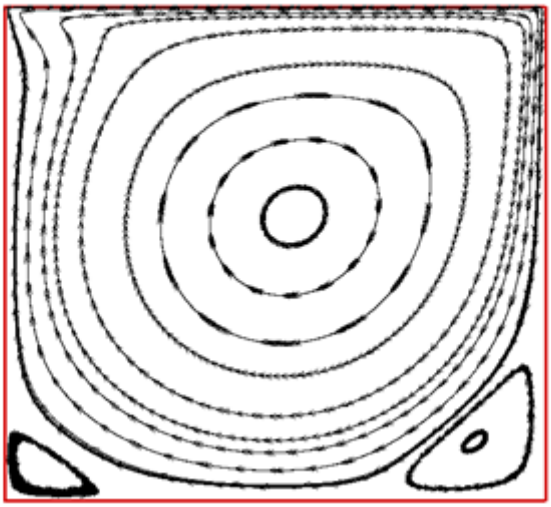

Figure 6-3 Cavity lid driven flow simulation by LBM, Re=800, grid 256x256

Table 6-2 Vortex centres location in the cavity problem, Re=100

	Primary vortex		Lower let vortex		Lower right vortex	
	x	Y	X	y	x	Y
Ghia	0.6172	0.7344	0.0313	0.0391	0.9453	0.0625
Chen	0.6196	0.7700	0.0392	0.0353	0.9451	0.0627
Present	0.6160	0.7391	0.0372	0.0383	0.9401	0.0629

Table 6-3 Vortex centres location in the cavity problem, Re=400

	Primary vortex		Lower let vortex		Lower right vortex	
	x	Y	X	y	X	Y
Ghia	0.5547	0.6055	0.0508	0.0496	0.8906	0.1250
Chen	0.5608	0.6078	0.0549	0.0510	0.8902	0.1255
Present	0.5580	0.6084	0.0518	0.0491	0.8839	0.1254

In order to model the solidification we need to model the thermal problem and find the temperature field in the system. The LBM framework discussed in this section is to model the hydrodynamics of the system when the system is assumed to be isothermal. There are several approaches to model the heat transfer and thermal problem using LBM (Succi, 2001). The most common approaches are:

- Multispeed model
- Modify the collision term
- Using another distribution function

The third approach has the minimum numerical instabilities and it is used widely especially to model the flow thermodynamics in the incompressible regime (He *et al*, 1998). In this approach another distribution function is used to model the temperature in the lattice. For D2Q9 lattice, the temperature filed is calculated using the new proposed PDF (g_k) as:

$$T = \sum_{k=0}^{8} g_k \qquad \textbf{(6-17)}$$

The discrete version of the Boltzmann equation over the lattice is expresses in the following form:

$$g_k(\vec{x} + \vec{e}_k, t+1) - g_k(\vec{x}, t) + G_k = -\frac{1}{\tau_T}(g_k - g_k^{eq}) \qquad \textbf{(6-18)}$$

Where, G_k represents any source or sink of the energy and τ_T is the relaxation time of the system which characterizes the thermal equilibrium. The collision

term is modelled by single relation time based on BGK assumption. Similar to the hydrodynamic modelling, the relaxation time for the thermal modelling is related to the thermal diffusivity of the fluid (α_T). For the hydrodynamic modelling the relaxation time was related to the viscosity of the fluid (ν). These two parameters are scaled by the Prandtl number ($Pr = \nu/\alpha_T$) which is about 7 for the liquid water.

$$\tau_T = 3\alpha_T + \frac{1}{2} \qquad \textbf{(6-19)}$$

It can be shown that Equation **(6-18)** and the relaxation time as expressed in **(6-19)** in conjunction with an appropriate equilibrium PDF function of (g^{eq}) model the energy equation for the incompressible flows in form of:

$$\frac{\partial T}{\partial t} + \vec{u}.\nabla T = \alpha_T \nabla^2 T \qquad \textbf{(6-20)}$$

$$g_k^{eq} = \frac{T w_k}{9}\left(-\frac{3}{2}\vec{u}.\vec{u}\right) \qquad k = 0$$

$$g_k^{eq} = \frac{T w_k}{9}\left(\frac{3}{2} + \frac{3}{2}\vec{u}.\vec{e}_k + \frac{9}{2}(\vec{u}.\vec{e}_k)^2 - \frac{3}{2}\vec{u}.\vec{u}\right) \qquad k = 1-4 \qquad \textbf{(6-21)}$$

$$g_k^{eq} = \frac{T w_k}{9}\left(3 + 6\vec{u}.\vec{e}_k + \frac{9}{2}(\vec{u}.\vec{e}_k)^2 - \frac{3}{2}\vec{u}.\vec{u}\right) \qquad k = 5-8$$

The energy equation can be rewritten in the non-dimensional form as:

$$\frac{\partial T}{\partial t} + \vec{u}.\nabla T = \frac{1}{RePr}\nabla^2 T \qquad \textbf{(6-22)}$$

In this model the effect of the dissipation term is neglected and it is assumed that the properties of the fluid such as the viscosity and the diffusivity are constant. It should be noticed that for low speed flows, such the problem of the moving water film, the effect of the viscous dissipation term can be neglected safely. Let us consider a typical moving water film in the icing problem to evaluate different non-dimensional parameters governing the problem. In chapter 2 and five we have presented some typical values for the different parameters of the water film in the icing problem.

- The length scale is the thickness of the water film which is typically in order of ($h = 10\ \mu m$).
- The velocity scale is the maximum velocity of the water film and it is typically ($V_f = 5 \times 10^{-2}\ m/s$).
- The temperature variation in the water film which can be ($\Delta T = 10°K$).
- The Prandtl number for the water is ($Pr = 7$), the kinematic viscosity ($\nu = 1.8 \times 10^{-6}\ m^2/s$) and the heat capacity is ($c_p = 4.2 \times 10^3 J/kg°K$).
- The Reynolds number is about 0.3 and ($1/Re \approx 3$) scales the diffusion term in the momentum equation. This shows that the diffusion term plays an important role alongside the convection and the pressure gradient terms.
- The conduction term in the energy equation is scaled by the parameter ($1/(RePr)$) which is about 0.5 for this problem. This indicates that this term has importance in the same order of the convection term in the energy equation.
- The viscous dissipation term is scaled by the Eckert number which is defined as ($Ec = V^2/c_p \Delta T$). This term for the problem with the aforementioned conditions is about ($Ec \approx 10^{-7}$). This clearly indicates

that the dissipation effects have negligible effects in the energy balance of the system.

Three different thermal boundary conditions have been developed in this work to model the solidification of the water film and they are:

- Periodic boundary condition:
- Fixed temperature boundary condition
- Fixed heat flux boundary condition (the adiabatic wall is a special case of this type of boundary condition)

The periodic boundary condition, in the water film problem, is used in case of small variation in the tangential direction. This means that the thermal solution of any part of the water film will be repeated for the other parts. To apply this boundary condition, simply all the PDF's of any side of the periodic condition are allocated for the other side and vice versa.

The implementation of the fixed temperature boundary condition is quite similar to the fixed pressure boundary condition in the hydrodynamics model. For instance consider a fixed temperature of T_H and we want to apply this temperature to the lower wall boundary in a D2Q9 lattice. The known PDF's, which are coming from inside the domain, are: $g_0, g_1, g_3, g_4, g_7$and g_8. The unknown PDF's are calculated as:

$$g_2 = \frac{2}{3}(T_H - \tilde{T})$$

$$g_5 = \frac{1}{6}(T_H - \tilde{T}) \qquad \textbf{(6-23)}$$

$$g_6 = \frac{1}{6}(T_H - \tilde{T})$$

$$\tilde{T} = g_0 + g_1 + g_3 + g_4 + g_7 + g_8$$

To work out these relations we should notify the symmetry requirement which implies that g_5 and g_6 should have the same relation. On the other hand g_2 is in the major axis of the lattice and the weight of the PDF in the major axis (i.e. directions 1,2,3 and 4) is 4 times the weight of PDF in the minor axis (i.e. directions 5,6,7 and 8). The weights of the different directions for D2Q69 are given in Equation **(6-11)**.

Consider the lower wall boundary but with fixed heat flux ($q_w = k\frac{\partial T}{\partial y}$) applied on it. To implement this boundary condition, we use a second order finite difference approximation to normal component of the temperature gradient on the wall. After some mathematics, one can show that the boundary condition in the non-dimensional form is implemented as follows:

$$g_2 = \frac{2}{3}(T_w - \tilde{T})$$

$$g_5 = \frac{1}{6}(T_w - \tilde{T})$$

$$g_6 = \frac{1}{6}(T_w - \tilde{T}) \qquad \textbf{(6-24)}$$

$$\tilde{T} = g_0 + g_1 + g_3 + g_4 + g_7 + g_8$$

$$T_w = \frac{4T(I,2) - T(I,3) - 2Re.Pr.q_w}{3}$$

Where, $T(I,2)$ and $T(I,3)$ are the temperature on the first and second nodes above the wall respectively at any wall node (I). The temperature on the wall is $T(I,1)$ which is equal to T_w.

To validate the thermal LBM code, we have performed a series of the simulation for the Rayleigh–Benard free convection problem inside a rectangular domain. Although the physics of this problem is not related directly to what we see in the icing problem, it is beneficial to show the correlation between the energy and

momentum equations in the incompressible limit. In this problem the temperature variation in the system drives the motion of the fluid. Using Boussinesq approximation, an external force is added to the momentum equation in order to model the effect of the temperature variation on the dynamics of the flow (He *et al.*, 1998).

Consider a rectangle with aspect ratio of 2:1. The upper wall temperature is kept at T_c while the lower wall has warmer temperature of T_H. The temperature in the non-dimensional form is defined as:

$$T_{dimensionless} = \frac{T - T_C}{T_H - T_C} = \frac{T - T_C}{\Delta T} \quad \textbf{(6-25)}$$

Thus the upper and lower walls will have non-dimensional temperatures of 0 and 1 respectively. The Boussinesq approximation states that the temperature variation in the domain acts as an external force (buoyancy force) to move the flow and it is approximated as:

$$\vec{F} = g_0 \beta_T (T - T_m)\hat{j} \quad \textbf{(6-26)}$$

Where, g is the gravity acceleration, β_T is the thermal expansion coefficient of the fluid and T_m is the average of the upper and lower walls temperatures. This force is acting in the direction perpendicular to the walls (in the direction of the unit vector $\hat{j}$). The left and right directions are periodic boundaries. The buoyancy force is scaled by the Rayleigh number which is defined as:

$$Ra = \frac{g_0 \beta_T \Delta T H^3}{\alpha_T \nu} \quad \textbf{(6-27)}$$

Where, H is the height of the domain. The velocity scale in the free convection problem is $\sqrt{g\beta_T \Delta T H}$. In the LBM simulations, this term must be kept small as was discussed in the previous section. The non-dimensional governing equations (continuity, momentum and energy) are dependent of Ra and Pr only and they are expressed as:

$$\nabla . \vec{u} = 0$$

$$\frac{\partial \vec{u}}{\partial t} + \vec{u}\nabla\vec{u} = -\frac{1}{\rho}\nabla p + \frac{1}{Re}\nabla^2\vec{u} + \frac{Ra}{PrRe^2}(T - T_m)\hat{j} \quad \textbf{(6-28)}$$

$$\frac{\partial T}{\partial t} + \vec{u}.\nabla T = \frac{1}{PrRe}\nabla^2 T$$

It should be noted that because we defined the reference velocity based on the buoyancy characteristics, the Reynolds number is not independent of the Rayleigh number and the Prandtl number ($Re = \sqrt{Ra/Pr}$).

For the purpose of validation we have considered the Rayleigh-Benard free convection problem with $Ra = 10^4$ and $Pr = 0.71$. Figure 6-4 shows the isothermal lines in domain. To initiate the convection in the system, the initial conditions were slightly deviated from the symmetry. Figure 6-5 shows the laminar streamlines of the flow.

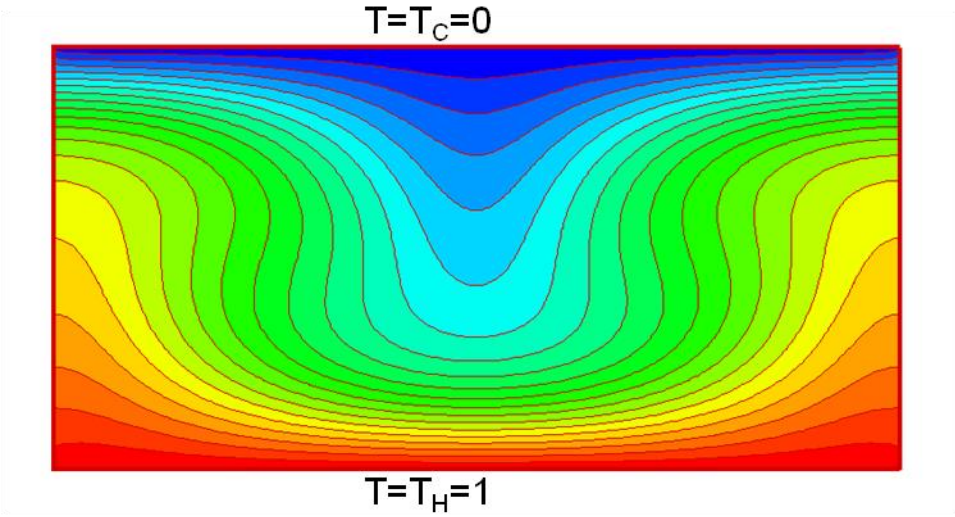

Figure 6-4 the isothermal lines in the Rayleigh-Benard free convection problem, Ra=10000, grid 200x100

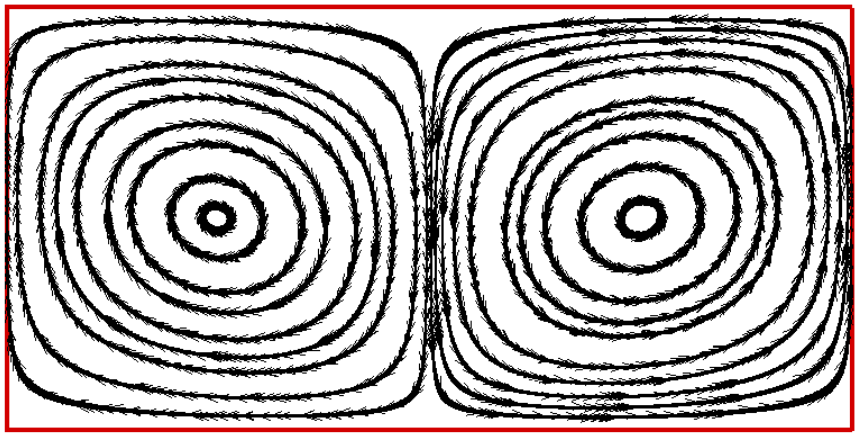

Figure 6-5 the stream lines in the Rayleigh-Benard free convection problem, Ra=10000, grid 200x100

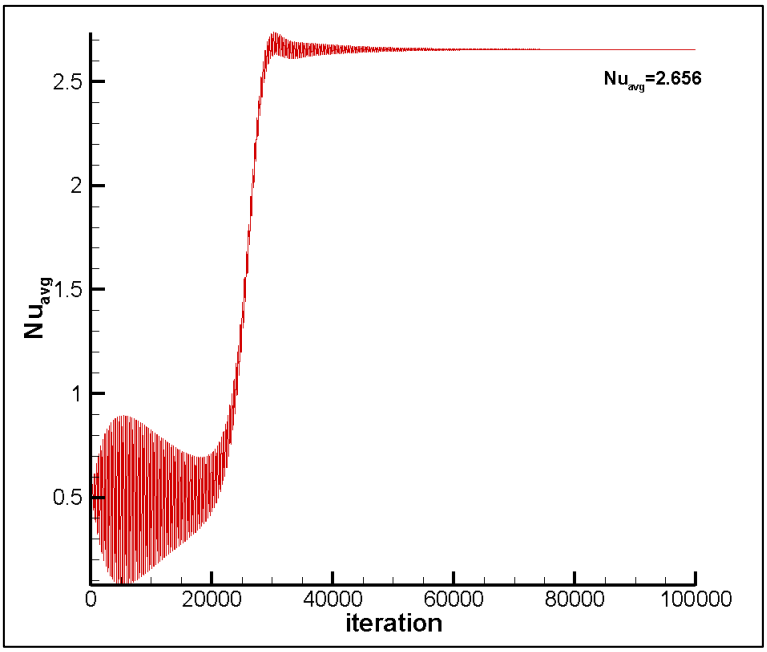

Figure 6-6 the history of the Nusselt number for the Rayleigh-Benard free convection problem, Ra=10000, grid 200x100

Figure 6-6 shows the history of the average Nusselt number (Nu_{avg}) in the domain which represents the overall heat transfer on the walls. The details of the Nusselt number calculation are given in (Davis, 1983). The steady state value of (Nu_{avg}) from the LBM simulation matches other numerical simulations and the analytical solutions (Davis, 1983).

6.3 Developing Three Dimensional Flow and Thermal Solver

The structure of the LBM code is quite similar to the two dimensional version of the code. The same relations are valid for the macro variables in the three dimensional version of the LBM. We have used D3Q19 lattice for the three dimensional simulations which has the similar properties of D2Q9 in the two dimensional simulations. The D3Q19 lattice is suitable for the incompressible flows for both the hydrodynamic and thermal modelling. We have used two different PDF's for modelling the hydrodynamics and the thermodynamics of the flows. Figure 6-7 shows the schematic of the lattice used for the three dimensional simulations.

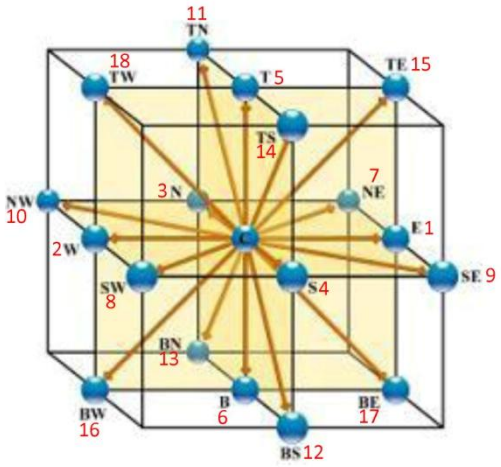

Figure 6-7 D3Q19 lattice used for the three dimensional LBM flow solver

The same methodology, as it is discussed in the previous section, is used to derive the equilibrium PDF's for the hydrodynamic modelling (f^{eq}) and thermal modelling (g^{eq}). The streaming process and evaluation of the collision term remain unchanged for both PDF's. Similar to the two dimensional simulation, the relaxation time in the momentum equation is related to the viscosity of the fluid. The relaxation time for the energy equation is related to the thermal diffusivity of the fluid. The equilibrium particle distribution function of the momentum equation in the three dimension simulation for the incompressible flow is as follows:

$$f_k^{eq} = \frac{\rho w_k}{9}\left(1 + 3\vec{u}.\vec{e}_k + \frac{9}{2}(\vec{u}.\vec{e}_k)^2 - \frac{3}{2}\vec{u}.\vec{u}\right)$$

$$w_k = \begin{Bmatrix} 3 & k = 0 \\ 0.5 & k = 1-6 \\ 0.25 & k = 7-19 \end{Bmatrix} \qquad \textbf{(6-29)}$$

$$e_x = \{0\ ,1\ ,-1\ ,0,0,0,0,1,-1,1,-1,0,0,0,0,1,-1,1,-1\ )$$

$$e_y = \{0\ ,0,0,1,-1,0,0,1,-1,-1,1,1,-1,1,-1,0,0,0,0)$$

$$e_z = \{0,0,0,0,0,1,-1,0,0,0,0,1,-1,-1,1,1,-1,-1,1\ )$$

The equilibrium particle distribution function of the energy equation (without the viscous dissipation term) in the three dimension simulation for the incompressible flow is as follows:

$$g_k^{eq} = \frac{Tw_k}{9}\left(-\frac{3}{2}\vec{u}.\vec{u}\right) \qquad k = 0$$

$$g_k^{eq} = \frac{Tw_k}{9}\left(1 + \vec{u}.\vec{e}_k + \frac{9}{2}(\vec{u}.\vec{e}_k)^2 - \frac{3}{2}\vec{u}.\vec{u}\right) \qquad k = 1-6 \qquad \textbf{(6-30)}$$

$$g_k^{eq} = \frac{Tw_k}{9}\left(2 + 4\vec{u}.\vec{e}_k + \frac{9}{2}(\vec{u}.\vec{e}_k)^2 - \frac{3}{2}\vec{u}.\vec{u}\right) \qquad k = 7-19$$

For the no-slip boundary condition on the walls, the bounce-back boundary conditions is used, which simply swap any PDF with the PDF of the opposite direction to satisfy no-slip condition. Consider a three dimensional flow and a Cartesian uniform grid to be used to simulate the flow using a LBM solver. The flow is moving from west to east and the lattice used is one shown in Figure 6-7. The boundary conditions are specified as follows:

- Inlet flow (from west side of the grid) with known velocity (u_{in}, v_{in}, w_{in}). In this case f_1, f_7, f_9, f_{15} and f_{17} are unknown and the rest of PDF's are coming from inside the domain. The unknown PDF's are calculated as:

$$f_1 = f_2 + \frac{1}{3}\tilde{\rho}u_{in}$$

$$f_7 = f_8 + \frac{1}{2}\tilde{\rho}u_{in} + \frac{1}{2}\tilde{\rho}v_{in} - \frac{1}{2}(f_3 - f_4 + f_{11} - f_{12} + f_{13} - f_{14})$$

$$f_9 = f_{10} + \frac{1}{2}\tilde{\rho}u_{in} - \frac{1}{2}\tilde{\rho}v_{in} + \frac{1}{2}(f_3 - f_4 + f_{11} - f_{12} + f_{13} - f_{14})$$

$$f_{15} = f_{16} + \frac{1}{2}\tilde{\rho}u_{in} + \frac{1}{2}\tilde{\rho}w_{in} - \frac{1}{2}(f_5 - f_6 + f_{11} - f_{12} + f_{14} - f_{13}) \quad \textbf{(6-31)}$$

$$f_{17} = f_{18} + \frac{1}{2}\tilde{\rho}u_{in} - \frac{1}{2}\tilde{\rho}w_{in} + \frac{1}{2}(f_5 - f_6 + f_{11} - f_{12} + f_{14} - f_{13})$$

$$\tilde{\rho} = \frac{2(f_2 + f_8 + f_{10} + f_{16} + f_{18}) + f_0 + f_3 + f_4 + f_5 + f_6 + f_{11} + f_{12} + f_{13} + f_{14}}{1 - u_{in}}$$

- Outlet flow (from east side of the grid) with known pressure (or density as the system is isothermal) of ρ_{out}. In this case f_2, f_8, f_{10}, f_{16} and f_{18} are unknown and the rest of PDF's are coming from inside the domain. The unknown PDF's are calculated as:

$$f_2 = f_1 - \frac{1}{3}\tilde{u}\rho_{out}$$

$$f_8 = f_7 - \frac{1}{6}\tilde{u}\rho_{out} + \frac{1}{2}(f_3 - f_4 + f_{11} - f_{12} + f_{13} - f_{14})$$

$$f_{10} = f_9 - \frac{1}{6}\tilde{u}\rho_{out} - \frac{1}{2}(f_3 - f_4 + f_{11} - f_{12} + f_{13} - f_{14})$$

$$f_{16} = f_{15} - \frac{1}{6}\tilde{u}\rho_{out} + \frac{1}{2}(f_5 - f_6 + f_{11} - f_{12} + f_{14} - f_{13}) \quad \textbf{(6-32)}$$

$$f_{18} = f_{17} - \frac{1}{6}\tilde{u}\rho_{out} - \frac{1}{2}(f_5 - f_6 + f_{11} - f_{12} + f_{14} - f_{13})$$

$$\tilde{u} = \frac{2(f_1 + f_7 + f_9 + f_{15} + f_{17}) + f_0 + f_3 + f_4 + f_5 + f_6 + f_{11} + f_{12} + f_{13} + f_{14}}{\rho_{out}} - 1$$

- Inlet flow (from west side of the grid) with known pressure (or equally known density) of ρ_{in}. In this case f_1, f_7, f_9, f_{15} and f_{17} are unknown and the rest of PDF's are coming from inside the domain. The unknown PDF's are calculated as:

$$f_1 = f_2 + \frac{1}{3}\tilde{u}\rho_{in}$$

$$f_7 = f_8 + \frac{1}{6}\tilde{u}\rho_{out} - \frac{1}{2}(f_3 - f_4 + f_{11} - f_{12} + f_{13} - f_{14})$$

$$f_9 = f_{10} + \frac{1}{6}\tilde{u}\rho_{out} + \frac{1}{2}(f_3 - f_4 + f_{11} - f_{12} + f_{13} - f_{14}) \quad \textbf{(6-33)}$$

$$f_{15} = f_{16} + \frac{1}{6}\tilde{u}\rho_{out} - \frac{1}{2}(f_5 - f_6 + f_{11} - f_{12} + f_{14} - f_{13})$$

$$f_{17} = f_{18} + \frac{1}{6}\tilde{u}\rho_{out} + \frac{1}{2}(f_5 - f_6 + f_{11} - f_{12} + f_{14} - f_{13})$$

$$\tilde{u} = 1 - \frac{2(f_2 + f_8 + f_{10} + f_{16} + f_{18}) + f_0 + f_3 + f_4 + f_5 + f_6 + f_{11} + f_{12} + f_{13} + f_{14}}{\rho_{in}}$$

- Moving top wall (from west to east) with known velocity u_{lid}. In this case f_6, f_{12}, f_{13}, f_{16} and $f_{17}$are unknown and the rest of PDF's are coming from inside the domain. The unknown PDF's are calculated as:

$$f_6 = f_5$$

$$f_{12} = f_{11} + \frac{1}{2}(f_3 - f_4 + f_7 - f_8 + f_{10} - f_9)$$

$$f_{13} = f_{14} - \frac{1}{2}(f_3 - f_4 + f_7 - f_8 + f_{10} - f_9) \quad \textbf{(6-34)}$$

$$f_{16} = f_{17} + \frac{1}{2}(f_1 - f_2 + f_9 - f_{10} + f_7 - f_8) - \frac{1}{2}\tilde{\rho}u_{lid}$$

$$f_{17} = f_{18} - \frac{1}{2}(f_1 - f_2 + f_9 - f_{10} + f_7 - f_8) + \frac{1}{2}\tilde{\rho}u_{lid}$$

$$\tilde{\rho} = f_0 + f_1 + f_2 + f_3 + f_4 + f_7 + f_8 + f_9 + f_{10} + 2(f_5 + f_{11} + f_{14} + f_{15} + f_{18})$$

Similar to the two dimensional simulation, we have used three temperature boundary conditions which are periodic, fixed temperature and fixed heat flux. For instance consider a fixed temperature of T_H and we want to apply this temperature to the bottom wall boundary in a D3Q19 lattice. In this case $g_5, g_{11}, g_{14}, g_{15}$, and g_{18}. are unknown and the rest of PDF's are coming from inside the domain. The unknown PDF's are calculated as:

$$g_5 = \frac{2}{3}(T_H - \tilde{T})$$

$$g_{11} = g_{14} = g_{15} = g_{18} = \frac{1}{12}(T_H - \tilde{T}) \qquad \textbf{(6-35)}$$

$$\tilde{T} = \sum_{k=0}^{4} g_k + \sum_{k=6}^{10} g_k + g_{12} + g_{13} + g_{16} + g_{17}$$

If we want to apply the fixed heat flux wall condition on the bottom wall, the fixed temperature in the Equation **(6-35)** should be replaced by the variable temperature T_w which depends on the temperature on the two nodes adjusted to the wall in the normal direction.

$$T_w = \frac{4T(I,J,2) - T(I,J,3) - 2Re.Pr.q_w}{3} \qquad \textbf{(6-36)}$$

Where, q_w is the applied heat flux to the wall (and it is zero for adiabatic wall condition), $T(I,J,2)$ and $T(I,J,3)$ are the temperature on the first and second nodes above the wall respectively at any wall node (I,J). The temperature on the wall is $T(I,J,1)$ which is equal to T_w.

The similar method can be adopted for any other boundary condition on the different boundary sides.

For the validation of the solver one case is presented in Figure 6-8 which is in good agreement with other CFD results (Jiang *et al.*, 1994).

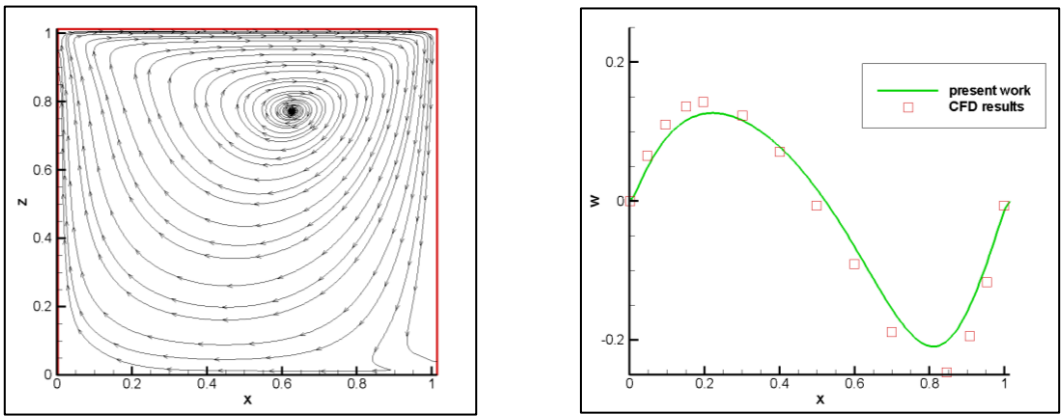

Figure 6-8 3D lid driven cavity simulation $Re = 100$: left) streamlines in the plane ($y = 0.5$), right) the z-direction velocity component variation with x in the centreline ($y = z = 0.5$)

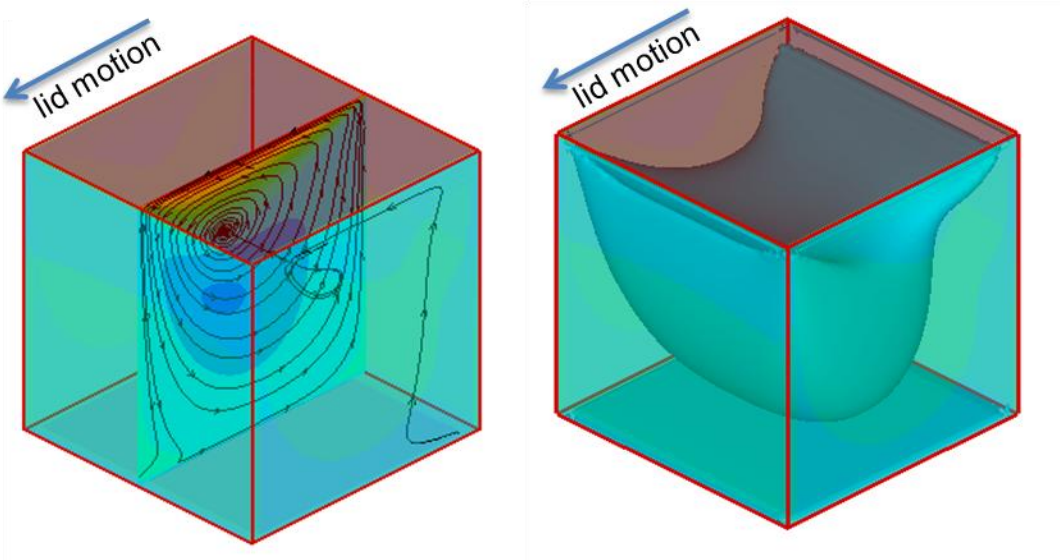

Figure 6-9 3D lid driven cavity simulation $Re = 100$, left) streamtraces on the middle plane perpendicular to the lid motion direction, right) isosurfaces of velocity component parallel to the lid motion

6.4 Solidification Modelling using LBM

It has been discussed that the solidification modelling and the sequential difficulties caused by the geometry modification, are one of the big challenges for icing codes developers. A new idea is developed to use LBM framework to model the solidification problem in icing. The lattice Boltzmann method has been used in different works to model the solidification and phase change for melting process and crystallization problems (Semma *et al*, 2007; Succi *et al*, 2002). In this section we are discussing different possible methods to model the solidification of the liquid water film in the icing problem.

To deal with the solidification problem we have to first perform the energy balance on the system in order to resolve where the phase change would happen. We have discussed in the previous sections the development of the two dimensional and three dimensional thermal lattice Boltzmann solvers and these solvers are used for the solidification modelling. The second part of solidification modelling is to consider the phase change problem from the liquid phase to the solid phase and its effect on the dynamics of the flow. One of the advantages of LBM is that this method can deal with the new solid particles without any need to modify the grid and geometry. The idea here in this work is to use a fixed grid approach and dynamically, the phase change zone is treated like a porous medium to consider the permeability of the phase changing material in the system.

The energy balance for an incompressible flow with phase change effects can be expresses mathematically as follows:

$$\frac{\partial T}{\partial t} + \vec{u}.\nabla T = \alpha_T \nabla^2 T - \frac{L}{c_p}\frac{\partial \varphi_L}{\partial t} \qquad \textbf{(6-37)}$$

Where, L is the latent heat of freezing of water, which is about $334\ kJ/kg$. The last term in this equation determines the effect of the solidification in the energy

balance of the system (here the water film). Equation **(6-37)** can be written in the non-dimensional form as:

$$\frac{\partial T}{\partial t} + \vec{u}.\nabla T = \frac{1}{RePr}\nabla^2 T - \frac{1}{St}\frac{\partial \varphi_L}{\partial t} \qquad \textbf{(6-38)}$$

Where $St = c_p \Delta T / L$ is the Stefan number and it characterizes the effect of the phase change in the energy balance of the system. The larger St the smaller is the effect of the phase change in the energy balance of the system. The temperature variation characteristic (ΔT) is usually the difference between the highest and lowest temperatures in the system. For instance in the water film solidification problem it can be the difference between the free-stream temperature and the cold surface temperature. It should be noticed that the phase change term in Equation **(6-38)** is an unsteady term and in order to keep the scheme fully explicit, this term is evaluated using the lag-values of the liquid fraction (φ_L).

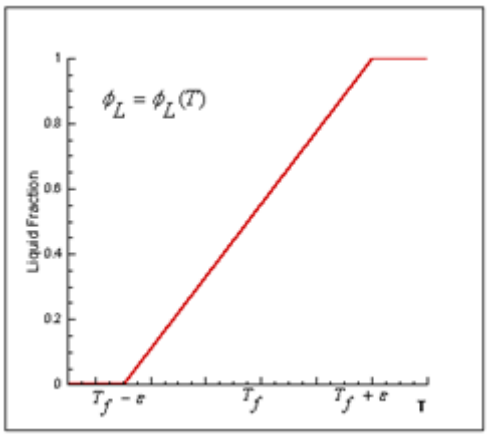

Figure 6-10 Variation of the liquid fraction around the freezing point for phase change consideration

The phase change process is considered to take place in a small range of temperature (typically about 5% of total temperature change in the system) around the freezing point (Semma *et al*, 2007). Figure 6-10 shows the linear variation which, is used in the current simulations, of liquid fraction around the freezing point.

In set of Equation **(6-39)** the details of calculations of hydrodynamics are given. These calculations are made for the liquid phase and the solid phase is considered as solid boundary. In fact, this model is updating the PDF's in such a way to apply an appropriate boundary condition on the phase changing material. When there is no phase change and ($\varphi_L = 1$) the set of Equation **(6-39)** is the same as standard update process of the PDF's which has been discussed in the previous sections. In the limit of the fully solidification when ($\varphi_L = 0$), these calculations are the same as the bounce-back boundary condition which is used to model the no-slip boundary assumption on the solid boundaries.

$$f_k^*(\vec{x} + \vec{e}_k, t) = f_k(\vec{x}, t)$$

$$f_k^{**}(\vec{x}, t+1) = f_k^*(\vec{x}, t) - \frac{1}{\tau_f}\left[f_k(\vec{x}, t) - f_k^{eq}(\vec{x}, t)\right] \qquad \textbf{(6-39)}$$

$$f_k(\vec{x}, t+1) = f_k^{**}(\vec{x}, t+1) + (1 - \varphi_L)[f_{\bar{k}}^{**}(\vec{x} + \vec{e}_k, t+1) - f_k^{**}(\vec{x}, t+1)]$$

In these calculations the notation (k^-) refers to the opposite node of the node (k) in the lattice. For instance, in D2Q9 lattice the opposite node of the node number 1 is the node number 3. In the calculations of the **(6-39)** the three steps are:

- The first step is the streaming to model the convection of the flow
- The second part is to model the collision term (diffusion effects)
- The third step is to treat the phase changing material as a permeable media

An alternative way to model the solidification effect into the motion of the flow is to add an external force in the momentum equation. This term models the resistance of the solid phase against the flow of the liquid phase (Chatterjee, 2010). In Equation **(6-6)** the aforementioned external force can be modelled as:

$$\vec{S}_k = w_k = -w_k \frac{K_0}{\rho} \frac{(1-\varphi_L)^2}{\varphi_L^3 + \epsilon} \vec{u} \qquad \textbf{(6-40)}$$

Where K_0 is a large number in order of $10^8 \frac{kg}{s.m^3}$ and ϵ is a small number in order of 10^{-3} to avoid the denominator in Equation **(6-40)** getting zero in the solid phase limit when $\varphi_L = 0$. In the solid limit this external force acts as a strong resistant against the flow of the liquid to assure vanishing the flow velocity near the solid phase. On the other hand in the liquid limit this term is vanishing and does not affect the motion of the liquid phase. However, this method includes some stability problem as it deals with large variation in this term with about 11 order of magnitude changes in the absolute value of $\vec{S}$.

6.5 Preliminary Results and Discussion

In this section we try to show the capability of the LBM to simulate the solidification process in icing problem. Consider a cavity flow problem with Reynolds number of 100. This Reynolds number is in the upper range of the typical Reynolds number of the thin liquid water film in the icing problems.The solution of flow for this problem using LBM is shown in Figure 6-11. To test the capability of the solver to model the flow around the complex solid particles distribution, a random set of solid particles are added in the cavity in the middle of the solution procedure. Figure 6-12 shows one set of random solid particles distribution. This can model the solidification process in the real condition when a part of moving water becomes solid. No numerical instability was found until the steady state solution was achieved. Figure 6-13 shows the steady state flow solution for Reynolds number of 100 with random solid particles distribution.

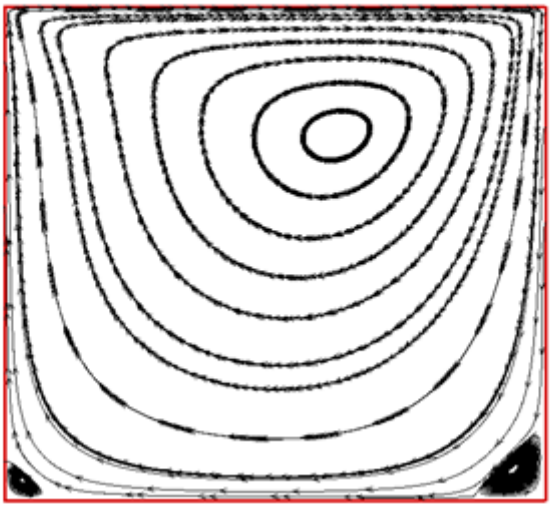

Figure 6-11 Cavity problem solution by LBM, Re=100, grid 128x128

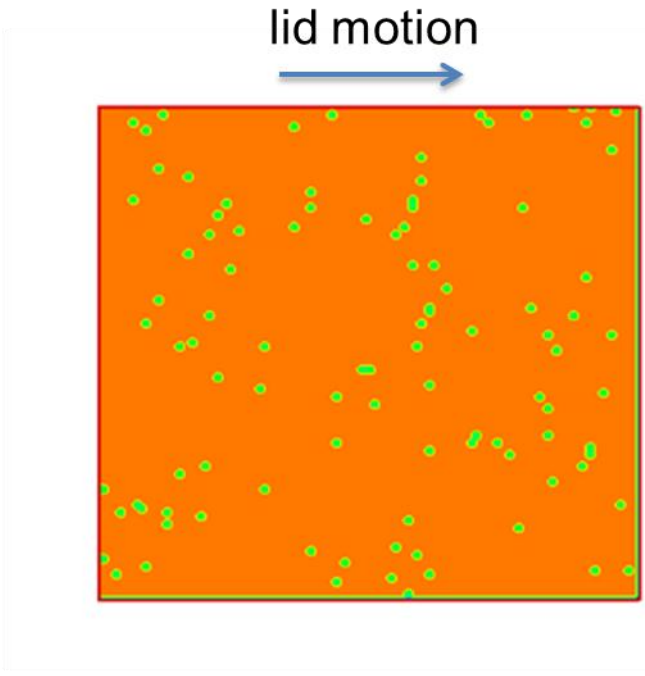

Figure 6-12 Plan view of random fixed solid particles distribution to simulate the solidification problem

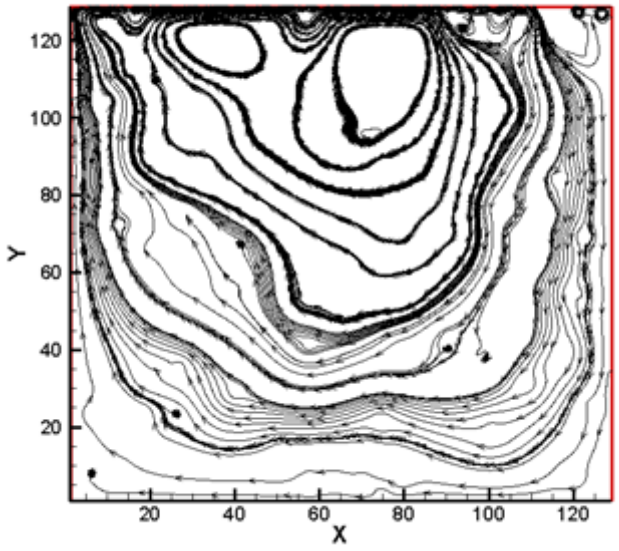

Figure 6-13 Solution of cavity problem in presence of solid particles, Re=100, grid 128x128

There are two important points regarding this simulation:

- The flow solver was able to simulate the small eddies around the solid particles even though a relatively coarse grid has been used in the simulation.
- The solver was able to deal with mass conservation problem caused by the phase change (from liquid to solid) which is one of the concerns in the solidification modelling.

The preliminary results obtained here show some of the capabilities of LBM to deal with the solidification problem and more work needs to be done to show other promises of the LBM to model the whole icing problem. However much work, which is based on the LBM, has suggested the outstanding capabilities of the lattice Boltzmann method in dealing with:

- Turbulent aerodynamic modelling around wing sections (Li *et al.*, 2005)
- Droplet dynamics and impact into water film and on the dry surfaces (Mukherjee and Abraham, 2007; Sehgal *et al.*, 1999)

- Air-water flows interaction and dealing with simulation of both flows simultaneously (Lee and Lin, 2005; Inamuro *et al.*, 2004)
- Thermal and heat transfer modelling of flows
- Solidification/melting and crystallization modelling

All of these aspects are related directly to the aircraft icing modelling (chapter one) and the last two were explored in this chapter. Based on these works, which have been done on different related aspects to icing, and also the preliminary results obtained from the simulations of the current research, we believe that the LBM can be an appropriate framework to model the aircraft icing problem at the finer scale. The three dimensional cases must be studied as they can show the capabilities of the LBM to handle the motion of the surface of the water film and also its waviness. The information on the velocity of the water film and the wave pattern of its surface come from the experimental data presented in chapter two.

7 Conclusion Remarks and Recommendations

7.1 Conclusions of the Work

In choosing to make an allowance for water splashed off from an icing surface in an icing model we can distinguish two approaches. The first approach is to evaluate those factors likely to affect the level or water loss by splash and find a suitable term for the mediating factor and to demonstrate that, perhaps with some factoring, it produces results similar to experiment. This mediating factor may then be integrated into existing icing codes with minimal re-writing and re-validation. Further add-ons can be created to deal with the breakup of splashed droplets and their fate.

The second approach is to resolve the processes at a finer scale so that the interaction may be treated more fully. Specifically, for us, that the water layer becomes an integral part of the ice modelling process, having a local thickness value which can be used as an input for the prediction of the amount of water which will be splashed off. In this investigation, we have aimed to take the second approach but also to package the findings into the form of a splash mediating factor which can be used in existing codes in accordance with the first approach.

Using existing facilities and code, we have worked on the link between corona shape, jet speed, droplet impact conditions, aerodynamic forcing and water film nature and thickness to develop a splashed volume indicator. Further, we propose a framework for modelling water percolation over an icing surface which might become a stepping stone for an icing prediction code which explicitly treats droplet impact, splash, ligament breakup, transport and re-impingement. Such a code might ultimately be expected to rely less on adjustment factors and be applicable to a wide range of scales, speeds, geometries, aerodynamic loads, surface types and droplet sizes.

In this work we have proposed a framework to model the splashing process using a semi-empirical approach. In this model, we have combined both the

experimental and observation data with numerical modelling of the splashing process. The experimental work has been undertaken at Cranfield University Icing facilities. In the conclusion of the experiments:

- Water film continuity is dependent on droplet impact and cloud conditions, becoming discontinuous in low liquid water concentrations.
- Water film velocity is measured and presented using a set of dimensionless parameters.
- The time taken for air flow effects to begin to take over from the early phases of a droplet impact is of the order of the time taken for the droplet to move through 50 times its own diameter (with droplet speed and air speed matched).
- Our experiments have been mostly possible at LWC values within the range found in natural icing conditions.

The numerical modelling had been tested and proven to have a good agreement with the experimental data, in the previous research which had been undertaken at Cranfield University on this subject. The key point and related results from the aforementioned work are as follows:

- Good agreement between the proposed numerical modelling and the experimental data
- The effect of the water film thickness on the splashing features in the SLD conditions

We have developed a semi-empirical method to estimate the water film thickness based on the experimental results of the water film velocity and analytical approach to balance the forces on the water film. The results of the VOF numerical modelling depends on the relative water film size (the ratio of water film thickness to droplet size) and the impact angle of the incoming droplet. This model considers the flow as an inviscid flow with moving interface between the different phases. Parametric correlations are offered to relate the splashed mass and the jets directions and velocities to the relative sizes of droplets and the film thickness they collide with and the impact angle.

The proposed model is limited to the wet impact and it is not valid for the dry impact. The numerical simulation should be performed for very low relative

water film thickness to model the condition of the dry impact. The model does not take in account the threshold of the splashing. However, we checked the validity of the model used in LEWICE code and it seems valid for the range of our experiments. Another important point is that this model is only valid when we consider the re-impingement effects otherwise it could lead to much less ice accretion compared to the real conditions. The size of the secondary droplet size is a key point in the re-impingement calculations and it has not been studied in this work. In our proposed model we have adopted the results and findings of the other members of the EXTICE project.

When the structure of the typical existing SLD models is compared with our proposed model we can notice the following points:

- Although the models address the splashing threshold from different aspects, both models indicate that in the typical SLD icing problem, splashing is taking place for droplets of size of $100\mu m$ and larger.
- In the existing models splashing characteristics are only dependant on the incoming droplet velocity and size while in the proposed model we try to relate the splashing characteristics not only to the incoming droplet velocity and size but on the surrounding airflow field and the presence of the liquid water film.
- In these models the splashing is taking place in one singular point, which is in clear contradiction with the observations of the splashing in the icing tunnel. In our proposed model, we defined geometry for the corona (base width, top width and height) and this allows as modelling the splashing in more realistic manner.
- As a result from the observations and the modelling we have characterized the secondary droplets with two ejected jets, while in the existing models model the secondary droplets are generally modelled with a single jet.
- The upper limit of the splashed mass in the existing splash models is about 15%-20% of the incoming droplet mass. In our model this ratio can be up to 90% in some cases of the large droplets and high velocity

impact near the stagnation zone. However, it should be noticed that our model it can be valid only if the re-impingement is taken in account. Generally the SLD models overestimate the collection efficiency (and subsequently the ice thickness) near the stagnation zone especially in the glaze regime. We believe that the type of SLD model, which take into account the local airflow condition, have the potential to deal with this problem. This should be investigated in more detail in the future works when the proposed model is implemented in icing codes.

Anticipating that further attention is required to model the percolation of a water film through ice roughness and in preparation for the modelling of more of the fluid, fluid-gas and fluid-solid interactions at the droplet impact time and length scales, work has begun on a multiphase model using a Lattice Boltzmann approach. The approach greatly simplifies the numerical problems of modelling large domains and complex interactions by restricting movements to steps in a limited number of directions. A solver has been developed which can solve momentum, heat and mass balances for two dimensional problems and has the capability of modelling the flow motion for the three dimensional problems. Further developments are needed to model the solidification process for three dimensional problems. The solution framework permits new solid particles to be introduced within an existing mesh, creating a new opportunity to handle the modelling of the phase change. Preliminary results show that Lattice Boltzmann method offers promise for modelling the fine scale flow and heat transfer elements of icing.

7.2 Recommendations for Future Works

We recommend the following for the future work and completion of the current research:

- We suggest the use of other type of targets in term of the geometry and the surface material. The airfoil-like targets could represent more realistic the aerodynamic forces on the water film. A scaling study might be helpful to generalize the experimental results. The observation showed a significant effect of the surface condition (in term of hydrophilicity and hydrophobicity) on the water film characteristics. More experimental work is suggested to characterize the water film for the widely used materials for the aircraft surfaces.

- We recommend the experimental study of the water film characteristics on the iced surfaces. There are difficulties associated with the imaging techniques that might be used to study the dynamics of the water film.

- The proposed methodology in this work should be tested and assessed when it is integrated in the icing codes in order to predict the ice shapes in the SLD conditions.

- Study the different methods, which have been described in chapter six, to model the effect of the solidification in the dynamics of the liquid water film.

- We finally recommend developing an icing codes based on the lattice Boltzmann method.

References and Bibliography

Airplane and Engine Certification Requirements in Supercooled Large Drop, Mixed Phase, and Ice Crystal Icing Conditions, (2010), FAA–2010–0636.

Aircraft Accident Report: In-Flight Icing Encounter And Loss Of Control, Simmons Airlines, (ATR) Model 72-212, N401am Roselawn, Indiana October 31, 1994, (1996), PB96-91040I, NTSB.

Ice Accretion Simulation, (1997), AGARD-AR-344.

Aircraft Icing Handbook, (2000), Civil Aviation Authority of New Zealand.

Collection Efficiency for Icing Analysis, (2001), EX156, Fluent.

Freezing Contamination: Aircraft Icing, (2005), Metro France and World Meteorological Organization (WMO) , TET1 aircraft icing 12/2005-V1.

Ice Accretion Simulation Evaluation Test, (2001), RTO-TR-038, RTO of NATO.

Icing Design Envelopes (14 CFR Parts 25 and 29, Appendix C) Converted to a Distance-Based Format, (2002), DOT/FAA/AR-00/30, FAA.

Addy, H. (2000), *Ice Accretion and Icing Effects for Modern Airfoils,* NASA/TP-2000-210031.

Al-Khalil, K. M. (1991), *Numerical Simulation of an Aircraft Anti-icing System Incorporating a Rivulet Model for the Runback Water* (PhD thesis), University of Toledo.

Al-Khalil, K. M., Horvath, C., Miller, D. R. and Wright, W. B. (1997), “Validation of NASA Thermal Ice Protection Computer Codes. III - The Validation of ANTICE”, *AIAA Paper,* 1997-0051.

Al-Khalil, K. M., Keith, T. G. and Dewitt, K. J. (1992), "Modelling of Surface Water Behaviour on Ice Protected Aircraft Components", *International Journal for Numerical Methods in Heat and Fluid Flow,* vol. 2, pp. 555-571.

Al-Khalil, K. M., Keith, T. G. and Dewitt, K. J. (1992), "Numerical Modeling of Runback Water on Ice Protected Aircraft Surfaces", *The Fifth Symposium on Numerical and Physical Aspects of Aerodynamic Flows.*

Anderson, D. N. (2004), *Manual of Scaling Methods,* NASA/CR-2004-212875.

Anderson, D. N. and Feo, A. (2002), "Ice Accretion Scaling Using Water Film Thickness Parameters", *AIAA Paper,* 2002-0522.

Anderson, D. N., Hentschel, D. B. and Ruff, G. A. (1998), "Measurement and Correlation of Ice Accretion Roughness", *AIAA Paper,* 1998-0486.

Anderson, D. N. and Shin, J. (1997), "Characterization of Ice Roughness from Simulated Icing Encounters", *AIAA Paper,* 1997-0052.

Anderson, D. N. and Tsao, J. C. (2003), "Additional Results of Ice-Accretion Scaling at SLD Conditions", *AIAA Paper,* 2003–0390.

Anderson, D. N. and Tsao, J. C. (2005), *Overview of Icing Physics Relevant to Scaling,* NASA/CR-2005-213851.

Barakos, G., Mitsoulis, E. and Assimacopoulis, D. (1994), "Natural Convection Flow in Square Cavity revisited Laminar and Turbulent Models with Wall Function", *International Journal for Numerical Methods in Fluids,* vol. 18, pp. 695-719.

Beaugendre, H., Morency, F. and Habashi, W. G. (2002), "FENSAP-ICE: Roughness Effects on Ice Shape Prediction", *AIAA Paper*, 2003-1222.

Begum, R. and Abdul Basit, M. (2008), "Lattice Boltzmann Method and its Applications to Fluid Flow Problems", *European Journal of Scientific Research,* vol. 22, no. 2, pp. 216-231.

Berthoumieu, P. and Feuillebois, F. (2010), *Modelling of the Basic SLD physics, Setting up and perform basic experiments, D4WP2, EXTICE Project*

Berthoumieu, P. (2012), "Experimental Srudy of Supercooled Large Droplets Impact in an Icing Wind Tunnel", *AIAA Paper,* 2012-3130.

Bourgault, Y., Habashi, W. G., Dompierre, J. and Baruzzi, G. S. (1999), "A Finite Element Method Study of Eulerian Droplets Impingement Models", *International Journal for Numerical Methods in Fluids,* vol. 29, pp. 429-449.

Bragg, M. B., Broeren, A. P. and Blumenthal, L. A. (2005), "Iced-Airfoil Aerodynamics", *Progress in Aerospace Sciences,* vol. 41, pp. 323-362.

Brakel, T. W., Charpin, J. P. F. and Myers, T. G. (2007), "One-dimensional Ice Growth due to Incoming Supercooled Droplets Impacting on a Thin Conducting Substrate", *International Journal of Heat and Mass Transfer,* vol. 50, pp. 1694-1705.

Busch, G. T., Broeren, A. P. and Bragg, M. B. (2008), "Aerodynamic Simulation of a Horn-Ice Accretion on a Subscale Model", *Journal of Aircraft,* vol. 45, pp. 604-613.

Chatterjee, D. (2010), "Lattice Boltzmann Simulation of Incompressible Transport Phenomena in Macroscopic Solidification Processes", *Numerical Heat Transfer, Part B,* vol. 58, pp. 55-72.

Chatterjee, D. and Chakraborty, S. (2006), "A Hybrid Lattice Boltzmann Model for Solid–Liquid Phase Transition in Presence of Fluid Flow", *Physical Review A,* vol. 351, pp. 359-367.

Chi, X., Li, Y., Chen, H., Addy, H. E., Choo, Y. K. and Shih, T. I. (2005), "A Comparative Study Using CFD to Predict Iced Airfoil Aerodynamics", *AIAA 2005-1371.*

Chikatamarla, S. S. and Karlin, I. V. (2009), "Lattices for the lattice Boltzmann method", *Physical Review E,* vol. 79, no. 046701, pp. 1-18.

Clift, R., Grace, J. R. and Weber, M. E. (1978), *Bubbles, Drops and Particles,* Academic Press, New York.

Comyn, J. (1997), *Adhesion Science,* Royal Scocity of Chemistry, Cambridge.

Croce, G., De Candido, E., Habashi, W. G. and Aubé, M. (2008), "Numerical Simulation of Icing Roughness Growth", *5th. European Congress on Computational Methods in Applied Sciences and Engineering,* June 30-July 5, 2008.

D'Orazio, A. and Succi, S. (2004), "Simulating Two-dimensional Thermal Channel Flows by Means of a Lattice Boltzmann Method with New Boundary Conditions", *Future Generation Computer Systems,* vol. 20, pp. 935-944.

Da Silva, G. A. L., Silvares, O. D. M. and De Zerbini, E. J. G. J. (2007), "Numerical Simulation of Airfoil Thermal Anti-Ice Operation Part 1: Mathematical Modeling", *Journal of Aircraft,* vol. 44, pp. 627-634.

Da Silva, G. A. L., Silvares, O. D. M. and De Zerbini, E. J. G. J. (2007), "Numerical Simulation of Airfoil Thermal Anti-Ice Operation Part 2: Implementation and Results", *Journal of Aircraft,* vol. 44, pp. 635-641.

Dardis, O. and McCloskey, J. (1998), "Lattice Boltzmann Scheme with Real Numbered Solid Density for the Simulation of Flow in Porous Media", *Physical Review E,* vol. 57, no. 4, pp. 4834-4837.

Das, K. (2006), *Numerical Icing on Turbomachinery* (PhD thesis), University of Cincinnati.

Davis, S. H. (2001), *Theory of Solidification,* Cambridge University Press.

De Vahl Davis, G. (1983), "Natural Convection of Air in a Square Cavity a Benchmark Numerical Solution", *International Journal for Numerical Methods in Fluids,* vol. 3, pp. 249-264.

De Vahl Davis, G. and Jones, I. P. (1983), "Natural Convection in Square Cavity Comparison Exercise", *International Journal for Numerical Methods in Fluids,* vol. 3, pp. 227-248.

Decours, J. and Le Pape, A. (2006), "2D Iced Airfoils Aerodynamic Performance Measurements and Simulations", *ONERA: Tire a Part,* vol. 157.

Demirdzic, I., Lilek, Z. and Peric, M. (1992), "Fluid Flow and Heat Transfer Test Problems for Non-orthogonal Grids Bench-mark Solutions", *International Journal for Numerical Methods in Fluids,* vol. 15, pp. 329-354.

Dima, C. and Brandi, V. (2000), *Prediction of Ice Accretion on Airfoils using CIRA Multi-Ice Code,* NATO/RTO Workshop Ice Accretion Calculation.

Djenidi, L. (2006), "Lattice Boltzmann Simulation of Grid-generated Turbulence", *Journal of Fluid Mechanics,* vol. 552, pp. 13-35.

Djenidi, L. and Moghtaderi, B. (2006), "Numerical Investigation of Laminar Mixing in a Coaxial Microreactor", *Journal of Fluid Mechanics,* vol. 568, pp. 223-242.

El Ganaoui, M., Lamazouade, A., Bontoux, P. and Morvan, D. (2002), "Computational Solution for Fluid Flow under Solid-Liquid Phase Change Conditions", *Computers and Fluids,* vol. 31, pp. 539-556.

Feo, A., Rogles, F. and Urdiales, M. (1991), *The Measurment of Water Film Thickness on Airfoils in Heavy Rain Conditions using Conductance Sensors,* AGARD CP 496.

Fletcher, A. J. (1983), "Generating Exact Solutions of 2D Burgers' Equations", *International Journal for Numerical Methods in Fluids,* vol. 3, pp. 213-216.

Fortin, G., Ilinca, A., Laforte, J. L. and Brandi, V. (2004), "New Roughness Computation Method and Geometric Accretion Model for Airfoil Icing", *Journal of Aircraft.,* vol. 41, pp. 119-127.

Fortin, G., Laforte, J. L. and Ilinca, A. (2006), "Heat and Mass Transfer During Ice Accretion on Aircraft Wings with an Improved Roughness Model", *International Journal of Thermal Sciences,* vol. 45, pp. 595-606.

Gattringer, M. (2009), *Numerical Simulation of Drop Impact on Dry and Wetted Surfaces* (MSc thesis), Cranfield University.

Geller, S., Krafczyk, M., Tolke, J., Turek, S. and Hron, J. (2006), "Benchmark Computations Based on lattice-Boltzmann, Finite Element and Finite Volume Methods for Laminar Flows", *Computers and Fluids,* vol. 35, pp. 888-897.

Gent, R. W., Dart, N. P. and Cansdale, J. T. (2000), "Aircraft Icing", *Philosophical Transactions of the Royal Society A: Mathematical, Physical and Engineering Sciences,* vol. 358, pp. 2873-2911.

Gent, R. W., Ford, J. M., Moser, R. J. and Miller, D. (2003), "Results from SLD Mass Loss Tests in the ACT Luton Icing Research Wind Tunnel", *AIAA Paper*, 2003-389.

Ghia, U., Ghia, K. and Shin, C. A. (1982), "High-Resolutions for Incompressible Flow using the Navier-Stokes Equations and a Multigrid Method", *Journal of Computational Physics,* vol. 48, pp. 387-411.

Guo, Z., Shi, B. and Zheng, C. (2002), "A Coupled Lattice BGK Model for the Boussinesq Equations", *International Journal for Numerical Methods in Fluids,* vol. 39, pp. 325-342.

Guo, Z., Zheng, C., Shi, B. and Zhao, T. S. (2007), "Thermal Lattice Boltzmann Equation for Low Mach Number Flows Decoupling Model", *Physical Review E,* vol. 75, no. 036704, pp. 1-15.

Hammond, D. W. (2000), *Development of 3D Ice Accretion Modelling ICECREMO,* NATO/RTO Workshop Ice Accretion Calculation.

Hammond, D. W. (2005), *Investigation into Super cooled Large Droplet Splashing,* Commissioned by the CAA Contract 623.

Hansman, R. J. and Kirby, M. (1987), *Experimental Methodologies to Support Aircraft Icing Analysis,* NASA Report N87-27589.

Harireche, O., Verdin, P., Thompson, C. P. and Hammond, D. W. (2008), "Explicit Finite Volume Modeling of Aircraft Anti-Icing and De-Icing", *Journal of Aircraft,* vol. 45, pp. 1924-1936.

He, X., Chen, S. and Doolen, G. D. (1998), "A Novel Thermal Model for the Lattice Boltzmann Method in Incompressible Limit", *Journal of Computational Physics,* vol. 146, pp. 282-300.

Hedde, T. and Guffond, D. (1992), "Development of a Three-dimensional Icing Code - Comparison with Experimental Shapes", *AIAA Paper*, 1992-00416.

Henry, R. C., Guffond, D., Aschettino, S. and Duprat, G. (2001), "Characterization of Ice Roughness and Influence on Aerodynamic Performance of Simulated Ice Shape", *AIAA Paper*, 2001-0092.

Henry, R. C., Guffond, D., Bouveret, A. and Gardette, G. (1999), "Heat Transfer Coefficient Measurement on Iced Airfoil in a Small Icing Wind Tunnel", *AIAA Paper,* 1999-0372.

Hindmarsh, J. P., Russell, A. B. and Chen, X. D. (2003), "Experimental and Numerical Analysis of the Temperature Transition of a Suspended Freezing Water Droplet", *International Journal of Heat and Mass Transfer,* vol. 46, pp. 1199-1213.

Hirt, C. W. and Nichols, B. D. (1981), "Volume of fluid (VOF) method for the dynamics of free boundaries", *Journal of Computational Physics,* vol. 39, no. 1, pp. 201-225.

Hou, S., Zou, Q., Chen, S., Doolen, G. and Cogley, A. C. (1995), "Simulation of Cavity Flow by the Lattice Boltzmann Method", *Journal of Computational Physics,* vol. 118, pp. 329-347.

Howison, S. D., Ockendon, J. R., Oliver, J. M., Purvis, R. and Smith, F. T. (2005), "Droplet Impact on a Thin Fluid Layer", *Journal of Fluid Mechanics,* vol. 542, pp. 1-23.

Huber, C., Parmigiani, A., Chopard, B., Manga, M. and Bachmann, O. (2008), "Lattice Boltzmann Model for Melting with Natural Convection", *International Journal of Heat and Fluid Flow,* vol. 29, pp. 1469-1480.

Ide, R. F. (1999), *Comparison of Liquid Water Content Measurement Techniques in an Icing Wind Tunnel,* NASA/TM-1999-209643.

Inamuro, T., Ogata, T., Tajima, S. and Konishi, N. (2005), "A Lattice Boltzmann Method for Incompressible Two-Phase Flows with Large Density Differences", *Journal of Computational Physics,* vol. 206, pp. 16-47.

Jacobs, S., Hospers, J. and Hoeijmakers, H. (2008), "Numerical Simulation of Ice Accretion on Multiple-Element Airfoil Sections", *26th International Congress of the Aeronautical Sciences.*

Jia, W. and Qiu, H. (2003), "Experimental Investigation of Droplet Dynamics and Heat Transfer in Spray Cooling", *Experimental Thermal and Fluid Science,* vol. 27, pp. 829-838.

Jiang, B. N., Lin, T. L. and Povinelli, L. A. (1994), "Large-scale Computation of Incompressible Viscous Flow by Least-squares Finite Element Method", *Comput. Methods Appl. Mech. Eng.,* vol. 114, pp. 213.

Jiaung, W. S., Ho, J. R. and Kuo, C. P. (2001), "Lattice Boltzmann Method for the Heat Conduction Problem With Phase Change", *Numerical Heat Transfer, Part B,* vol. 39, pp. 167-187.

Kim, W., Hammitt, F. G., Blome, S. and Hamed, H. (1976), *Thin Shear Driven Water Film Wavelet Characteristics,* UMICH 014571-4-I.

Knezevici, D., R. J. Kind, R. J. and Oleskiw, M.,M. (2005), "Determination of Median Volume Diameter (MVD) and Liquid Water Content (LWC) by Multiple Rotating Cylinders", *AIAA Paper*, 2005-861.

Kollar, L. E. and Farzaneh, M. (2007), "Modeling the Evolution of Droplet Size Distribution in Two-Phase Flows", *International Journal of Multiphase Flow,* vol. 33, pp. 1255-1270.

Korner, C., Pohl, T., Rude, U., Thurey, N. and Zeiser, T. (2006), "Parallel Lattice Boltzmann Methods for CFD Applications", in Bruaset, A. M. and Tveito, A. (eds.) *Numerical Solution of Partial Differential Equations on Parallel Computers,* Springer, Berlin, pp. 439-466.

Kreeger, R. E., Vargas, M. and McClain, S. T. (2005), "Heat Transfer over Roughness Elements Larger than the Boundary Layer", *AIAA Paper,* 2005-5186.

Lallemand, P. and Luo, L. (2003), "Lattice Boltzmann Method for Moving Boundaries", *Journal of Computational Physics,* vol. 184, pp. 406-421.

Latt, J. (2007), *Hydrodynamic Limit of Lattice Boltzmann Equations* (PhD thesis), University of Geneva.

Latt, J. (2008)*, Choice of Units in Lattice Boltzmann Simulations*, available at: http://www.lbmethod.org.

Lee, T. and Lin, C. (2005), "A Stable Discretization of the Lattice Boltzmann Equation for Simulation of Incompressible Two-Phase Flows at High Density Ratio", *Journal of Computational Physics,* vol. 206, pp. 16-47.

Lemaitre, C., Hemon, P. and de Langre, E. (2007), "Thin water film around a cable subject to wind", *Journal of Wind Engineering and Industrial Aerodynamics,* vol. 95, no. 9, pp. 1259-1271.

Levinson, L. H. and Wright, W. B. (2008), "IceVal DatAssistant - An Interactive, Automated Icing Data Management System", *AIAA Paper,* 2008-443.

Li , X., Liu, Y., Xu, Y., Ye, M. and Wu, F. (2011), "Migration-collision Scheme of LBM for Heat Conduction Problems Involving Solidification", *Theoretical & Applied Mechanics Letters,* vol. 1, no. 022003, pp. 1-5.

Li, H., Roisman, I. and Tropea, C. (2009), *Physics of Supercooled Large Drops (SLD): Literature Review,* D1WP2, EXTICE Project.

Li, H., Roisman, I. and Tropea, C. (2012), *Experiments and Modeling of Splash,* D2WP2, EXTICE Project.

Li, Y., Shock, R., Zhang, R. and Chen, H. (2005), "Simulation of Flow over an Iced Airfoil by Using a Lattice-Boltzmann Method", *AIAA Paper,* 2005-1103.

Lockerby, D. A. and Reese, J. M. (2008), "On the Modelling of Isothermal Gas Flows at the Microscale", *Journal of Fluid Mechanics,* vol. 604, pp. 235-261.

Luxford, G. (2005), *Experimental and Modelling Investigation of the Deformation, Drag and Break-up of Drizzle Droplets Subjected to Strong Aerodynamic Forces in Relation to SLD Aircraft Icing* (PhD thesis), Cranfield University.

Martys, N. S., Hagedorn, J. G. and Devaney, J. E. *, Lattice Boltzmann Simulations of Single and Multi Component Flow in Porous Media*, available at: www.fire.nist.gov/bfrlpubs/build00/PDF/b00029.pdf.

McCann, D. W. (2005), "NNICE - A Neural Network Aircraft Icing Algorithm", *Environmental Modelling and Software,* vol. 20, pp. 1335-1342.

Medvedev, D. and Kassner, K. (2005), "Lattice-Boltzmann Scheme for Dendritic Growth in Presence of Convection", *Journal of Crystal Growth,* vol. 275, no. e, pp. 1495-1500.

Mei, R., Luo, L. and Shyy, W. (1999), "An Accurate Curved Boundary Treatment in the Lattice Boltzmann Method", *Journal of Computational Physics,* vol. 155, pp. 307-330.

Messinger, B. L. (1953), "Equilibrium Temperature of an Unheated Icing Surface as a Function of Air Speed", *Journal of the Aeronautical Sciences,* vol. 20, pp. 29-42.

Miller, D. M. (1970), *Investigation of Ice Accertion Characteristics of Hydrophobic Materials,* FAA-DS-70-11.

Miller, D. R., Potapczuk, M. G. and Bond, T. H. (2004), *Update on SLD Engineering Tools Development,* NASA/TM—2004-213072.

Miller, W. and Succi, S. (2002), "A Lattice Boltzmann Model for Anisotropic Crystal Growth from Melt", *Journal of Statistical Physics,* vol. 107, no. 1/2, pp. 173-186.

Mingione, G. (2007), *EXTICE (EXTrime ICing Environment) Project: Description of Work,* Seventh Framework Programme, Report 211927.

Mingione, G. and Barocco, M. (2002), *Flight in Icing Conditions Summary,* , DGaC, France.

Mitchell, S. L. and Myers, T. G. (2008), "Approximate Solution Methods for One-Dimensional Solidification From an Incoming Fluid", *Applied Mathematics and Computation,* vol. 202, pp. 311-326.

Mohamad, A. A. (2011), *Fundamentals and Engineering Applications with Computer Codes,* Springer, London.

Mukherjee, S. and Abraham, J. (2007), "Investigations of Drop Impact on Dry Walls with a Lattice Boltzmann Model", *Journal of Colloid and Interface Science,* vol. 312, pp. 341-354.

Mukherjee, S. and Abraham, J. (2007), "A Pressure Evolution Based Multi Relaxation Time High Density Ratio Two Phase Lattice Boltzmann Model", *Computers and Fluids,* vol. 36, pp. 1149-1158.

Mulholland, J. A., Srivastava, R. K., Ryan, J. V. and Wendt, J. (1988), "Influence of Droplet Spacing on Drag Coefficient in Non-evaporating, Monodisperse Streams", *Amer. Inst. Aeron. Astron. Journal,* vol. 26, pp. 1231-1237.

Mundo, C., Sommerfield, M. and Tropea, C. (1995), "Droplet-wall Collisions Experimental Studies of the Deformation and Breakup Process", *International Journal of Multiphase Flow,* vol. 21, no. 2, pp. 151-173.

Myers, T. G. (2001), "Extension to the Messinger Model for Aircraft Icing", *American Institute of Aeronautics and Astronautics Journal,* vol. 39, pp. 211-218.

Myers, T. G. and Charpin, J. P. F. (2004), "A Mathematical Model for Atmospheric Ice Accretion and Water Flow on a Cold Surface", *International Journal of Heat and Mass Transfer,* vol. 47, no. 25, pp. 5483-5500.

Myers, T. G., Charpin, J. P. F. and Chapman, S. J. (2002), "The Flow and Solidification of a Thin Fluid Film on an Arbitrary Three-Dimensional Surface", *Physics of Fluids,* vol. 14, pp. 2788-2804.

Myers, T. G., Charpin, J. P. F. and Thompson, C. P. (2002), "Slowly Accreting Ice Due to Supercooled Water Impacting on a Cold Surface", *Physics of Fluids,* vol. 14, pp. 240-257.

Myers, T. G. and Hammond, D. W. (1999), "Ice and Water Film Growth From Incoming Supercooled Droplets", *International Journal of Heat and Mass Transfer,* vol. 42, pp. 2233-2242.

Myers, T. G., Liang, H. X. and Wetton, B. (2004), "The Stability and Flow of a Rivulet Driven by Interfacial Shear and Gravity", *International Journal of Non-Linear Mechanics,* vol. 39, pp. 1239-1249.

Naterer, G. F. (2003), "Coupled Liquid Film and Solidified Layer Growth with Impinging Supercooled Droplets and Joule Heating", *International Journal of Heat and Fluid Flow,* vol. 24, pp. 223-235.

Papadakis, M. (2003), "General Effects of Large Droplet Dynamics on Ice Accretion Modeling", *AIAA Paper,* 2003-392.

Papadakis, M., Yeong, H., Wong, S., Vargas, M. and Potapczuk, M. (2002), "Aerodynamic Performance of a Swept Wing with Ice Accretions", *AIAA Paper,* 2003-0731.

Peng, G., Xi, H., Duncan, C. and Chou, S. (1999), "Finite Volume Scheme for the lattice Boltzmann Method on Unstructured Meshes", *Physical Review E,* vol. 59, no. 4, pp. 4675-4682.

Peng, Y., Shu, C. and Chew, Y. T. (2003), "A 3D Incompressible Thermal Lattice Boltzmann Model and its Application to Simulate Natural Convection In Cubic Cavity", *Journal of Computational Physics,* vol. 193, pp. 260-274.

Potapczuk, M. (2003), "Ice Mass Measurements Implications for the Ice Accretion Process", *AIAA Paper,* 2003-387.

Potapczuk, M. and Wright, W. B. (2006), "SLD Simulation Capabilities with LEWICE", *CFD Methods for SLD Simulation Workshop,* October 19-20, 2006.

Potapczuk, M. G. (1999), *A Review of NASA Lewis' Development Plans for Computational Simulation of Aircraft Icing, AIAA Paper,* 1999-0243.

Potapczuk, M. G. and Miller, D. (2006), "Numerical Simulation of Ice Shapes from a Bimodal Large Droplet Icing Cloud", *AIAA Paper*, 2006-462.

Potapczuk, M. G., Papadakis, M. J. and Vargas, M. (2002), "LEWICE Modeling of Swept Wing Ice Accretions", *AIAA Paper,* 2003-0730.

Purvis, R. and Smith, F. (2004), "Large Droplet Impact on Water Layers", *AIAA Paper,* 2004-0414.

Purvis, R. and Smith, F. T. (2004), "Air-Water Interactions Near Droplet Impact", *European Journal of Applied Mathematics,* vol. 15, pp. 853-871.

Purvis, R. and Smith, F. T. (2005), "Droplet Impact on Water Layers: Post-Impact Analysis and Computations", *Philosophical Transactions of the Royal Society A: Mathematical, Physical and Engineering Sciences,* vol. 363, pp. 1209-1221.

Quero, M. (2006), *Analytical and Experimental Investigation into the Thermal Aspects of Droplet Impingement* (PhD thesis), Cranfield University.

Quero, M., Hammond, D. W., Purvis, R. and Smith, F. T. (2006), "Analysis of Super-Cooled Water Droplet Impact on a Thin Water Layer and Ice Growth", *AIAA Paper,* 2006-0466.

Rahmati, A. R. and Ashrafizaadeh, M. (2009), "A Generalizied LBM for 3D Incomp Flow Simulation", *Journal for Applied Fluid Mechanics,* vol. 2, no. 1, pp. 71-95.

Raj, R., Prasad, A., Parida, P. R. and Mishra, S. C. (2006), "Analysis of Solidification of a Semitransparent Planar Layer Using LBM and Discrete Trasfer Method", *Numerical Heat Transfer, Part A,* vol. 49, pp. 279-299.

Robert, J. G. (1992), "Contact Angle, Wetting, and Adhesion: A Critical Review", *J. Adhesion Sci. Technol.,* vol. 6, pp. 1269-1302.

Rothmayer, A. (2002), "On the Creation of Ice Surface Roughness by Interfacial Instabilities", *AIAA Paper,* 2003-0972.

Rothmayer, A. (2003), "Scaling Laws for Water and Ice Layers on Airfoils", *AIAA Paper,* 2003-1217.

Rothmayer, A. P. (2006), "Stagnation Point Icing", *AIAA Paper,* 2006-1081.

Rothmayer, A. P. and Krakos, J. A. (2004), "Residual Droplet Impacts and Thin Film Dynamics", *AIAA Paper,* 2004-0057.

Rothmayer, A. P., Matheis, B. D. and Timoshin, S. N. (2002), "Thin Liquid Films Flowing Over External Aerodynamic Surfaces", *Journal of Engineering Mathematics,* vol. 42, pp. 341-357.

Ruff, G. A. and Berkowitz, B. M. (1990), *Users Manual LEWICE,* NASA CR-185129.

Rutkowski, A., Wright, W. B. and Potapczuk, M. G. (2003), "Numerical Study of Droplet Splashing and Re-impingement", *AIAA Paper,* 2003-388.

Sanjeev, A. (2008), *Computational Study of Surfactant-Induced Modification of Droplet Impact Dynamics and Heat Transfer on Hydrophobic and Hydrophilic Surfaces* (MSc thesis), University of Cincinnati.

Sawyer, M. L., Jeter, S. M. and Abdel-Khalik, S. (1997), "A Critical Heat Flux Correlation for Droplet Impact Cooling", *International Journal of Heat and Mass Transfer,* vol. 40, pp. 2123-2131.

Schlichting, H. and Gersten, K. (2000), *Boundary Layer Theory,* 8th Edition, Springer.

Schrader, M. E. (1992), *Modern Approches to Wettability Theory and Applications,* Plenum Press, New York.

Sehgal, B. R., Nourgaliev, R. R. and Dinh, T. N. (1999), "Numerical Simulation of Droplet Deformation and Break-up by Lattice Boltzmann Method", *Progress in Nuclear Energy,* vol. 34, no. 4, pp. 471-488.

Semma, E., El Ganaoui, M. and Bennacer, R. (2007), "Lattice Boltzmann Method for Melting Solidification Problems", *C. R. Mecanique,* vol. 335, pp. 295-303.

Semma, E., El Ganaoui, M., Bennacer, R. and Mohamad, A. A. (2008), "Investigation of Flows in Solidification by Using the Lattice Boltzmann Method", *International Journal of Thermal Sciences,* vol. 47, pp. 201-208.

Shin, J. (1994), "Characteristics of Surface Roughness Associated with Leading Edge Ice Accretion", *AIAA Paper,* 1994-0799.

Shin, J. and Bond, T. (1993), "Surface Roughness Due to Residual Ice in the Use of Low Power Deicing Systems", *UNITED STATES,* Vol. NASA-TM-105971; *AIAA Paper,* 1993-0031.

Smith, F. T. and Purvis, R. (2005), "Air Effects on Large Droplet Impact", *AIAA Paper,* 2005-5184.

Smyrnaios, D. S., Pelekasis, N. A. and Tsamopoulos, J. A. (2000), "Boundary Layer Flow of Air Past Solid Surfaces in the Presence of Rainfall", *Journal of Fluid Mechanics,* vol. 425, pp. 79-110.

Soufflet, Y. (2008), *Improvement of Runback Water Calculation and its Impact on Ice Prediction* (PhD thesis), Cranfield University.

Stanfield, R. (2008), *Infulence of Flight-Path Variability of Conditions Upon In-Flight Icing* (EngD thesis), Cranfield University.

Steuerangle, J., Roy, K. and Wright, D. (2008), *Aircraft Icing: Safety Advisor,* SA11-04/08 AOPA, Bruce Landsberg.

Strapp, J. W., Oldenburg, J., Ide, R., Lilie, L., Bacic, S., Vukovic, Z., Oleskiw, M., Miller, D., Emery, E. and Leone , G. (2003), "Wind Tunnel Measurements of the Response of Hot-Wire Liquid Water Content Instruments to Large Droplets", *Journal of Atmospheric and Oceanic Technology,* vol. 20, pp. 791-806.

Strub, M., Jabbour, O., Strub, F. and Bedecarrats, J. P. (2003), "Experimental Study and Modelling of the Crystallization of a Water Droplet", *International Journal of Refrigeration,* vol. 26, pp. 59-68.

Succi, S. (2001), *The Lattice Boltzmann Equation for Fluid Dynamics and Beyond,* Oxford University Press, Oxford.

Sukop, M. C. and Thorne, D. T. (2006), *Lattice Boltzmann Modelling: An Introduction for Geoscientists and Engineers,* Springer, Netherlands.

Tan, C. S. and Bartlett, P. G. (2003), "An Experimental Study of Droplet Break-Up Using A Wind Tunnel", *AIAA Paper,* 2003-391.

Tan, C. S. and Papadakis, M. (2005), "Droplet Breakup, Splashing and Re-Impingement on An Iced Airfoil", *AIAA Paper 2005-5185.*

Thomas, P. J. (1992), "On the Influence of the Basset History Force on the Motion of a Particle through a Fluid", *Physics of Fluids A,* vol. 4, no. 9, pp. 2090-2093.

Thorne, D. T. and Sukop, M. C. "Lattice Boltzmann model for the elder problem", *Developments in Water Science,* vol. 55, part 2, pp. 1549-1557.

Tsao, J. C. and Anderson, D. N. (2005), "Latest Developments in SLD Scaling", *AIAA Paper,* 2005-5187.

Tsao, J. C., Kreeger, R. E. and Feo, A. (2010), *Evaluation of the Water Film Weber Number in Glaze Icing Scaling,* NASA/TM—2010-216101.

Tsao, J. C. (2002), "Cross Flow Effects on Glaze Ice Roughness Formation (on swept wing leading edge)", *AIAA Paper,* 2003-1219.

Tsao, J. C. and Rothmayer, A. P. (2002), "Application of Triple-Deck Theory to the Prediction of Glaze Ice Roughness Formation on an Airfoil Leading Edge", *Computers and Fluids,* vol. 31, pp. 977-1014.

Van Driest, E. R. (1956), "On Turbulent Flow near a Wall", *Journal of the Aeronautical Sciences,* vol. 23, pp. 1007-1011.

Vargas, M. (2005), "Current Experimental Basis for Modeling Ice Accretions on Swept Wings", *AIAA Paper,* 2005-5188.

Vargas, M. (2007), "Current Experimental Basis for Modeling Ice Accretions on Swept Wings", *Journal of Aircraft,* vol. 44, pp. 274-290.

Vargas, M. and Tsao, J. C. (2007), "Observations on the Growth of Roughness Elements into Icing Feathers", *AIAA Paper,* 2007-900.

Vargas, M. and Tsao, J. C. (2008), "Time-Sequence Observations of the Formation of Ice Accretions on Swept Wings", *AIAA Paper,* 2008-470.

Verdin, P. (2007), *An Automatic Multi-stepping Approach to Aircraft Ice Prediction* (PhD thesis), Cranfield University.

Viggen, E., M. (2009), *The Lattice Boltzmann Method with Applications in Acoustics* (MSc thesis), Norwegian University of Science and Technology.

Voller, V. R. and Prakash, C. (1987), "A Fixed Grid Numerical Modelling Methodology for Convection-diffusion Mushy Region Phase-change Problems", *International Journal of Heat and Mass Transfer,* vol. 30, no. 8, pp. 1709-1719.

Walsh, S. D. C., Burwinkle, H. and Saar, M. O. (2009), "A New Partial-Bounceback Lattice Boltzmann Method for Fluid Flow Through Heterogeneous Media", *Computers & Geosciences,* vol. 35, pp. 1186-1193.

Wang, J., Wang, M. and Li, Z. (2007), "A lattice Boltzmann Algorithm for Fuid–Solid Conjugate Heat Transfer", *International Journal of Thermal Sciences,* vol. 46, pp. 228-234.

Wang, X. (2008), *Convective Heat Transfer and Experimental Icing Aerodynamics of Wind Turbine Blades* (PhD thesis), University of Manitoba.

Wang, G. and Rothmayer, A. P. (2005), "Air Driven Water Flow Past Small Scale Surface Roughness", *AIAA Paper,* 2005-0653.

Wang, G. and Rothmayer, A. P. (2009), "Thin Water Films Driven by Air Shear Stress Through Roughness", *Computers and Fluids,* vol. 38, pp. 235-246.

Wanger, A. J. (2008), *A Practical Introduction to the Lattice Boltzmann Method*, available at: http://www.physics.ndsu.nodak.edu/wagner/LB.html.

Weinstein, L. M. (1988) *Liquid Thickness Gauge.* The United States of America as represented by the Administrator of the National Aeronautics and Space Administration, Washington, D.C. Patent no. 4,765,187.

Whalen, E. A., Broeren, A. P. and Bragg, M. B. (2008), "Aerodynamics of Scaled Runback Ice Accretions", *Journal of Aircraft,* vol. 45, pp. 591-603.

Whalen, E. A., Broeren, A. P., Bragg, M. B. and Lee, S. (2005), "Characteristics of Runback Ice Accretions on Airfoils and their Aerodynamic Effects", *AIAA Paper,* 2005-1065.

Wilcox, D. C. (2006), *Turbulence Modeling for CFD,* D C W Industries.

Wolf Gladrow, D. A. (2005), *Lattice-Gas Cellular Automata and Lattice Boltzmann Models,* Springer, Berlin.

Wright, W. B. (1993), "Advancements in the LEWICE Ice Accretion Model", *AIAA Paper,* 1993-0171.

Wright, W. B. (1998), *A Summary of Validation Results for LEWICE 2.0,* NASA/CR-1998-208687.

Wright, W. B. (2002), *User Manual LEWICE Version 2.2.2,* NASA/CR-2002-211793.

Wright, W. B. (2005), "Validation Results for LEWICE 3.0", *AIAA Paper,* 2005-1243.

Wright, W. B. and Bidwell, C. S. (1995), "Additional Improvements to the NASA Lewis Ice Accretion Code LEWICE", *AIAA Paper,* 1995-0752.

Wright, W. B. and Potapczuk, M. G. (2004), "Semi-Empirical Modeling of SLD Physics", *AIAA Paper,* 2004-412.

Wright, W. B., Potapczuk, M. G. and Levinson, L. H. (2008), "Comparison of LEWICE and GlennICE in the SLD Regime", *AIAA Paper,* 2008-439.

Yoon, S. S., DesJardin, P. E., Presser, C., Hewson, J. C. and Avedisian, C. T. (2006), "Numerical Modeling and Experimental Measurements of Water Spray Impact and Transport Over a Cylinder", *International Journal of Multiphase Flow,* vol. 32, pp. 132-157.

Yuan, P. (2005), *Thermal Lattice Boltzmann Two-Phase Flow Model for Fluid Dynamics* (PhD thesis), University of Pittsburgh.

Zhang, X. (2007), *Surface Classification from Aicraft Icing Droplet Splsh Images* (MSc thesis), Cranfield University.

Zhao Yu, B. S. (2009), *A Novel Lattice Boltzmann Method for Direct Numerical Simulation of Multiphase Flows* (PhD thesis), The Ohio State University.

Zhu, L., Tretheway, D., Petzold, L. and Meinhart, C. (2003), "Simulation of Fluid Slip at 3D Hydrophobic Microchannel Walls by the Lattice Boltzmann Method", *Journal of Computational Physics,* vol. 202, pp. 181-195.

APPENDICES

Appendix A Commercial Aircraft Icing Regulations[1]

Appendix C of FAA FAR Part 25

This Appendix C of 14 CFR Part 25 has been in use since 1964 for selecting values of icing-related cloud variables for the design of in-flight ice protection systems for aircraft. Figure A-1, Figure A-2 and Figure A-3 are known as .continuous maximum conditions and they represent a portion of stratiform icing conditions or layer-type clouds that, in 1964, were considered to be important for the design of thermal ice protection systems on large airplanes. Figure A-4, Figure A-5 and Figure A-6 are known as .intermittent maximum conditions, and they represent a portion of convective, or cumuliform, clouds and icing conditions. Traditionally, continuous maximum conditions have been applied to airframe ice protection and intermittent maximum conditions have been applied to engine ice protection. These are design envelopes as opposed to more complete scientific .characterizations. The former contain only those ranges of variables that are thought to be important for the design of aircraft ice protection systems. A complete characterization will require a wider range of variables and values. Figure A-1 and Figure A-4 are supposed to indicate the probable maximum (99%) value of liquid water content (LWC) that is to be expected as an average over a specified reference distance, for a given temperature and representative droplet size in the cloud. For Figure A-1 this reference or standard distance is 20 statute miles (17.4 nmi) in stratiform icing conditions, and for Figure A-4, it is 3 statute miles (2.6 nmi) in convective icing conditions. These are arbitrary reference distances but were convenient for the original National Advisory Committee for Aeronautics (NACA) researchers in the late 1940s because most of their rotating cylinder measurements were averages over approximately 10 and 3 miles, respectively. These probable maximum

[1] The major part of this section is directly cited from FAA Icing Regulations documents.

values of LWC were estimated by the NACA and Weather Bureau researchers in the early 1950s when they first formulated the basis for the present-day Appendix C.

In these icing applications, the actual droplet size distribution (typically 1-30 μm) in clouds is represented by a single variable called the droplet median volume diameter (MVD) or, in the older usage, an approximately equivalent variable called the mean effective diameter (MED). The MVD is the midpoint of the LWC distribution over the range of cloud droplet sizes that happen to be present at the time. The MVD therefore varies with the number of droplets in each size category, but the overall average for layer clouds is about 15 μm while for convective clouds it is about 19 μm. The MVD has proven useful as a simple substitute for the actual droplet size distributions in ice accretion computations.

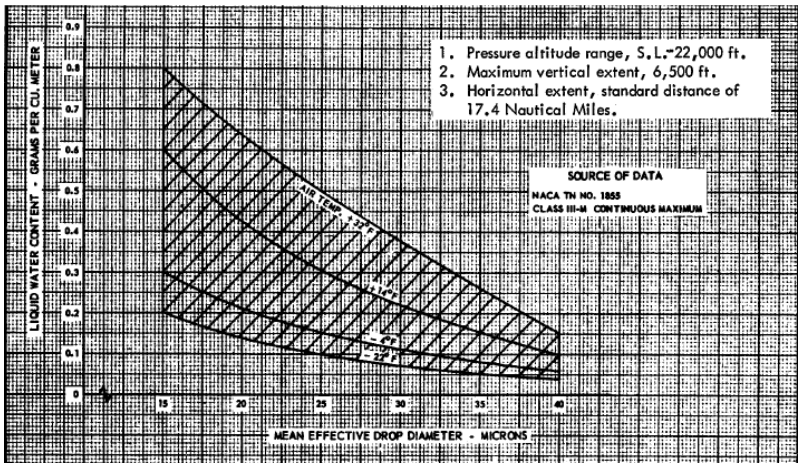

Figure A-1 Continuous maximum (stratiform clouds) atmospheric icing conditions (Liquid water content versus mean effective drop diameter)

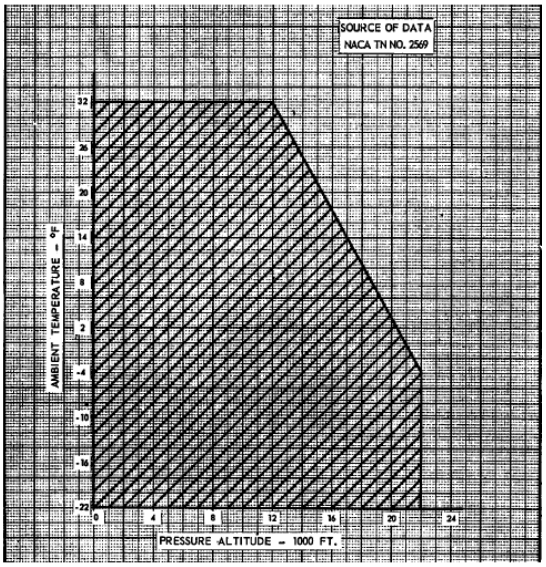

Figure A-2 Continuous maximum (stratiform clouds) atmospheric icing conditions (ambient temperature versus pressure altitude)

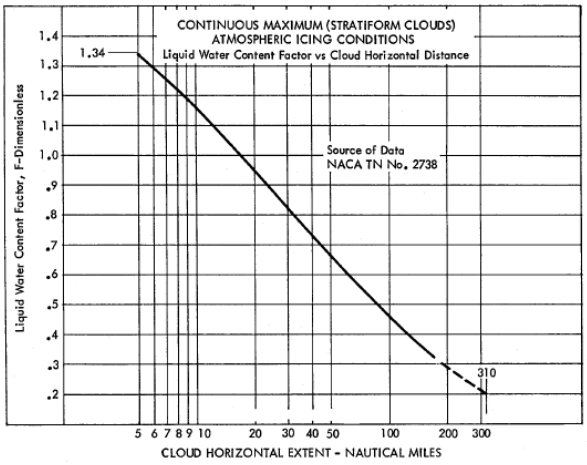

Figure A-3 Continuous maximum (stratiform clouds) atmospheric icing conditions (liquid water content factor versus cloud horizontal extent)

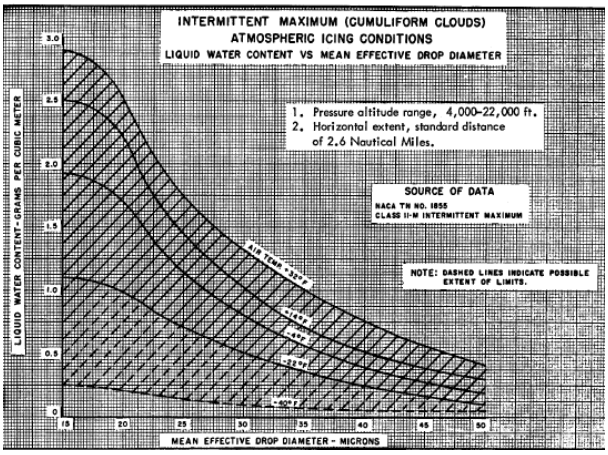

Figure A-4 Intermittent maximum (cumuliform clouds) atmospheric icing conditions (liquid water content versus mean effective drop diameter)

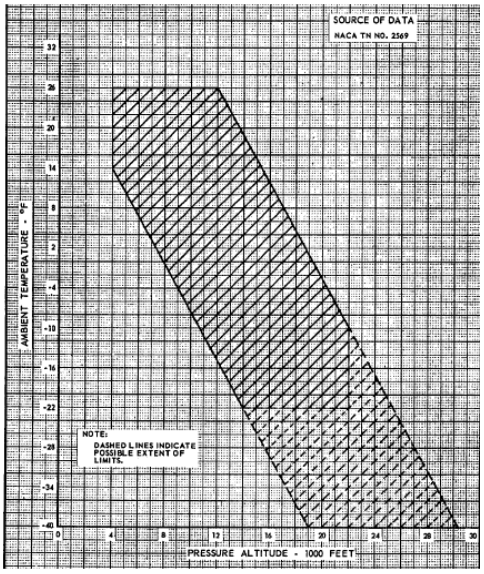

Figure A-5 Intermittent maximum (cumuliform clouds) atmospheric icing conditions (ambient temperature versus pressure altitude)

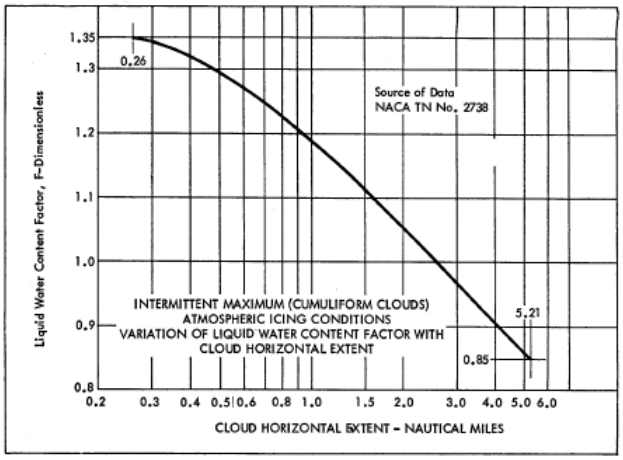

Figure A-6 Intermittent maximum (cumuliform clouds) atmospheric icing conditions (variation of liquid water content factor with cloud horizontal extent)

Appendix O of FAA FAR Part 25

In the 1990s, the FAA became aware that the types of icing conditions considered during the certification of transport category airplanes and turbine aircraft engines needed to be expanded to increase the level of safety during flight in icing. The FAA determined that the revised icing certification standards should include supercooled large drops (SLD), mixed phase, and ice crystals. Safety concerns about the adequacy of the icing certification standards were brought to the forefront of public and governmental attention by a 1994 accident in Roselawn, Indiana, involving an Avions de Transport Regional ATR 72 series airplane. The FAA, Aerospatiale, the French Direction Ge´ne´ral de l'Aviation Civile, Bureau Enquete Accident, the National Aeronautics and Space Administration, the National Transportation Safety Board (NTSB), and others conducted an extensive investigation of this accident. These investigations led to the conclusion that freezing drizzle conditions created a ridge of ice on the wing's upper surface aft of the de-icing boots and forward of the ailerons. It was further concluded that this ridge of ice contributed to an un-commanded roll of the airplane. Based on its investigation, the NTSB recommended changes to the icing certification requirements. The certification requirements for icing conditions are specified in part 25, appendix C. The atmospheric condition

(freezing drizzle) that contributed to the Roselawn accident is currently outside the icing envelope for certifying transport category airplanes. The term “icing envelope” is used within part 25, appendix C, and this NPRM (Notice of Proposed Rule Making) to refer to the environmental icing conditions within which the airplane must be shown to be able to safely operate. The term ‘‘transport category airplanes’’ is used throughout this rulemaking document to include all airplanes type certificated to part 25 regulations. Another atmospheric icing condition that is currently outside the icing envelope is freezing rain. The FAA has not required airplane manufacturers to show that airplanes can operate safely in freezing drizzle or freezing rain conditions. These conditions constitute an icing environment known as supercooled large drops (SLDs). As a result of this accident and consistent with related NTSB recommendations the FAA tasked the Aviation Rulemaking Advisory Committee (ARAC), through its Ice Protection Harmonization Working Group (IPHWG), to do the following:

- Define an icing environment that includes SLDs.
- Consider the need to define a mixed phase icing environment (supercooled liquid and ice crystals).
- Devise requirements to assess the ability of an airplane to either safely operate without restrictions in SLD and mixed phase conditions or safely operate until it can exit these conditions.
- Study the effects icing requirement changes could have on Pilot compartment view; Airspeed indicating system; Static pressure systems.
- Consider the need for a regulation on ice protection for angle of attack probes.

Currently[1] the certification regulations applicable to transport category airplanes for flight in icing conditions require that: “The airplane must be able to operate safely in the continuous maximum and intermittent maximum icing conditions of appendix C”. The certification regulations also require minimum performance

[1] It is referred to the date of the FAA report publication in 2010.

and handling qualities in these icing conditions and methods to detect airframe icing and to activate and operate ice protection systems.

Icing regulations applicable to engines (part 33, 91 and 135 of the regulations) address limitations in icing conditions for airplanes operated under these parts. Part 121 (Operating Requirements: Domestic, Flag and Supplemental Operations) addresses operations in icing conditions that might adversely affect safety and requires installing certain types of ice protection equipment and wing illumination equipment. Some of the part 25 and 33 regulations specify that the affected equipment must be able to operate in some or all of the icing conditions defined in part 25, appendix C. Other regulations within these parts do not specify the icing conditions that must be considered for airplane certification, but, historically, airplane certification programs have only considered icing conditions that are defined in appendix C.

Appendix C addresses continuous maximum and intermittent maximum icing conditions within stratiform and cumuliform clouds ranging from sea level up to 30,000 feet. Appendix C defines icing cloud characteristics in terms of mean effective drop diameters, liquid water content, temperature, horizontal and vertical extent, and altitude. Icing conditions that contain drops with mean effective diameters that are larger than the cloud mean effective drop diameters defined in appendix C are typically referred to as freezing drizzle or freezing rain. Icing conditions containing freezing drizzle and freezing rain are not currently considered when certifying an airplane's ice protection systems. Because the larger diameter drops typically impinge farther aft on the airfoil, exposure to these conditions can result in ice accretions aft of the ice protection area, which can negatively affect airplane performance and handling qualities. Likewise, mixed phase (supercooled liquid and ice crystals) and 100% ice crystal icing conditions are not currently considered when certifying an airplane's ice protection systems. Exposing engines and externally mounted probes to these conditions could result in hazardous ice accumulations within the engine that may result in engine damage, power loss, and loss of or misleading airspeed indications. The certification regulations for transport

category airplanes and engines do not address the safe operation of airplanes in SLD, mixed phase, or ice crystal icing conditions and the operating rules do not specifically prohibit operations in these conditions.

The NTSB issued NTSB Safety Recommendation as a result of the Roselawn accident previously discussed. This rulemaking activity partially addresses the NTSB recommendations because there are separate rulemaking activities associated with revisions to 14 CFR part 23 regulations for small airplanes and 14 CFR part 121 operational regulations. The NTSB recommendations are as follows:

1. Revise the icing criteria published in 14 Code of Federal Regulations (CFR), parts 23 and 25, in light of both recent research into aircraft ice accretion under varying conditions of liquid water content, drop size distribution, and temperature, and recent developments in both the design and use of aircraft. Also, expand the appendix C icing certification envelope to include freezing drizzle/freezing rain and mixed water/ice crystal conditions, as necessary.
2. Revise the icing certification testing regulation to ensure that airplanes are properly tested for all conditions in which they are authorized to operate, or are otherwise shown to be capable of safe flight into such conditions. If safe operations cannot be demonstrated by the manufacturer, operational limitations should be imposed to prohibit flight in such conditions and flight crews should be provided with the means to positively determine when they are in icing conditions that exceed the limits for aircraft certification.

The ARAC's (Aviation Rulemaking Advisory Committee) Ice Protection Harmonization Working Group (IPHWG) submitted additional part 121 icing rulemaking recommendations to the FAA that may lead to future rulemaking, but do not directly impact this NPRM. Those recommendations would improve airplane safety when operating in icing conditions. The recommendations would:

- Address when ice protection systems must be activated.

- Require some airplanes to exit all icing conditions after encountering large drop icing conditions conducive to ice accretions aft of the airframe's protected area.

The following figures show the envelope which has been defined for freezing drizzle and freezing rain by FAA. Whenever is applicable, manufacturers must show that the airplane can operate safely in these conditions.

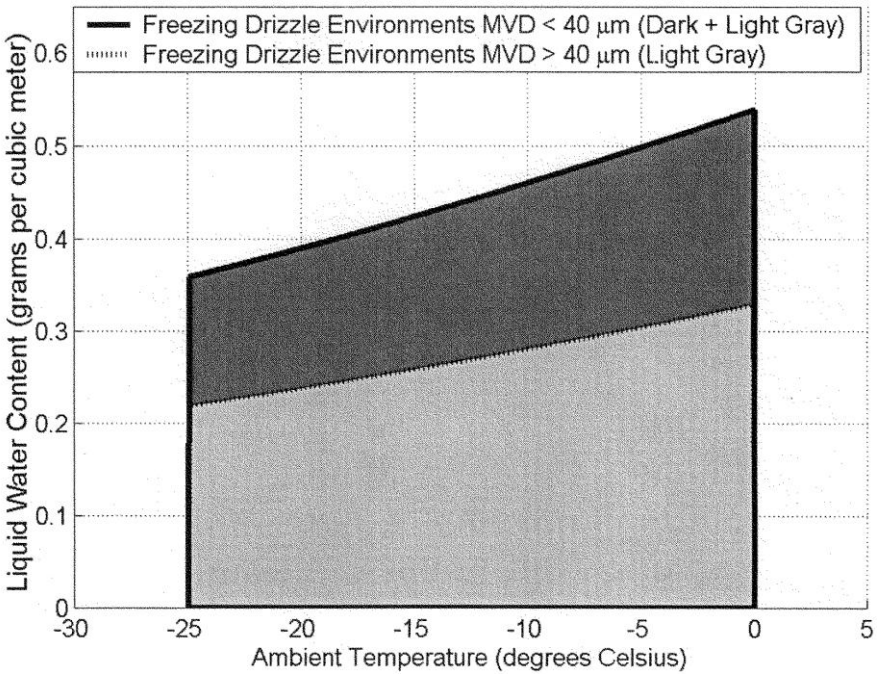

Figure A-7 Freezing drizzle envelope, LWC versus the ambient temperature

The envelope of freezing drizzle environment is defined in Figure A-7, Figure A-8 and Figure A-9 while the envelope of freezing rain environment is defined in Figure A-10, Figure A-11and Figure A-12. The environmental conditions in these envelopes are summarized in Table A-1

It should be noted that in SLD conditions the MVD of the clouds could be smaller or larger than 40μm although in both cases the clods will contain droplets with diameter larger than 40μm.

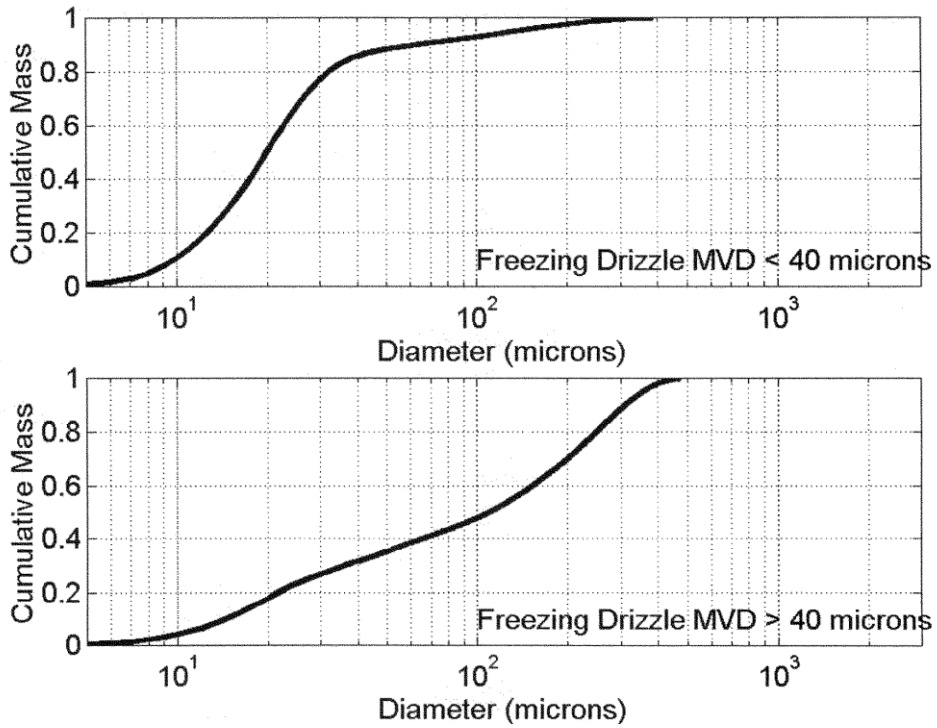

Figure A-8 Freezing drizzle, droplet diameter distribution

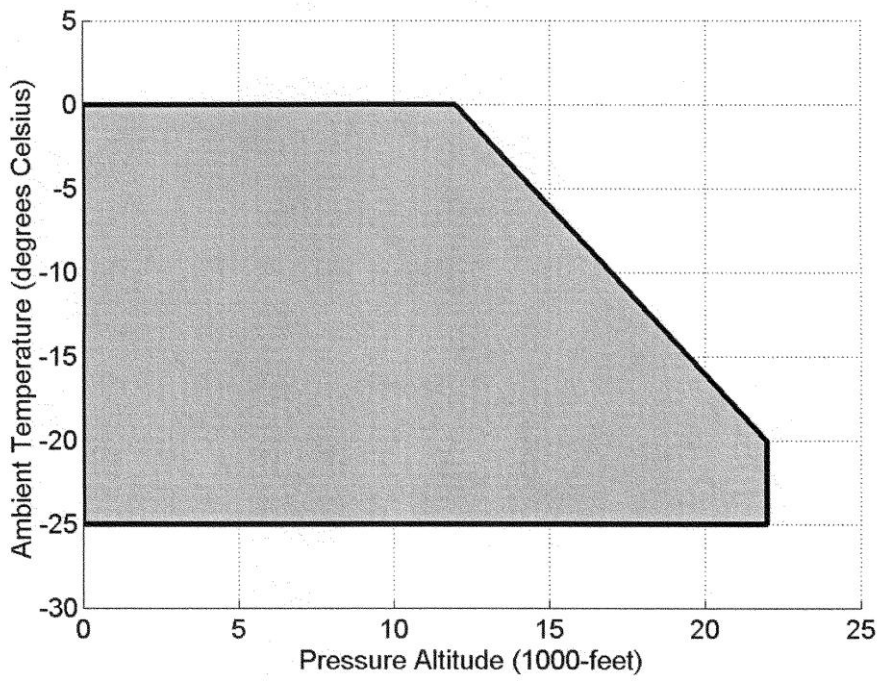

Figure A-9 Freezing drizzle envelope, ambient temperature versus pressure altitude

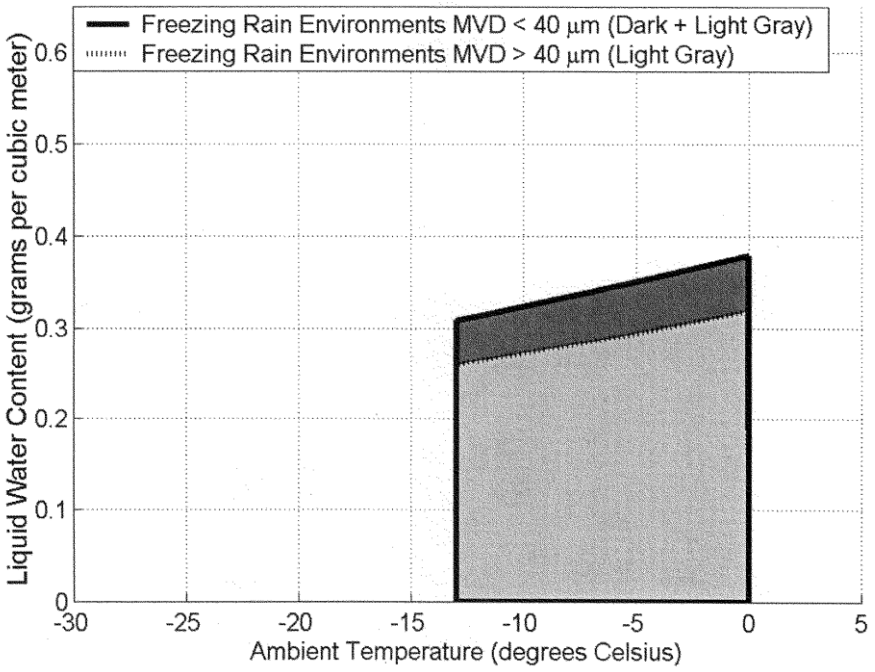

Figure A-10 Freezing rain envelope, LWC versus the ambient temperature

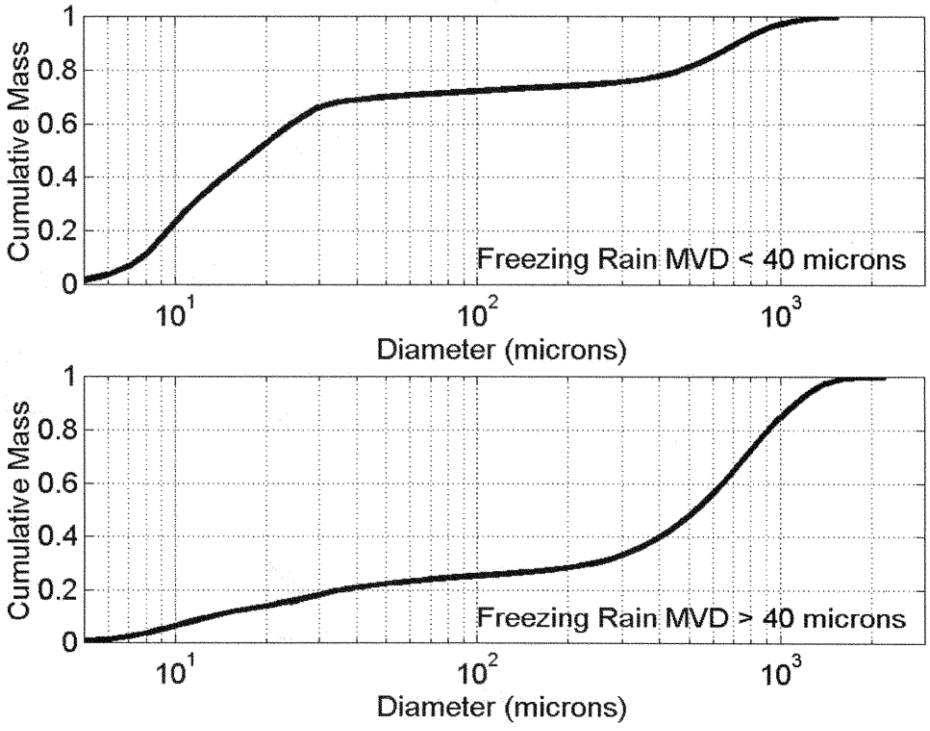

Figure A-11 Freezing rain, droplet diameter distribution

FIGURE 6 - Appendix O, Freezing Rain, Temperature and Altitude

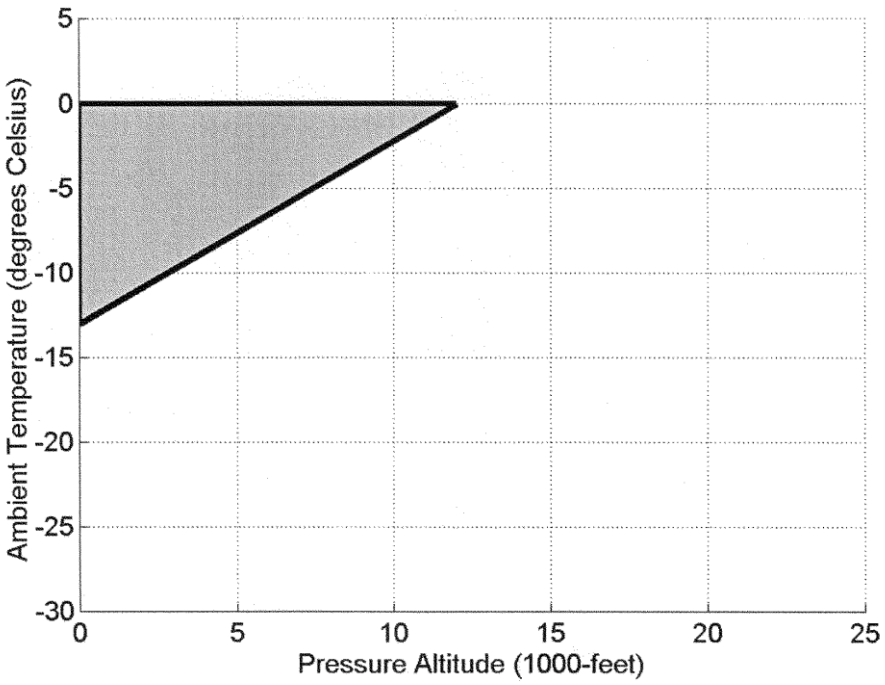

Figure A-12 Freezing rain envelope, ambient temperature versus pressure altitude

Table A-1 Comparison of environmental conditions for Appendix C and SLD icing envelopes.

	Appendix C, Stratiform clouds	Appendix C, Cumuliform clouds	Freezing Drizzle, MVD<40μm	Freezing Drizzle, MVD<4μmm	Freezing Rain, MVD<40μm	Freezing Rain, MVD<40μm
Max droplet size (μm)	40	50	400	500	1500	2200
LWC Range (g/m^3)	0.04-0.8	.05-2.93	0-0.53	0-0.53	0-0.38	0-0.38
Temperature Range (ºC)	-5 to 0	-40 to 0	-25 to 0	-25 to 0	-13 to 0	-13 to 0
Altitude Range (ft)	0-22,000	19,000-29,200	0-22,000	0-22,000	0-12.000	0-12,000

Appendix B Fluent setup for simulation of drop impact

The UDF (User Defined Function) has been used in Fluent to simulate the drop impact is given in this appendix. Three phases are defined for the simulation, which are the droplet, water film and surrounding air.

The UDF is as follows and should be compiled in Fluent and hooked before the initialization step.

```
/************************************************************************
UDF Initiallizing Volume Fraction and Velocity
************************************************************************/

/*-------definitions-------------------------------------------------------------------------------*/


#include "udf.h"

#define diam            0.0002                  /*drop diameter*/
#define h_film          0.0001                  /*film thickness*/
#define y_drop          0.00024                 /*initial drop height from the wall*/
#define x_drop          0.0                     /*initial drop distance from the left side*/
#define velocity_y      -1.0                    /*initial drop y-velocity*/
#define velocity_x      0                       /*initial drop x-velocity*/

/*-------drop velocity-----------------------------------------------------------------------------*/


DEFINE_INIT(init_drop_velocity, mixture_domain)
{

        int phase_domain_index;

        cell_t cell;

        Thread *cell_thread;

        Domain *subdomain;

        real xc[ND_ND];


        sub_domain_loop(subdomain, mixture_domain, phase_domain_index)

        {

                if (DOMAIN_ID(subdomain) == 2)


                        thread_loop_c (cell_thread,subdomain)

                                {


                                        begin_c_loop_all (cell,cell_thread)

                                                {
                                                        C_CENTROID(xc,cell,cell_thread);

                                                        if (sqrt(pow(xc[0] - x_drop,
2.)+pow(xc[1] - y_drop, 2.)) <= (diam/2.0))
```

```
                                                        C_V(cell,cell_thread) =
velocity_y;
                                                        C_U(cell,cell_thread) =
velocity_x;
                                                }
                                        end_c_loop_all (cell,cell_thread)
                                }
        }
}


/*------drop phase-------------------------------------------------------------------------*/

DEFINE_INIT(init_liquid_phase_drop, mixture_domain)
{
        int phase_domain_index;
        cell_t cell;

        Thread *cell_thread;
        Domain *subdomain;
        real xc[ND_ND];

        sub_domain_loop(subdomain, mixture_domain, phase_domain_index)
        {
                if (DOMAIN_ID(subdomain) == 2)

                        thread_loop_c(cell_thread,subdomain)
                                {

                                        begin_c_loop_all (cell,cell_thread)
                                                {
                                                        C_CENTROID(xc,cell,cell_thread);
                                                        if (sqrt(pow(xc[0] -
x_drop,2.)+pow(xc[1] - y_drop,2.)) <= (diam/2.0))

                                                                C_VOF(cell,cell_thread) = 1.;
                                                        else

                                                                C_VOF(cell,cell_thread) = 0.;
                                                }
                                        end_c_loop_all (cell,cell_thread)
                                }
        }
```

```
}
/*---film phase-------------------------------------------------------------------------*/

DEFINE_INIT(init_liquid_phase_film, mixture_domain)
{
        int phase_domain_index;
        cell_t cell;

        Thread *cell_thread;
        Domain *subdomain;
        real xc[ND_ND];

        sub_domain_loop(subdomain, mixture_domain, phase_domain_index)
        {

                if (DOMAIN_ID(subdomain) == 3)

                        thread_loop_c(cell_thread,subdomain)
                                {

                                        begin_c_loop_all (cell,cell_thread)
                                                {
                                                        C_CENTROID(xc,cell,cell_thread);
                                                        if ((xc[1]) <= h_film)

                                                                C_VOF(cell,cell_thread) = 1.;
                                                        else

                                                                C_VOF(cell,cell_thread) = 0.;
                                                }
                                        end_c_loop_all (cell,cell_thread)
                                }
        }
}

/*-------air phase----------------------------------------------------------------------*/

DEFINE_INIT(init_air_phase, mixture_domain)
{
        int phase_domain_index;
        cell_t cell;

        Thread *cell_thread;
```

```
        Domain *subdomain;
        real xc[ND_ND];

        sub_domain_loop(subdomain, mixture_domain, phase_domain_index)
        {
                if (DOMAIN_ID(subdomain) == 4)
                        thread_loop_c(cell_thread,subdomain)
                                {
                                        begin_c_loop_all (cell,cell_thread)
                                        {
                                                C_CENTROID(xc,cell,cell_thread);
                                                if ((sqrt(pow(xc[0] - x_drop,2.)+pow(xc[1] -
y_drop,2.)) > (diam/2.0)) && ((xc[1]) > h_film))
                                                        C_VOF(cell,cell_thread) = 1.;
                                                else
                                                        C_VOF(cell,cell_thread) = 0.;
                                        }
                                        end_c_loop_all (cell,cell_thread)
                                }
        }
}
```

Appendix C Structure of the LMB FORTRAN Code

```
******Parameters*********************************************************

******Flags of the Nodes
Ghost=0      specifies the virtual nodes used to applay the boundary conditions
Wall=1       specifies the nodes on the walls
InletU=2     specifies the nodes in the inlet when velocity is known
OutletP=3    specifies the nodes in the outlet when pressure is known
Period=4     specifies the nodes with periodic conditions
Body=5       specifies the nodes of a immersed body
InletP=6     specifies the nodes in the inlet when pressure is known
OutletU=7    specifies the nodes in the outlet when velocity is known
Fluid=9      specifies the nodes of the fluids
Lid=10       specifies the nodes on the lid for cavity problem

******Weights used in calculation of f^eq and g^eq for each node in the lattice
W(i)

******the directions for each node in the lattice
ex(i), ey(i),ez(i)

****** the opposite node for each node
Ops(i)

******The Parameters
Xdim=81                  lattice size in x-direction expressed in lattice units
Ydim=81                  lattice size in y-direction expressed in lattice units
Zdim=21                  lattice size in z-direction expressed in lattice units
L=79.D0                  lattice length scale expressed in lattice units
MaxItr=10000             number of time steps

Uref=0.1D0               reference velocity in lattice units
Re=10                    Reynolds number
Pr=7.D0                  Prandtl number
Ra=10000                 Rayleigh number used in the free convection problems

Rho_backp=0.99D0         nondimensional density set for pressure outlet boundary
RhoInit=1.D0             initial value of flow nondimensional density
Rho_Set_inlet=1.01D0     nondimensional density in pressure inlet boundary
TUpper=0.0D0             nondimensional temperature in the upper (hot) boundary
TLower=1.0D0             nondimensional temperature in the lower (cold) boundary
TInit =1.0D0             nondimensional initial temperature in the domain
TLeft =0.0D0             nondimensional temperature in inlet boundary
TRight=1.0D0             nondimensional temperature in outlet boundary
dT=1.0D0                 nondimensional temperature difference between hot and
                         cold sides

Tfreez=-0.7D0            nondimensional temperature of the freezing point
EpsT=0.05D0*(dT)         temperature difference used in modelling the ice
                         porosity
InitZeroVel=.True.       if TRUE initiates the zero velocity, otherwise initiates
                         by Uref
```

```
******Main Program*****************************************************************
Program TLBM
Call Lattice                    generates the lattice for the computations
Call Initiate                   initiates the variables for flow simulation
Call Initiate_T                 initiates the variables for thermal simulation
Call CalFeq                     initiates f with f^eq
Call CalGeq_T                   initiates g with g^eq
Do Itr=1,MaxItr                 the main loop of the simulations performed for
                                each time step
      Call BC                   apply the boundary conditions for flow simulation
      Call CalMacroVar          calculates the macro variables from f
      Call CalFeq               calculates f^eq based on calculated macro variables
      Call Collision            calculates the collision term
      Call PorosityForce        modify f to consider the porosity during the
                                solidification process
      Call Streaming            shifts f to model the convection
      Call BuoyancyForce        calculates the free convection terms
      Call BC_T                 apply the boundary conditions for thermal
                                simulation
      Call CalMacroVar_T        recovers the temperature from g
      Call CalGeq_T             calculates g^eq based on calculated macro variables
      Call Collision_T          calculates the collision term of energy equation
      Call Streaming_T          shifts g to model the convection in the energy
                                equation
      Call Solidification       determines the phase changes between liquid water
                                and ice
End Do
Call Output                     makes the output files and data for post-
                                processing
End Program TLBM
```